# Previously undetected disturbances are the dominant driver of carbon loss in protected Amazonian forests

Liang Wan[1,*], Philippe Ciais[1], Aurélien de Truchis[2], Ewan Sean[2], Fabian Jörg Fischer[3], Ricardo Dalagnol[4], Clément Bourgoin[5], Yidi Xu[1], Nan Meng[1], Xiaojun Li[6], Arthur Fendrich[5], Clément Albergel[7], Youngryel Ryu[8], Stephen Sitch[9], Thais Michele Rosan[9], Jean-Pierre Wigneron[10], Fabien H. Wagner[4], Shidong Liu[11], Lei Zhu[1], Agnès Pellissier-Tanon[1], Ibrahim Fayad[1,2], Gabriel Belouze[1], Clement J. F. Delcourt[1], Sassan Saatchi[4,12], Luiz E. O. C. Aragão[13,9], Jean P. Ometto[13]

1. Laboratoire des Sciences du Climat et de l'Environnement, LSCE/IPSL, CEA-CNRS-UVSQ, Université Paris Saclay, 91191 Gif-sur-Yvette, France
2. Kayrros SAS, Paris 75009, France
3. TUM School of Life Sciences, Ecosystem Dynamics and Forest Management, Technical University of Munich, Hans-Carl-von-Carlowitz-Platz 2, 85354 Freising, Germany
4. CTREES, Pasadena, 91105 California, USA
5. European Commission, Joint Research Centre (JRC), Ispra, 21027, Italy
6. Faculty of Geosciences and Engineering, Southwest Jiaotong University, Chengdu, 611756, China
7. European Space Agency Climate Office, ECSAT, Didcot, UK
8. Department of Landscape Architecture and Rural Systems Engineering, Seoul National University, Republic of Korea
9. Faculty of Environment, Science and Economy, University of Exeter, Exeter, EX4 4QF, UK
10. ISPA, UMR 1391 INRAE/Bordeaux Science Agro, 33140 Villenave d'Ornon, France
11. State Key Laboratory of Remote Sensing and Digital Earth, Aerospace Information Research Institute, Chinese Academy of Sciences, Beijing 100094, China
12. Jet Propulsion Laboratory, California Institute of Technology, Pasadena, 91109 CA, USA
13. Earth Observation and Geoinformatics Division, National Institute for Space Research (INPE), São José dos Campos, Brazil

* Corresponding authors (liangwanzju@gmail.com; liang.wan@lsce.ipsl.fr)

**Preprint status.**

This manuscript is an EarthArxiv preprint and has been submitted to a journal for peer review and possible publication. Subsequent versions of this manuscript may differ from the present version.

**Supplementary information:**

**Supplementary Text 1– Text 13**

**Supplementary Fig. 1– Fig. 45**

**Supplementary Table 1– Table 14**


## Abstract

Amazonian forests face increasing pressures from human-induced deforestation and degradation, compounded by natural disturbances such as droughts and windthrow events. In response, forest protection policies strengthened and formalised large protected areas and Indigenous lands[1,2], now covering 43% of the region. However, clearings and degradation in these protected areas are complex and hard to detect with current medium-resolution satellite observations. Here we mapped canopy height (10 m) and aboveground biomass carbon (30 m) changes from 2019 to 2022 by combining ~727,000 spaceborne LiDAR measurements with Sentinel-1/2 imagery using a deep learning framework. We estimate a net aboveground carbon loss of −257 ± 47 Tg C $yr^{-1}$ across the entire Amazon forest, with changes in carbon density aligning with field inventory data. Gross losses from agricultural expansion, logging, fire, road construction, and drought (−437 ± 42 Tg C $yr^{-1}$) exceed gross gains of 180 ± 20 Tg C $yr^{-1}$, with secondary-forest regrowth contributing 38 ± 7 Tg C $yr^{-1}$. Approximately 28% of net carbon loss occurred within protected areas, including 6% in Indigenous lands. We found that 80% of total carbon losses were associated with small disturbance patches and low height losses, which remain largely undetected by Landsat-based disturbance products yet supported by independent airborne LiDAR and PlanetScope imagery. As a result, carbon losses exceeded Landsat-based estimates by 84% in non-protected areas and 166% in protected areas, and were 36–55% higher than passive-microwave-based estimates[3,4] and consistently greater than those from dynamic vegetation models. These findings highlight the critical role of high-resolution monitoring in uncovering hidden carbon losses and underscore the need for improved conservation strategies, even within formally protected Amazonian forests.


## Main

Achieving the climate targets of the Paris Agreement requires stopping carbon emissions from deforestation and forest degradation, while preserving intact tropical forests and restoring degraded ones [5-7]. The Amazon forest is critical in this context as it holds one-third of tropical forests biomass[8,9] and exerts a strong influence on regional [10] and global climate. In the 2000s, more than

half of the Amazon forest was under formal protection through designated protected areas, an essential measure to limit deforestation and preserve carbon stocks and biodiversity[1,2]. However, those protected areas are not immune to drought and increasingly exposed to external pressures such as fires, illegal logging and mining activities, and spillover from surrounding land use change[11-13]. Since 1990, the Amazon countries have lost nearly 18% of their undisturbed tropical moist forests[13], and the remaining areas are increasingly affected by climate extremes (more frequent and severe droughts, high temperatures and storms) and forest degradation through direct human pressure caused by forest fragmentation (e.g. the edge-effect), logging, and fires [14]. Compounded human and climate disturbances accelerate carbon losses[15,16] and undermine the integrity of protected areas and challenge their enforcement [17], especially in the Amazon, which experiences frequent small disturbances[18,19].

Current approaches have limitations to capture where and why aboveground biomass carbon (AGC) is changing over the Amazon forest[1,3,11,20]. Previous research either mapped and classified disturbance events from satellite imagery without quantifying associated carbon losses[13,21-24], or estimated carbon change at coarse resolution (100 m to 25 km) from optical and passive microwave sensors[25-27] (**Supplementary Table 1**). Coarse resolution maps miss small scale but pervasive processes such as selective logging, edge degradation, and early regrowth[28,29], as well as the dynamics of small forest fragments in complex landscapes [30,31]. This is particularly problematic in protected areas where the low density of population and roads makes disturbances more scattered, irregular and hard to detect[32]. Recent efforts to map tree height provide a promising basis for high-resolution biomass estimation[33], but currently remain limited to a single epoch. This highlights the need for high-spatial-resolution height and biomass change products (≤30 m) to detect disturbance processes that are often overlooked in existing forest disturbance datasets, particularly disturbances associated with small patch sizes (<2 ha) [19] or low canopy height loss (<5 m) [34]. These include minor deforestation clearings, forest degradation, and gains from secondary forest regrowth or gap recovery in old-growth forests[12,13,35].

Millions of height and vertical structure measurements on meter-scale, discrete footprints from the Global Ecosystem Dynamics Investigation (GEDI) spaceborne LiDAR have greatly advanced our capabilities for monitoring changes of trees' dominant height and AGC [36-38]. However, the sparse spatial sampling, the lack of revisits of individual footprints and their geolocation errors prevent a complete systematic mapping of disturbances using GEDI data alone. To overcome these

limitations, we transformed discrete arrays of GEDI footprints into continuous yearly maps of height at 10 m resolution by using a deep learning model leveraging Sentinel radar and optical imagery images [39]. This allowed us to generate maps of height change at 10 m and 30 m resolutions from 2019 to 2022, and derive AGC changes at 30 m resolution across the Amazon forest, defined as pixels with forest height ≥ 5 m [40,41], using allometric relationships trained on 434 forest inventory plot measurements[42-45] (**Methods**, **Supplementary Fig. 1–12**). The maps of height were evaluated against ~1,400 reference airborne LiDAR (ALS) campaigns[46-48] covering the Brazilian Amazon ($R^2$ = 0.56, MAE = 4.37 m) (**Supplementary Fig. 14**). Biomass was evaluated against 109 independent forest inventory plots that were not part of the training data ($R^2$ = 0.56, MAE = 30.22 Mg C $ha^{-1}$). The performance of the canopy height and biomass maps across different forest types is presented in **Supplementary Text 7**.

We validated height change using two recently available repeat ALS acquisitions collected in the Caxiuanã[49,50] and Jamari[51,52] National Forest, which showed acceptable agreement at 30 m ($R^2$ = 0.32, MAE = 3.17 m) (**Supplementary Fig. 17**). As the ALS data mostly cover intact forests with relatively stable structure, our satellite-derived height changes were small (<5 m), and fine-scale gaps and rapid regrowth observed in ALS may remain difficult to capture at 10–30 m resolution. Further, we compared height loss detections in Mato Grosso against a reference map of tree cover loss from 5-meter resolution PlanetScope optical images (**Supplementary Fig. 18**) [53,54]. Our mapping detects 43%–86% of all tree cover loss events at varying scales, missing only the very smallest features that fall below the 10-m spatial resolution of the Sentinel satellites (**Supplementary Text 8, Supplementary Fig. 20**). By contrast, the Landsat-based Tropical Moist Forests (TMF) [13], Global Forest Change (GFC) [22], and radar-based RAdar for Detecting Deforestation (RADD) [23] disturbance datasets captured less than 20% of the Planet-derived tree cover loss at fine spatial scales. In addition, at a broader kilometer-scale, height changes given by year-on-year differences of our maps were found to match the statistical estimations of change derived from clusters of sparse GEDI footprints (**Supplementary Fig. 17**, **22–24**).

We further conducted a systematic validation of CH loss and gain patches using an independent set of high-resolution (5 m) PlanetScope imagery (**Methods**). Samples were stratified by patch-size class (0–2, 2–10, and 10–100 ha) and change types (**Supplementary Fig. 25**), and randomly selected 581 loss patches and 522 gain patches were visually interpreted by comparing PlanetScope imagery acquired between 2019 and 2022. The area-weighted user's accuracies reached 75.5% for

581 CH loss patches and 72.5% for 522 CH gain patches (**Supplementary Table 3**). Validation accuracy generally increased with patch size, whereas the low accuracies were observed for small patches (<2 ha). This likely reflects both residual noise in the mapped products and the intrinsic difficulty of visually identifying subtle CH changes from optical imagery, particularly for very small patches with mean CH changes close to zero. Image-chip validation further showed that the reliability of CH-loss detections increased with increasing CH-loss magnitude (62%–87%) (**Supplementary Fig. 25, Fig. 26**), whereas the lowest detection reliability occurred for the smallest-magnitude class ($-2 \leq \Delta CH < 0$ m) (**Supplementary Table 4**). Because subtle CH losses often produce only weak visual signatures in optical imagery, these estimates are likely conservative for both small patches and low-magnitude CH losses. Consistent with this interpretation, independent repeat ALS measurements confirmed numerous low-magnitude CH-loss events that were not detected by conventional forest disturbance products, including TMF, GFC and RADD (**Supplementary Fig. 17**, **Supplementary Table 5**).

The height change patterns shown in **Fig. 1** align well at first glance with Landsat-based TMF disturbance data [13] across the Amazon (**Supplementary Fig. 17**). This visual agreement is evident when zooming into smaller regions (**Fig. 1c–e**) where predicted height losses coincide with deforestation (permanent forest removal) and degradation (short-period disturbance), and height gains with forest regrowth events following deforestation in TMF, particularly in regions with large height changes (**Supplementary Fig. 21**). Compared to TMF disturbances, GFC tree cover loss[22], and RADD [23], our data displayed more small height loss events.

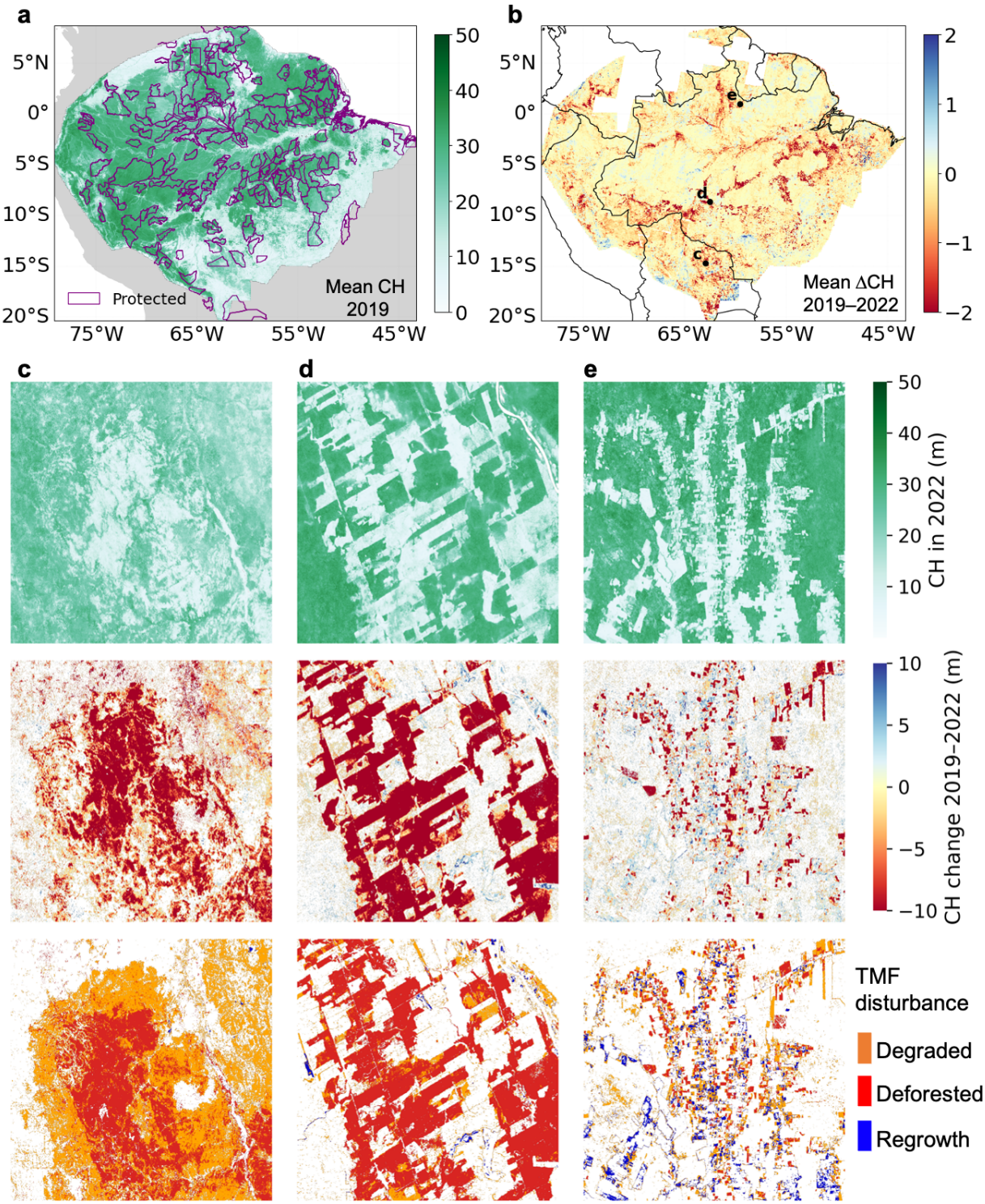



**Fig. 1: Mapping canopy height (CH) change in the Amazon. a, b,** Spatial distribution of CH in 2019 and CH change (ΔCH) from 2019 to 2022, aggregated to 5-km grid cells for visualization. The height change was averaged from the change and non-change pixels within each 5-km grid cell. The blank area in the upper part of the ΔCH map (**b**) corresponds to missing Sentinel-1 observations in 2022. The locations of three representative regions, indicated by black points, highlight distinct patterns in disturbance type distributions. To improve visual clarity, only the boundaries of large

protected areas (area > 0.5 Mha) are highlighted in purple. **c, d, e,** Maps of CH in 2022 (top row), ΔCH from 2019 to 2022 (middle row), and Tropical Moist Forest (TMF) disturbance types (bottom row) at 30 m resolution for three 30 km × 30 km regions. To emphasize CH gains, ΔCH was visualized within a range of –10 m (≤ –10 m) to +10 m (≥ 10 m). Forest degradation (orange), deforestation (red), and regrowth (blue) derived from the TMF data are shown in the bottom row.

**Aboveground carbon changes by disturbance type and protection status**

Firstly, we look at large-scale carbon changes. To do so, we classified 30-m AGC changes (2019–2022) into deforestation, degradation, regrowth, and other types by combining our height change maps with TMF disturbances types[13] (**Methods, Supplementary Text 9)**. Over the whole Amazon, we found a net AGC loss of −257 ± 47 Tg C $yr^{-1}$ across a disturbed area of 116 ± 9 Mha. This net loss resulted from gross losses of −437 ± 42 Tg C $yr^{-1}$ exceeding gross gains of 180 ± 20 Tg C $yr^{-1}$ (**Supplementary Table 6)**. On average 43% of the gross losses was attributed to degradation (−190 ± 31 Tg C $yr^{-1}$), against 21% to deforestation (−93 ± 15 Tg C $yr^{-1}$) and the remaining 36% to 'losses in other forests' which means disturbances that were undetected by TMF, and are systematically associated with minor height changes (≤ 5 m) in our dataset, potentially reflecting understory disturbance and very small-scale logging activities [55,56].

The largest AGC losses are concentrated in the southern and eastern Amazon basin (**Fig. 2a**), particularly within the arc of deforestation spanning Pará, Mato Grosso and Rondônia in Brazil, where extensive deforestation and degradation occurs[57] and most of the TMF disturbances are found (**Supplementary Fig. 17e)**. The 'losses in other forests' not included by TMF are mainly in central Amazonia near major rivers and road corridors (**see loss driver analysis below**) [58], with additional hotspots in the Andean foothills of Peru and Bolivia, often linked to mining and agricultural expansion [59]. Some of these losses may reflect natural processes, such as river dynamics[60] or disturbance events within bamboo-dominated forest[61]. The AGC gains are more diffuse than the losses, reflecting secondary forest regrowth[35] along the deforestation frontiers at the edges of the Amazon and undisturbed forest growth in central Amazonia (**Fig. 2a**). Secondary forest regrowth as identified by TMF[13] and our height gains, accounted for 21% of the gross AGC gain (38 ± 5 Tg C $yr^{-1}$).

The key result is that in the protected areas, which cover 43% of the study area[62], the net AGC carbon losses amounted to −72 ± 18 Tg C $yr^{-1}$ (**Fig. 2b, c**), that is 28% of the total net loss. The

spatial distribution of AGC changes (**Supplementary Fig. 28a, b)** provides detailed information on the effectiveness of each protected region. We found that 69% of the protected areas (n = 1248) experienced AGC losses during the study period (**Fig. 2d**), with Indigenous Areas (−15.6 Tg C $yr^{-1}$), Environmental Protection Areas (−8.7 Tg C $yr^{-1}$), and National Parks (−7.1 Tg C $yr^{-1}$) experiencing the largest losses. When normalized by area, however, Indigenous Areas exhibited the lowest average carbon density loss (−0.15 Mg C $ha^{-1}$ $yr^{-1}$), compared to Environmental Protection Areas (−0.62) and National Parks (−0.25) (**Supplementary Table 7**). The larger total carbon loss in Indigenous land is primarily driven by partial canopy removal rather than complete forest conversion, and likely reflects selective logging, small-scale agriculture, and controlled fire use [1,63].

Further analysis revealed that protected areas that were designated 12–16 years before 2019 experienced larger net carbon losses (−15.1 Tg C $yr^{-1}$) compared to those established in earlier years (−13.2 Tg C $yr^{-1}$) while the recent conservation areas designated 4–8 years before 2019 exhibited smaller changes (**Supplementary Fig. 28d**). Even the strictest protection level labelled as Ia and II according to the International Union for Conservation of Nature (IUCN) [62] showed large net AGC losses. The category Ia also shows a high AGC loss density, just below category V (protected landscapes) and areas with no IUCN categories (**Supplementary Table 8**). While some of the AGC loss in protected areas may result from natural disturbances, the data shown in **Fig 2d** suggests that a stricter official protection level does not necessarily associate with less degradation [64]. Furthermore, we found substantial differences in biomass carbon dynamics among forest types across the Amazon. Most carbon losses occurred in forest formations (−187.4 Tg C $yr^{-1}$) followed by flooded forests (−71.1 Tg C $yr^{-1}$), whereas mangroves and savanna formations showed comparatively smaller carbon changes (**Supplementary Table 9**), highlighting strong contrasts in disturbance and recovery dynamics among Amazonian ecosystems. The large carbon losses in flooded forests likely reflect their high exposure to hydrological extremes and increasing human activities along major river corridors[65,66].

Our AGC loss estimates are on average higher than those reported in previous studies, but remain within their uncertainty ranges, likely due to differences in models, spatial resolution, and temporal coverage. In comparison with our net loss (2019–2022) of −257 ± 47 Tg C $yr^{-1}$, Fawcett et al. [4] using multiple satellite datasets assessed a loss of −189 ± 59 Tg C $yr^{-1}$ and Fendrich et al. using downscaled L-band vegetation optical depth measurements gave a loss of −166 Tg C $yr^{-1}$ [3] during

2012–2019 (**Supplementary Table 10**). Similar patterns were also observed in protected areas, where we detected more carbon losses from degradation (−48 ± 6 Tg C $yr^{-1}$) and deforestation (−16 ± 2 Tg C $yr^{-1}$) than the average long-term losses reported by Fendrich et al.[3] (−8 to −17 and −5 to −7 Tg C $yr^{-1}$, respectively), although protected areas consistently showed a lower mean carbon loss rate per unit of forest area than non-protected areas in both approaches (**Supplementary Table 8**).

Our estimates differ from top-down atmospheric inversion models, bottom-up flux estimates, and hybrid approaches because they represent different carbon pools and processes (see **Supplementary Text 10** for detailed comparisons). By resolving small-scale degradation, afforestation, plantations and post-disturbance regrowth, our approach provides a complementary, spatially explicit perspective on the Amazon carbon balance.

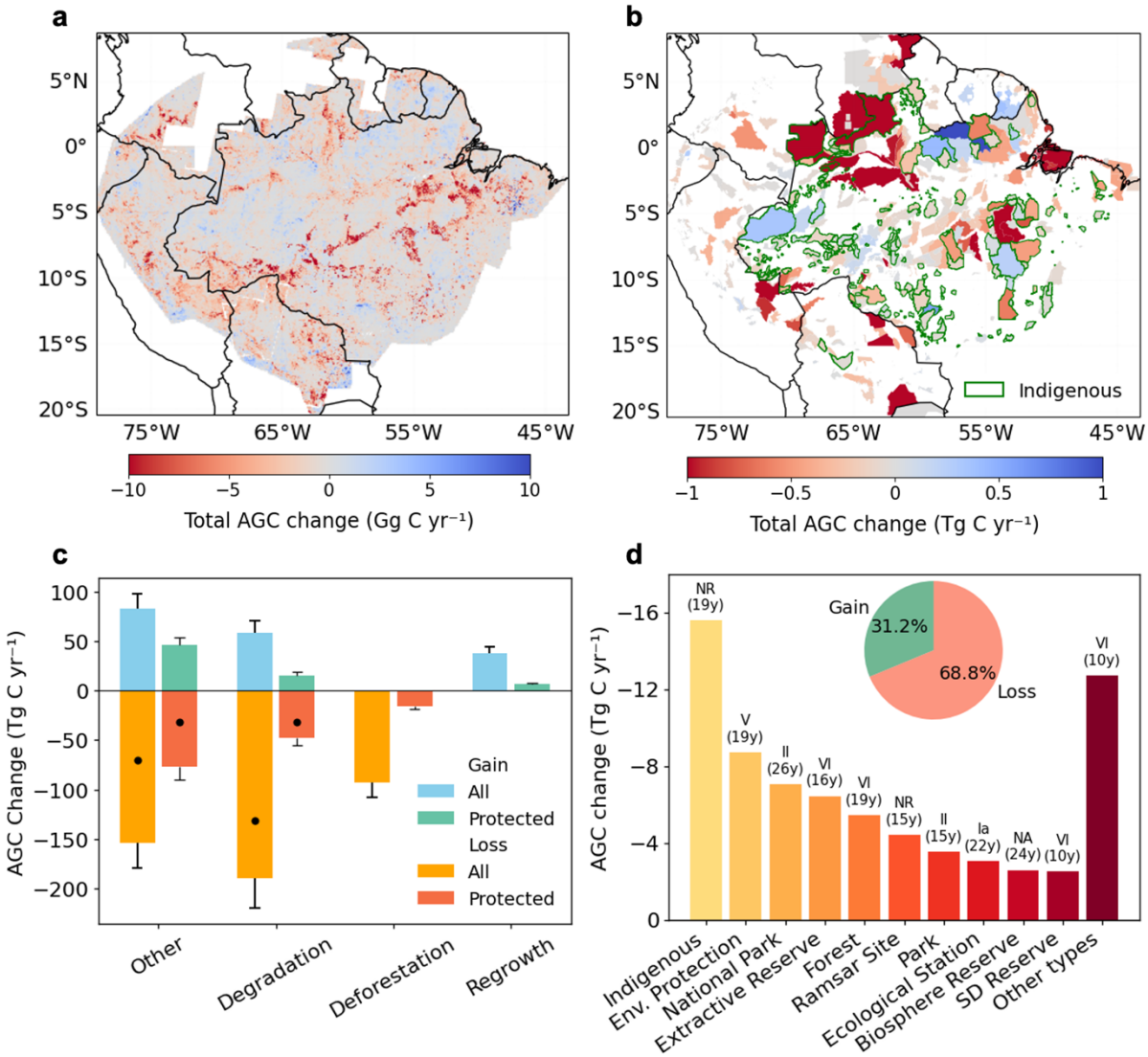


**Fig. 2: Aboveground biomass carbon (AGC) budget across the Amazon and protected area.** **a, b,** Spatial patterns of mean annual AGC change from 2019 to 2022, displayed for: all 5-km grid cells (Gg C $yr^{-1}$) (**a**) and officially designated protected areas (Tg C $yr^{-1}$) (**b**). The boundaries of Indigenous areas within all protected areas were highlighted in green. **c**, Mean annual AGC gains and losses (Tg C $yr^{-1}$) by forest disturbance class, shown for the entire study area and protected areas. Disturbance classes include secondary, degraded, and deforested forests, derived from canopy height (CH) change and TMF disturbance data, and other forests are areas not classified as disturbed by TMF but showing CH changes. Bars represent AGC gains and losses with estimated uncertainty, and black dots denote the net carbon change for the corresponding category. **d,** Mean annual AGC change (Tg C $yr^{-1}$) from 2019 to 2022 for different protected area types[62]. The top 10 categories with the greatest AGC loss are shown; remaining types are grouped as "other types". Pie charts show the proportion of protected regions experiencing net AGC gain or loss. The primary IUCN management categories (Ia, Ib, II, III, IV, V, and VI), along with the mean year (such as 19y) of designation (as of 2019), are shown above each bar for each protected area type. "NR" and "NA" indicate cases where IUCN categories were not reported or not applicable, respectively.

## Previously overlooked small forest disturbances and implications for carbon change

Then, in a second step, we tried to understand how the carbon loss presented above relates to the structure of forest disturbances. The main finding is that a large number of forest disturbances in our dataset were not detected by previously used Landsat satellite-based products such as the Tropical Moist Forest (TMF). Out of 70 million hectares with small height losses (<5 m) distributed across 40 million disturbance events in our dataset, ~80% were not identified as disturbances by the TMF dataset at 30 m resolution (**Fig. 3a**). Similarly, the proportion of small disturbance patches (<2 ha) associated with height loss was relatively higher in our dataset than in the TMF disturbance maps (**Fig. 3b**). We also detected much more disturbance than reported in the widely used Landsat-derived Global Forest Change (GFC) tree cover loss dataset [22], and the Sentinel-1 radar-based RAdar for Detecting Deforestation (RADD) product[23]. This highlights a substantially greater sensitivity of our datasets to small disturbance patches and height losses, including those associated with logging, road construction, fragmentation, and natural processes (**Supplementary Fig. 29**), often missed by conventional disturbance products. Independent visual validation confirmed that the majority of mapped small disturbance patches and low-magnitude CH-loss events corresponded to real canopy disturbances observed in PlanetScope imagery (**Supplementary Table 3**, **Table 4**). Although uncertainties remain, particularly for the smallest patches (< 2 ha) and lowest-magnitude

CH losses (< −5 m), these arise from a combination of residual uncertainty in the mapped CH products and the intrinsic limitations of visual interpretation using optical imagery, where subtle structural changes occupying only a few pixels may not produce sufficiently distinct visual signatures for reliable identification. Consequently, the reported validation accuracies for these categories are likely conservative. Further analyses restricted to visually confirmed CH-loss patches and image chips yielded consistent results, showing that TMF, GFC and RADD still omitted a substantial proportion of confirmed small disturbance patches and low-magnitude CH-loss events (**Supplementary Table 5**).

In contrast to our estimate of a net AGC loss of −257 Tg C $yr^{-1}$ across all height loss events, keeping only the patches detected by TMF, GFC[22], RADD[23] would give much lower losses of −127, −125, and −79 Tg C $yr^{-1}$, respectively (**Supplementary Fig. 30**). So, the main reason why we found greater AGC losses than previous studies is that we detected more tree height loss events. Small height loss events (<5 m) contribute the most to gross AGC loss, yet ~80% of these events were not captured by TMF. Small height losses (<5 m) contributed ~54% of gross AGC loss, yet ~80% of these events were not captured by TMF. Although the lowest CH-loss magnitude class ($-5 \leq \Delta CH < -2$) showed lower validation accuracy (62–68%; **Supplementary Table 4**), reflecting both residual uncertainty in the mapped CH estimates and the intrinsic limitations of visually identifying subtle disturbances from optical imagery, most of the associated AGC loss occurred within disturbance patches larger than 10 ha. These larger patches accounted for 69% of the gross AGC loss associated with CH loss (**Supplementary Table 11**) and exhibited high validation accuracy (~84%; **Supplementary Table 3**). Therefore, uncertainty associated with low-magnitude CH-loss detections does not substantially alter our overall estimates of carbon loss.

For deforestation, we found that clearings of moderate size (2–100 ha) account for 54% of the total deforestation-driven loss of biomass (−50 Tg C $yr^{-1}$) whereas large clearings >1000 ha contributed only 8% (**Supplementary Fig. 31**). The very small deforestation patches (<2 ha) contributed a small fraction of the net carbon loss, likely because many of those small clearings happen in younger low biomass secondary forests [67]. For degradation, patches of up to 100 ha in size dominate the loss of biomass (58%) while small degradation patches showed insignificant changes, possibly because they coincide with tree regrowth [13,35]. For patches of forest regrowth as identified by TMF, the small ones (<2 ha) contributed 39% of the total biomass regrowth gain at basin scale while the patches larger than 100 ha, typically planned afforestation projects, contributed 13%. Within

protected areas, small regrowth patches contributed 47% of regrowth gain. The biomass gains observed in small regrowth patches typically reflect regeneration after fire and logging (**Supplementary Fig. 32**).

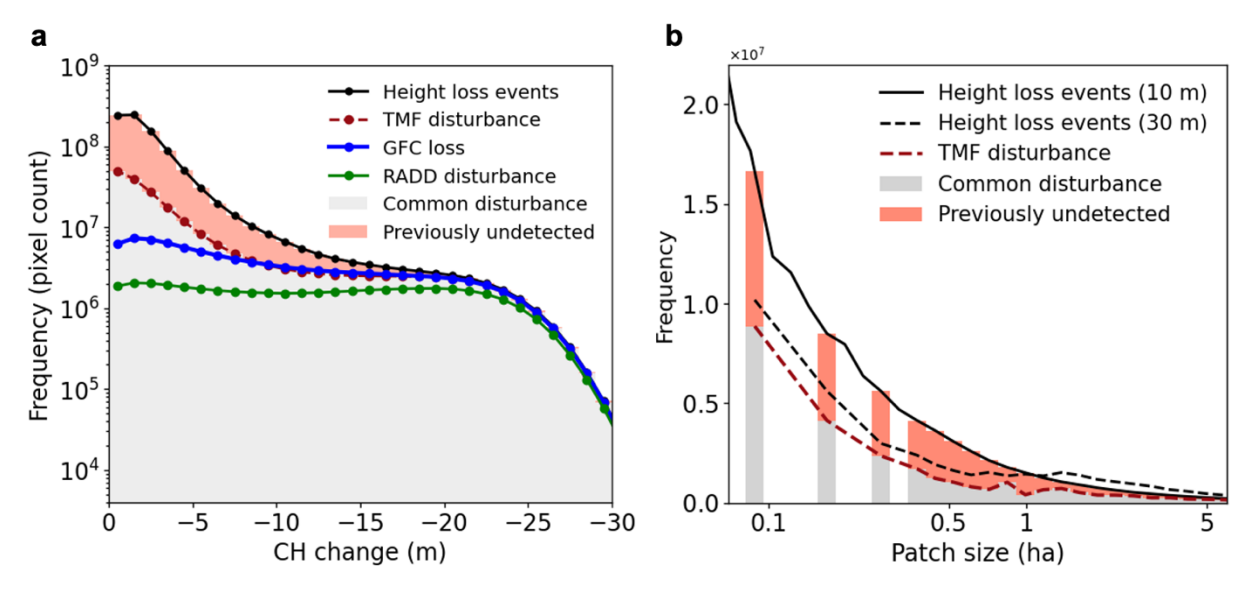



**Fig. 3: Comparison of detected canopy height loss with reference disturbance datasets**. **a,** Frequency distribution of CH loss (ΔCH < 0) between 2019 and 2022 across 1-m ΔCH bins, compared with corresponding disturbance pixels from the the Tropical Moist Forest (TMF), Global Forest Change (GFC), and radar-based RAdar for Detecting Deforestation (RADD) datasets. TMF disturbances include both degradation and deforestation pixels. Disturbance pixels from these datasets were overlaid with the CH change map to estimate the proportion of height loss detected, as they do not explicitly provide canopy height change information. Common disturbance indicates pixels detected by existing disturbance datasets (TMF, GFC or RADD), whereas previously undetected events represent additional canopy height loss not captured by these products. **b,** Comparison of frequency distributions between TMF disturbances and CH loss across varying patch sizes. Patch size was grouped into 51 logarithmically spaced bins ranging from 0.01 to 100,000 ha. Only the 0–10 ha range is shown due to the concentration of differences in smaller patches. A logarithmic scale was applied to better visualize variation that would be obscured on a linear scale.

In the third step of this analysis, we examined how disturbance type and patch size jointly influence biomass carbon density dynamics, complementing the total carbon changes described above. Both deforestation and degradation caused substantial declines in AGC density (**Supplementary Fig. 33**). The temporal trajectories of AGC density following degradation and regrowth varied with

patch size. Overall, the AGC density changes per unit disturbed area estimated in this study are consistent with previous findings[37,57,68] (**Supplementary Table 12**), despite differences in spatial coverage, sampling density and methodology. We also discussed the relationship between disturbance density and changes in AGC density (see details in **Supplementary Text 11**).

## Natural and anthropogenic drivers of biomass carbon loss

The final part of the analysis is about drivers of carbon losses. To address this question, we generated a comprehensive 1-km resolution map of the drivers of biomass loss by integrating an existing map of forest loss drivers[69] with a 30-m Landsat-based burned area map [70], a new 5-m road map detected from Planet data [71], and additional inputs from previously developed Amazon degradation driver maps (0.09–0.5°)[14] (**Methods**). This detailed multiple drivers allows us to better separate natural and anthropogenic drivers of AGC dynamics at 1-km resolution in Amazonian forests. In short, we found that most of the recent carbon losses were dominated by agricultural expansion, followed by logging and fire disturbance (**Fig. 4a**), consistent with refs [14,57]. But we identified road presence as a significant factor associated with AGC losses (**Supplementary Fig. 40**). In details, permanent agriculture contributed most to AGC decline (−149 ± 32 Tg C $yr^{-1}$, 58% of the net loss), followed by logging (−22 ± 8 Tg C $yr^{-1}$, 8.6%), fires (−19 ± 5 Tg C $yr^{-1}$, 7.3%), and settlements and infrastructure including road expansion (−13 ± 4 Tg C $yr^{-1}$, 5.2%), while drought, shifting cultivation, and mining expansion each accounted for smaller fractions (< 5%) (**Fig. 4b**).

Forest degradation in the Amazon results from multiple interacting disturbance pathways, including burned-area fraction, logging area, edge area, distance to roads, forest age, land-use transition type, and disturbance density (see **Supplementary Text 12**). The proximity of roads is generally associated with higher AGC losses from degradation (**Fig. 4c**). Both total AGC and mean AGC density changes declined steeply away from the nearest road, with an edge effect extending ~2.5 to 3.5 km away from the nearest road, slightly larger than the ~2 km effect reported using GEDI biomass data[12]. Sensitivity tests confirmed that edge distances shorten at lower road fraction (percentage of road pixels) thresholds and lengthen at higher ones (**Supplementary Fig. 41**), reflecting differences between fragmented margins and major road corridors. Despite our AGC losses being concentrated in areas with low burn fractions, small edge areas, and logging, the mean AGC density loss consistently increased with disturbance intensity, particularly under extensive edge influence and large-scale logging (**Supplementary Fig. 42**). Forest age further modulated

vulnerability to AGC decline (**Fig. 4d**): losses were dominated by old-growth forests (>200 years), with additional contributions from young stands (0–20 years) and forests of uncertain age.

An important question is whether protected areas exhibit a distinct attribution profile than non-protected forests. The answer is that in protected areas, AGC losses were caused mainly by agricultural expansion (29.7%), logging (12.4%), settlements and infrastructure (9.7%), fires (9.6%) and drought (9.4%) (**Supplementary Fig. 43**). Here, agriculture is called 'permanent' as it indicates a long-term land-use conversion (i.e., deforestation). These losses in protected areas are closely associated with mixed natural and human disturbances. In contrast, AGC losses in non-protected areas were dominated by permanent agricultural expansion (69.4%) and logging (7.2%) with more carbon loss from degradation than from deforestation (**Supplementary Fig. 43**).

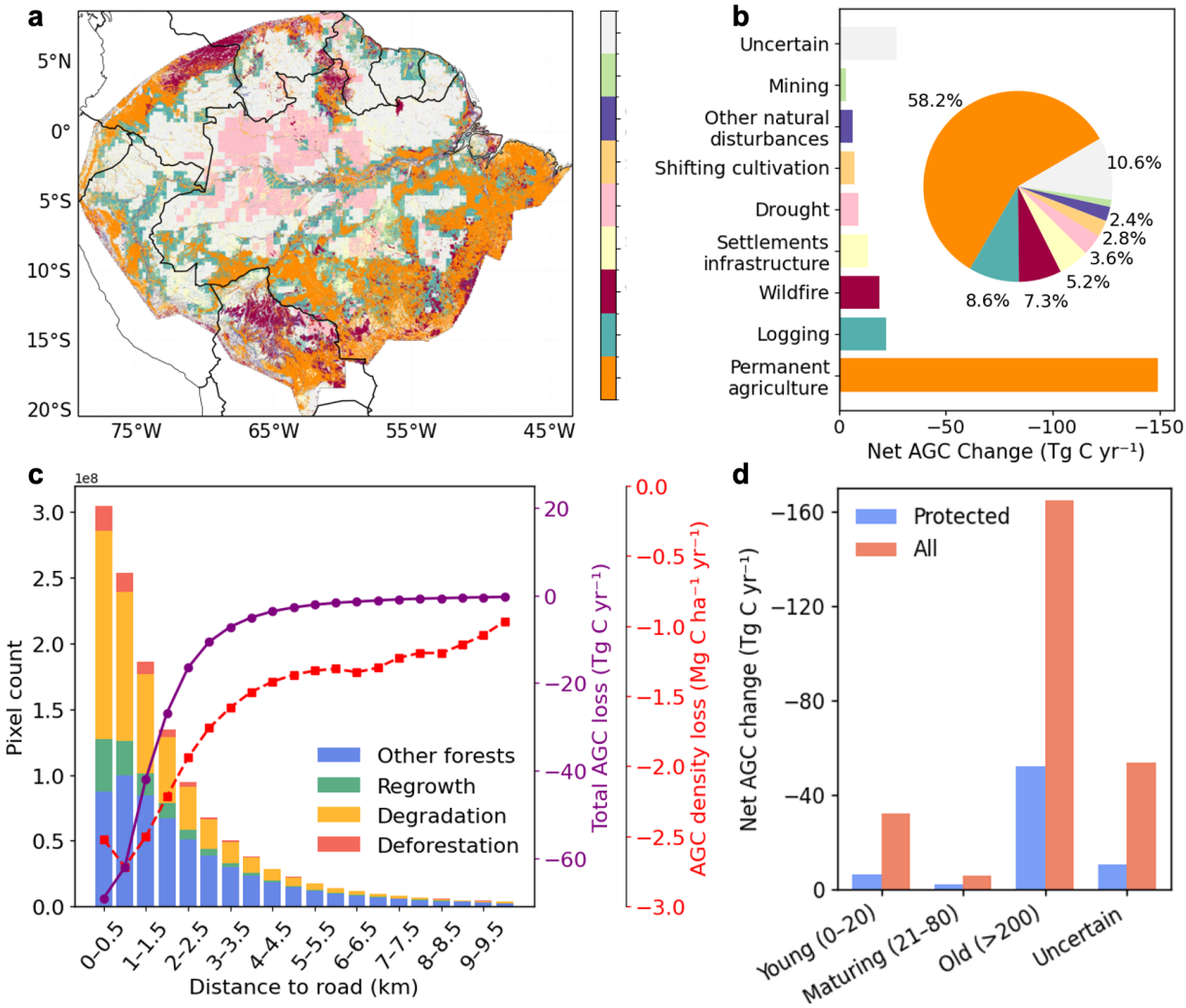



**Fig. 4: Drivers and spatial patterns of aboveground carbon change (AGC) in Amazonian forests. a,** Spatial distribution of forest loss drivers at 1-km resolution across the Amazon basin.

The loss driver was derived from an updated dataset integrating 1-km forest loss drivers, 30-m Landsat-based burned area data, 5-m road data, and an Amazon forest degradation driver map. **b,** Contribution of different drivers to net AGC change from 2019 to 2022, with corresponding percentages. Only contributions (percentage) above 2% are shown. **c,** Relationship between distance to roads and AGC change for other forests, regrowth, degraded, and deforested areas. We calculated the distance of each pixel with valid AGC change values to the nearest road pixel with a road fraction above 0.2 at 30-m resolution, and further examined the effects of different road fractions at this scale (**Supplementary Fig. 41**). **d,** Net AGC change across forest age classes (young, maturing, mature, and old) within all Amazon and protected areas.

## Towards high-resolution tropical carbon monitoring

While our approach enables high-resolution, spatially continuous assessments of Amazonian carbon change, several methodological limitations remain. Although multiple spatial and temporal consistency constraints were applied to reduce isolated noise and unstable retrievals, uncertainties associated with field plot geolocation, input datasets, and model assumptions cannot be fully eliminated, especially in structurally heterogeneous tropical forests. Furthermore, forest extent was defined structurally using a canopy height threshold of ≥5 m[40], primarily at 30 m resolution. Within this domain, the height change data remains sensitive to small structural variations (≤5 m), consistent with independent disturbance and height-change datasets (**Supplementary Fig. 17, Fig. 18**), despite filtering some minor fluctuations during preprocessing. This structural definition does not explicitly distinguish anthropogenic disturbance from natural canopy dynamics. Nevertheless, the strong spatial clustering of large losses near agriculture, mining areas, and land-use transitions suggests that the dominant carbon-loss signal reflects human-driven disturbance (**Fig. 4**). Because driver attribution relies on a 1 km loss-driver dataset, part of the apparent spatial coherence may reflect the resolution of the attribution product. Although our height and AGC change estimates provide finer spatial detail than previous products, direct comparisons are limited by differences in resolution, temporal coverage, and biomass model assumptions. Independent evaluations suggest that our carbon-loss estimates are likely conservative (See the discussion of the limitations in **Supplementary Text 13**).

Even under conservative assumptions, our analysis indicates that small disturbances patches and low height losses constitute the dominant source of carbon loss across Amazonian forests, including within protected areas, where carbon losses arise from a combination of natural disturbances and

human activities. These disturbances, often below the detection thresholds of conventional satellite products, collectively produce substantial biomass losses despite their limited spatial extent[72]. This finding aligns with emerging evidence that persistent small clearings can drive long-term biomass decline in tropical forests[19], even where large-scale deforestation is constrained. By capturing fine-scale canopy height changes, our approach highlights a pervasive but largely overlooked pathway of carbon loss that may not be adequately addressed by conservation policies focused primarily on large disturbance events.

Our findings carry direct policy relevance. By leveraging spatially continuous biomass estimates with wall-to-wall coverage, this study provides finer spatial insights into carbon loss patterns than coarse-resolution satellite products and complements localized airborne lidar campaigns. Alarming declines in protected areas highlight the limitations of current safeguards in fully preventing carbon loss[17,73], although some losses may also result from natural disturbances such as droughts. Notably, although protected areas exhibit lower average carbon losses than unprotected lands, their vast spatial extent means that even relatively small per-area declines translate into substantial total carbon loss, underscoring their critical importance for regional carbon balance. At the same time, agricultural frontier expansion, partly driven by economic necessity, is proceeding at unsustainable rates[74]. Moreover, the lack of rigorous legal frameworks for monitoring protected land and the increasing vulnerability of Indigenous lands highlight urgent governance gaps[75]. Effective climate and conservation policy should move beyond nominal protection and focus on practical, place-based actions that safeguard both ecosystem integrity and the rights of local communities.

## Methods

### Mapping canopy height and aboveground biomass

We employed multi-source remote sensing data to map 10 m canopy height (CH) across the Amazon forest (*Amazonia sensu lato*), integrating Sentinel-2 L2A, Sentinel-1 SAR, and GEDI L2A data (v2.0) (**Supplementary Text 1**). A U-Net model [76] was trained for pixel-wise CH prediction using six input bands (five from Sentinel-2 and one from Sentinel-1 VH), with filtered GEDI CH as the target. GEDI RH100 data served as the reference CH dataset[77,78], capturing upper canopy profiles within a 25 m footprint. GEDI footprints were rasterized to 10 m resolution using a center-based collocation strategy. Annual CH predictions were generated from three Sentinel-2 images per tile (within ±6 months of GEDI acquisition), and median composites were applied to reduce noise and temporal inconsistencies. Finally, we produced annual 10 m CH maps in Cloud-

Optimized GeoTIFF format for 2019–2023. Forest pixels were defined based on canopy height, using a threshold of CH ≥ 5 m. This height-based definition follows the approach adopted in the GLAD tree height product[40] and aligns with the tree-height criterion of the FAO FRA forest definition[41]. Although canopy height was mapped at 10 m resolution all subsequent height change and AGC change estimates were conducted at 30 m resolution.

We assessed the CH model performance against independent GEDI RH100 and airborne LiDAR (ALS) data across the Amazon (**see Supplementary Text 2, Text 3 for details**). Two large-scale ALS datasets were used: (1) the EBA project (2016–2018), which includes 667 ALS transects[46,47]; and (2) the Sustainable Landscapes Brazil Project (2008–2018) [48] from which we used 823 transects acquired in 2016–2018, closer to our mapping period. To align the ALS data with our CH maps, we resampled ALS-derived height products to 10 m resolution by assigning the maximum height within each pixel and excluding edge pixels. The maximum height was used as a proxy for RH100 because ALS point-cloud data were not available. Since some ALS tiles contained fewer than 10 valid pixels within our study area, a total of 1,398 ALS maximum CH maps were ultimately used to validate the satellite-derived CH products.

We further produced the 30-m aboveground biomass (AGB) map from the 10-m CH map and a new 1-km wood density (WD) map [79,80] as:

$$AGB = 1.3354 \times (CH \times WD)^{1.8146}$$

The original CH map was resampled using mean aggregation, whereas the WD map was resampled using nearest-neighbor sampling to produce the 30-m AGB map. The AGB model was trained and validated using the field inventory samples (n = 543) from three published studies/datasets: (1) The Longo et al. [42]dataset provides carbon estimates from 40 × 40 m, 50 × 50 m plots and 20 × 500 m transects across 18 Brazilian Amazon sites surveyed between 2011 and 2015; (2) The Dionizio et al. [43]dataset includes 387 forest plots (0.01–0.25 ha) established in the Carajás National Forest between 2014 and 2022, primarily near mining infrastructure, with values averaged for plots reporting identical coordinates; (3) The ForestPlots dataset[44,45] comprises field-derived AGB estimates from forest inventory plots measured between the 1990s and 2010s, most of which are <1 ha, using the three-parameter moist tropical forest equation[81] with regional height models and species-level WD. The details about the data processing and AGB model establishment can be found in **Supplementary Text 4**. We then converted aboveground biomass (AGB; Mg ha$^{-1}$) to aboveground carbon (AGC; Mg C ha$^{-1}$) using a conversion factor of 0.456, following values reported in published studies[82,83].

**Processing height change**

We derived CH change from 2019 to 2022 ($\Delta CH_{2022–2019}$) and processed the data through several steps to remove noise and false trends: (1) To retain spatially coherent and temporally consistent changes, we aimed to apply a full 3D 26-connectivity filter centered on $\Delta CH_{2022–2019}$, which connects each pixel to its eight neighbors in both spatial and temporal dimensions (i.e., using $\Delta CH_{2022–2019}$ and $\Delta CH_{2023–2019}$ as adjacent layers). However, processing the full 3D dataset was computationally prohibitive. As an efficient approximation, we applied two rounds of 17-connectivity filtering: one between $\Delta CH_{2021–2019}$ and $\Delta CH_{2022–2019}$, and another between $\Delta CH_{2022–2019}$ and $\Delta CH_{2023–2019}$. Pixels that remained isolated in both analyses were removed. (2) **For CH gains (ΔCH > 0),** we used the Mann–Kendall trend test[84,85] (**Supplementary Text 5**) to identify the change trends (2019–2022) and removed pixels with weak or inconsistent temporal trends (Mann–Kendall Sum < 6), except where the Tropical Moist Forests (TMF) [13] dataset indicated forest regrowth. **For CH losses (ΔCH < 0)**, we excluded pixels with stable Sentinel-1 VV backscatter (|CV| ≤ 5), unless supported by a strong negative Mann–Kendall trend (Mann–Kendall Sum ≤ −4) or by degradation and deforestation identified in the TMF dataset. (3) We finally used annual canopy cover change (ΔCC, 2019–2022) trained on GEDI canopy cover[86] as a reference (**Supplementary Text 6**). Following previous studies[87,88], forest pixels with |ΔCC| ≤ 2% were treated as undisturbed. Among these, we retained only those where ΔCC and ΔCH exhibited the same direction of change, while inconsistent cases were excluded.

Based on these processing steps, we can filter out noise pixels to better detect real CH changes. By incorporating multiple reference datasets (e.g., TMF, Sentinel-1, canopy cover), we can reduce the risk of mistakenly removing real change pixels. To check the variation in change pixels at above three steps, we compared the number of CH-loss pixels with original CH change data (**Supplementary Table 13**). The results show that the filtering primarily excluded pixels with CH change < 10 m (14.1%–77.3%), while only 0%–4.2% of pixels were removed when CH loss exceeded 20 m. Based on 30-m CH change, we calculated the responding 30-m AGC change based on our fitted empirical allometric model between CH and AGB.

**Evaluating height and biomass change maps**

We evaluated CH loss after each processing step against several disturbance datasets that are independent of GEDI data, including TMF[13], Global Forest Change (GFC)[22], and Radar for Detecting Deforestation (RADD)[23] (see **Supplementary Table 2**). No suitable forest gain dataset was available for comparison during 2019–2022. Although TMF v2024 includes some regrowth

pixels for 2019–2021, they account for only a small portion of observed forest height gains. Some increases likely reflect structural recovery, natural growth, or undetected post-disturbance changes not captured by TMF.

The TMF dataset provides 30 m resolution disturbance maps across tropical moist forests from single-date classification of Landsat imagery and trajectory analysis, capturing deforestation, degradation, and regrowth (i.e. regeneration after deforestation) since 1990. The GFC dataset, derived from time-series analysis of Landsat imagery, characterizes global tree cover loss at 30 m resolution since 2001. RADD alerts, generated from Sentinel-1 radar imagery, offer near-real-time disturbance detection in primary humid tropical forests at 10 m resolution since 2020 (in the Amazon). While GFC and RADD primarily detect tree cover loss, the TMF dataset distinguishes non-permanent disturbances (i.e. forest degradation) from permanent disturbances (i.e. deforestation) followed or not by regrowth. The results showed high agreement between CH loss and disturbances from GFC and TMF, with precision exceeding 80% when CH loss was less than –20 m (**Supplementary Fig. 21**). The CH change processing notably improved the match with TMF degradation for small losses (–6 to 0 m), increasing precision by approximately 10%.

We compared the CH change maps after the above processing steps with RH100 changes derived directly from GEDI footprint data at the same period (2019–2022). However, direct comparison between CH change maps and RH100 changes derived from GEDI footprint data is limited by several factors. GEDI data are subject to geolocation uncertainty (~10 m) and seasonal phenological variation[89], while Sentinel-2–derived CH estimates may be influenced by point spread function, adjacency effects, and atmospheric correction errors[90]. Additionally, the low density of repeat GEDI acquisitions and the lack of overlapping footprints between years make footprint-level change detection infeasible. Additionally, because repeat GEDI footprints occur irregularly and sparsely without a fixed repeat orbit, there are limited overlaps between years, which constrains footprint-level change detection at broad scales, even though some studies have exploited near-coincident measurements to detect changes where they occur[37]. To address these limitations, we used high-quality, high-sensitivity GEDI L2A observations (v2.0) (**Supplementary Table 2**), selected based on established quality criteria[91,92] and aggregated both CH and RH100 changes to grid cells of varying sizes (30 m to 100 km). RH100 change was computed as the difference in mean RH100 values per grid cell between 2019 and 2022 across all forest areas. We compared CH and RH100 changes at different spatial resolutions and found that their agreement improves as the

resolution becomes coarser (**Supplementary Fig. 22–24**). CH change estimates had a mean absolute error (MAE) of ~5 m at finer resolutions, which improved to 3.62 m when aggregated to 5 km. These results suggest that coarser-scale comparisons provide a more robust basis for evaluating CH change estimates derived from optical data.

We evaluated our satellite-derived height change using two recent repeat ALS datasets from the Caxiuanã and Jamari National Forests[49-52], which provide original point cloud data acquired during 2019–2022. Following the same processing pipeline (see **Supplementary Text 2**), we generated 1 m resolution canopy height models and aggregated the maximum height to 10 m resolution. To validate CH changes, we compared height differences from both ALS and satellite data at 10 m and 30 m resolutions, considering only reliable height changes from both sources. As the ALS acquisitions mostly cover intact forests as indicated by the TMF data, observed changes were generally small (<5 m), and some fine-scale canopy gaps or rapid regrowth events detected by ALS were not captured by our satellite-derived height change (**Supplementary Fig. 17**).

We also used independent high-resolution datasets of tree cover loss, fire, and logging to evaluate the performance of CH change in the Brazilian state of Mato Grosso. These datasets were derived from 5 m Planet NICFI imagery using a U-Net deep learning model[53,54]. The tree cover loss dataset provides monthly maps from 2016 to 2024 at 5 m resolution, showing relatively consistent agreement with the official Brazilian deforestation map (67.2%) [54]. Logging- and fire-related degradation events were mapped from 2016 to 2023 at six-month intervals, outperforming existing products (F1 = 68.9 for logging; F1 = 75.6 for fire) [53]. To ensure temporal consistency with our CH change data, we selected tree cover loss, fire, and logging detections from June 2019 to June 2022. We then compared mean CH change with the ratios of tree cover loss, fire, and logging events across grid cells ranging from 10 m to 50 km, assessing the detection rate of CH-derived height loss as follows:

$$Detection\ rate = \frac{Height\ loss\ \cap Disturbance}{Disturbance}$$

This detection rate measures the ability of CH-derived height loss to detect independent disturbance events (e.g., tree cover loss, fire, logging). We also examined the relationship between tree cover loss and height change, and evaluated how consistently tree cover loss detected height loss.

To assess the reliability of mapped CH changes, we conducted two complementary visual validation exercises using high-resolution (5 m) PlanetScope imagery. First, we performed an

independent validation of mapped CH-loss and CH-gain patches by stratifying samples[93] according to patch-size class (0–2, 2–10, and 10–100 ha) and change type (gain and loss) (**Supplementary Fig. 25**). We visually interpreted 581 loss patches and 522 gain patches by comparing PlanetScope imagery acquired in 2019 and 2022 and assessing whether the mapped CH change was consistent with visible canopy change within the corresponding gain or loss area, recognizing that some patches may contain both gain and loss signals. User's accuracy was calculated for each patch-size class, together with an area-weighted accuracy[93] to account for the disproportionate contribution of larger patches to the total mapped change (**Supplementary Table 3**). Because this validation relied on visual interpretation of optical imagery, its sensitivity is inherently limited for detecting disturbances in very small patches. Disturbance patches occupying only a few PlanetScope pixels may not exhibit sufficiently distinct visual signatures to be confidently identified, particularly where canopy changes are spatially fragmented or partially obscured by surrounding intact canopy. Consequently, the estimated user's accuracy for the smallest patch-size class should be regarded as conservative, as some true CH-change patches may not be visually distinguishable from PlanetScope imagery alone.

To further evaluate the reliability of CH-loss detections across different loss magnitudes, we conducted an additional visual assessment using randomly sampled 2-ha and 5-ha image chips extracted from the mapped CH-change layer (**Supplementary Fig. 25, Fig. 26**). The image-chip sizes refer to the area of the sampled image subsets rather than the size of individual CH-loss patches, because CH changes cannot be reliably interpreted at the individual-pixel level using optical imagery alone. Image chips were stratified according to their mean estimated CH-loss magnitude ($-2 \leq \Delta CH < 0$ m, $-5 \leq \Delta CH < -2$ m, $-10 \leq \Delta CH < -5$ m, and $-15 \leq \Delta CH < -10$ m) (**Supplementary Table 4**). Monthly PlanetScope imagery acquired in 2019 and 2022 was visually interpreted to determine whether canopy loss was present within each sampled image chip. As with the patch-based validation, this image-chip assessment is also constrained by the detectability of canopy disturbance in optical imagery. Small-magnitude CH losses often produce only subtle visual changes in PlanetScope imagery, even when real CH reductions are present. Consequently, the estimated detection reliability for the lower CH-loss magnitude classes should also be regarded as conservative, because some true low-magnitude CH-loss events may not be visually distinguishable from optical imagery alone. This assessment was designed to quantify the reliability of CH-loss detection (true and false detections) across different CH-loss magnitude classes, rather than to validate the quantitative accuracy of the estimated CH-loss values, which cannot be independently assessed by visual interpretation alone.

We also compared CH-derived AGC changes with AGC change estimates from L-VOD data [94]. This dataset provides annual AGC maps for Amazonian forests from 2010 to 2020 at 100 m spatial resolution, downscaled from 25 km L-VOD-derived AGC data[94] using a constrained statistical disaggregation model. Due to the unavailability of L-VOD data for 2021 and 2022, we used available data between 2017 and 2020 for comparison. We first compared the CH-derived AGC map for 2019 with the 2019 AGC map derived from L-VOD, to evaluate consistency in absolute AGC values. Then, we compared average AGC changes over a three-year period: 2019–2022 from our CH data, and 2017–2020 from the L-VOD dataset. Although the time periods do not fully overlap, this comparison provides a useful indication of agreement in spatial AGC change patterns (**Supplementary Fig. 44)**.

**Mapping of biomass carbon change patterns across disturbance types**

AGC change data were categorized into deforestation, degradation, regrowth, and other forest areas by integrating CH change magnitude with TMF disturbance classes [13]. These classes are broadly based on the disturbance and recovery definitions used in the TMF dataset, which relies on long-term satellite observations. However, TMF does not directly capture forest height loss or gain, and we observed discrepancies between TMF classifications and our height change estimates. To address this, we used TMF as a reference to determine typical ranges of height change for different disturbance types, and applied height loss thresholds from our observations (**Supplementary Fig. 27**) and results reported in previous studies[34] to separate deforestation and degradation losses. In contrast, gains could not be reliably distinguished using thresholds alone, so we trained a model using height increases overlapping TMF-regrowth and forests recovering from degradation. Remaining areas with minimal height variation (≤ 5 m) in forests classified as 'undisturbed' since 1990 by TMF were labeled as 'other' (see **Supplementary Text 9** for details). Because of the limited temporal coverage of the CH-derived change data (2019–2022), distinctions between natural forests, plantations, and afforestation could not be derived from CH changes.

To assess the influence of patch size on AGC density change rates and totals, we analyzed AGC change associated with CH–derived regrowth, degradation, and deforestation patches. Patch size was calculated as the area of each connected region (8-neighbour connectivity). We defined small-scale disturbance events as areas smaller than 2 ha[19]. In addition, patch size was classified into four categories: <2 ha, 2–20 ha, 20–100 ha, and >100 ha. We also considered subtle height loss events involving canopy height reductions of less than 5 m[34], which have largely been overlooked in previous studies. We quantified total carbon losses in regions experiencing CH loss that were not

identified as disturbed in Landsat-based datasets, and compared them to losses associated with mapped disturbances. We overlaid our carbon data with previous disturbance datasets, including TMF[13], GFC [22], RADD[23], to quantify the associated carbon losses across varying patch sizes and height losses.

To evaluate the effectiveness of conservation and land-use policies, we quantified AGC changes within the entire Amazon and protected areas using the AGC change map for 2019–2022. Boundaries of officially designated protected areas from all management categories were obtained from the World Database on Protected Areas (WDPA), downloaded in March 2025 and documented according to the User Manual v1.6 (UNEP-WCMC 2019) [62]. AGC change patterns were compared across the Amazon and protected areas. To facilitate comparison across regions with heterogeneous patch-size distributions and wide size ranges, patch sizes were grouped into 51 logarithmically spaced bins from 0.01 to 100,000 ha. Furthermore, based on long-term TMF disturbance histories, we quantified AGC density changes across years of degradation and regrowth, stratified by different patch sizes. Our results focus on 20-years TMF disturbances preceding our observation period (2019–2022). Although TMF data extend back to 1990, the number of valid observations is lower before 2000, which may affect the detection of short-duration disturbances. Moreover, older disturbances contribute minimally to recent AGC changes, with a flattening trend over time. Full results for 1990–2022 are shown in **Supplementary Fig. 36**.

**Identifying drivers of biomass carbon change**

To attribute AGC loss to specific drivers, we integrated multiple spatial datasets. As a baseline, we used the 1-km forest loss driver dataset (2001–2022 v1.0) developed by the World Resources Institute (WRI) and Google DeepMind[69]. This dataset classified forest loss into seven categories: permanent agriculture, hard commodities, shifting cultivation, logging, wildfires, settlements and infrastructure, and other natural disturbances. Pixels with AGC loss at 1-km resolution that were not assigned a driver in this dataset were treated as ‘uncertain’. The reported overall classification accuracy of the WRI driver dataset was 90.7 ± 3.0% in Latin America[69]. However, because the driver map was produced at 1-km spatial resolution, it may not fully capture fine-scale disturbance heterogeneity observed in the 30-m AGC change maps.

To reduce this uncertainty, we incorporated two additional datasets. First, we used the Global Annual Burned Area Map (GABAM, 30 m, 1990–2021) [70] to identify burned areas across the Amazon, focusing on 2019–2021 but also considering fires from 2014–2018 to better capture legacy fire effects during more fire-active years [95], and wildfires during this earlier period may still

673 have influenced forest changes in 2019–2022. These burned areas were merged with the "wildfire"
674 class in the WRI dataset. We focused on WRI pixels with AGC loss but no assigned driver.
675 Although other datasets provide fire attribution based on tree cover loss[96], they do not align well
676 with our AGC change data. GABAM allowed us to capture fire-related disturbances coinciding
677 with AGC loss, improving attribution in these cases. The validation showed commission and
678 omission errors of 13.17% and 30.13%[70], respectively, indicating that some fire-related
679 disturbances may remain undetected.
680 We further incorporated a 5-m road map[71], from which road fraction was derived as the
681 proportion of road pixels within each 30-m grid cell to identify settlement and infrastructure areas.
682 Where both burn and road pixels occurred within the same 1-km grid cell, we compared their area
683 fractions and assigned the driver with the larger proportion. Finally, we used the Amazon
684 degradation driver map[14] to supplement information on logging and drought, particularly for pixels
685 initially labeled as uncertain or natural disturbances. This dataset helps clarify the spatial patterns
686 of degradation drivers. However, due to its relatively coarse resolution (0.09°–0.5°) and temporal
687 coverage (2001–2018), it is best suited as a complementary source. It also helped detect additional
688 low-density logging events that were not attributed in the WRI dataset, likely due to its 1 km
689 resolution which limits attribution of small-scale or diffuse disturbances. This procedure yielded an
690 updated forest loss driver dataset, from which we calculated net AGC change attributable to each
691 driver category. To approximately account for uncertainty in driver attribution, we used the reported
692 overall classification accuracy of the WRI dataset (90.7 ± 3.0%) as a conservative approximation
693 of attribution uncertainty when calculating driver-specific AGC change. However, because
694 independent reference data for all disturbance categories are currently unavailable, category-
695 specific attribution uncertainty remains difficult to quantify and may vary among disturbance types
696 and spatial contexts. In addition, Because forest degradation often involves diffuse and overlapping
697 disturbance processes, uncertainty in degradation driver attribution remains higher than for large-
698 scale deforestation. Integrating multiple complementary datasets helped reduce attribution
699 uncertainty. Note that multiple disturbance processes may coexist within a single 1-km grid cell,
700 introducing uncertainty in driver attribution. Therefore, the identified drivers should be interpreted
701 as dominant disturbance associations rather than exact causal attribution at the pixel level. The AGC
702 change associated with the original WRI loss driver map can be found in **Supplementary Fig. 45.**
703 Furthermore, we assessed the influence of roads[71] by calculating road fractions at 30-m
704 resolution and examining AGC loss as a function of distance to roads. To test the robustness of road
705 definition, we applied different road-fraction thresholds (0.1, 0.2, 0.3) and compared AGC

responses across these definitions. In addition, we assessed the impacts of burned area fraction[70], logging, and forest edge areas[17] on total AGC change and mean AGC density change. This helps clarify how the frequency of these disturbance events contributes to aboveground carbon loss in the Amazon.

**Quantifying uncertainty in biomass carbon change**

We quantified total biomass carbon change across the whole region, as well as within protected areas, based on contributions from forest regrowth following deforestation, degradation, deforestation, and other forest changes. We further estimated the total uncertainty ($\sigma_{Total}$) in biomass carbon change by accounting for three sources of error:

$$\sigma_{Total} = \sqrt{\sigma_{AGC}^2 + \sigma_{class}^2 + \sigma_{detect}^2}$$

where $\sigma_{AGC}$ represents the uncertainty associated with the estimation of AGC change, $\sigma_{class}$ denotes the classification uncertainty, and $\sigma_{detect}$ represents the uncertainty in CH loss and gain detection. Although these uncertainty components may partially overlap in practice, we conservatively assumed them to be independent during uncertainty propagation.

(1) $\sigma_{AGC}$ was evaluated via 100 bootstrap iterations of the AGB model, formulated as $AGB = a \times (CH \times WD)^b$. In each iteration, a new training sample was drawn with replacement and used to re-fit the model, generating distributions of the fitted parameters a and b. The resulting mean and standard deviation of these parameters were used to propagate model uncertainty in AGB estimation[27]. For each region, we calculated the coefficient of variation (CV) of total AGC change across the 100 bootstrap realizations to quantify $\sigma_{AGC}$.

(2) $\sigma_{class}$ was assessed across six forest-change classes, including CH > 0 (other, regrowth, and degraded forest) and CH < 0 (other, deforested, and degraded forest). As these classes were derived from CH-change thresholds and TMF labels, and no ground-truth classification error was available, we re-trained an XGBoost model to predict these classes using the existing labels. We then calculated the weighted average of precision and recall across classes to estimate mean classification accuracy (**Supplementary Table 14**), which was used as a proxy for $\sigma_{class}$. Since degradation and deforestation were defined by threshold-based class separation, misclassification in one implies a corresponding error in the other. Therefore, we assumed comparable uncertainty in these two classes and used their mean uncertainty in subsequent analyses.

(3) $\sigma_{detect}$ associated with CH change detection was estimated from the independent visual validation results. Specifically, we treated the complements of the area-weighted user's accuracies (24.5% for CH loss and 27.5% for CH gain; Supplementary Table 3) as bounded Type-B

uncertainties under a uniform distribution assumption[97]. Detection uncertainty was then computed by treating the classification error $(1 - Accuracy)$ as a bounding interval rather than a standard deviation. The corresponding relative detection uncertainties were estimated as $(1 - Accuracy)/\sqrt{3}$ and propagated independently together with biomass estimation and classification uncertainties. This uncertainty primarily reflects residual mapping noise and the inherent difficulty of visually identifying subtle CH changes, particularly for very small patches with low-magnitude CH variations.

For analyses involving disturbance-driver attribution, an additional uncertainty term associated with the driver classification map was included in the error propagation framework. This uncertainty was estimated from the reported overall classification accuracy of the WRI driver dataset in Latin America, corresponding to a relative attribution uncertainty of 9.3%. Driver attribution uncertainty was propagated independently together with biomass estimation uncertainty and canopy height change detection uncertainty using quadratic error propagation to estimate uncertainties associated with AGC gain, loss, and net change across different disturbance drivers.

**Acknowledgements**

We are grateful to the support from the European Space Agency Climate Change Initiative (ESA-CCI) RECCAP2-CS project (ESA ESRIN/4000144908/24/I-LR), and the One Forest Vision initiative, funded by the French Ministry of Higher Education and Research and the French Ministry for Europe and Foreign Affairs. We also acknowledge the support from the CALIPSO (Carbon Loss in Plant Soils and Oceans) project funded through the generosity of Schmidt Science. This work was granted access to the HPC resources of IDRIS under the allocation 2025-[AD010114718R1] made by GENCI. We are grateful to HighTide and Grantham Foundations for their support of scientific research at CTrees.org. We acknowledge the open access to Sentinel-1/-2 imagery provided by the European Space Agency and GEDI datasets from NASA. We acknowledge a European Research Council grant to Rupert Seidl under the European Union's Horizon 2020 research and innovation programme that supported Fabian Jörg Fischer (grant agreement no.: 101001905, FORWARD). Many thanks to all investigators and researchers for their significant efforts in collecting the field plot and ALS data used in this study.

**Author contributions**

The paper was conceived and the initial draft prepared by LW and PC. LW, PC, AdT, and ES developed and validated the data and mapping products. FJF, RD, CB, AF, FHW, SL, and SS

provided relevant reference datasets for model validation and analysis. LW, PC, FJF, RD, CB, AF, JW, LEOCA, and JPO contributed to shaping the structure of the manuscript. All authors contributed to the interpretation of the results and to writing the manuscript.

## Data availability

The TMF data are available at https://forobs.jrc.ec.europa.eu/TMF. The tree cover loss from GFC can be accessed from https://glad.earthengine.app/view/global-forest-change. The RADD Forest Disturbance Alert data were available at https://gee-community-catalog.org/projects/radd/. The WRI loss driver data can be accessed from https://zenodo.org/records/14163025. The burned-area dataset can be accessed from https://gee-community-catalog.org/projects/gabam/. The ALS and field inventory datasets used for model development and validation are openly available through the references and Supplementary Information. The code and additional maps of biomass and canopy height changes will be fully released online upon acceptance.

## References


1 Walker, W. S. *et al.* The role of forest conversion, degradation, and disturbance in the carbon dynamics of Amazon indigenous territories and protected areas. *Proceedings of the National Academy of Sciences* **117**, 3015-3025 (2020).

2 Soares-Filho, B. *et al.* Role of Brazilian Amazon protected areas in climate change mitigation. *Proceedings of the National Academy of Sciences* **107**, 10821-10826 (2010).

3 Fendrich, A. *et al.* Human influence on Amazon's aboveground carbon dynamics intensified over the last decade. *Nature Communications* **16**, 6681 (2025). https://doi.org:10.1038/s41467-025-61856-1

4 Fawcett, D. *et al.* Declining Amazon biomass due to deforestation and subsequent degradation losses exceeding gains. *Global Change Biology* **29**, 1106-1118 (2023).

5 Griscom, B. W. *et al.* Natural climate solutions. *Proceedings of the National Academy of Sciences* **114**, 11645-11650 (2017).

6 Mitchard, E. T. The tropical forest carbon cycle and climate change. *Nature* **559**, 527-534 (2018).

7 Ciais, P. *et al.* in *Climate Change 2013: The Physical Science Basis. Contribution of Working Group I to the Fifth Assessment Report of the Intergovernmental Panel on Climate Change Change* 465-570 (Cambridge University Press, 2014).

8 Matricardi, E. A. T. *et al.* Long-term forest degradation surpasses deforestation in the Brazilian Amazon. *Science* **369**, 1378-1382 (2020).
9 Pan, Y. *et al.* The enduring world forest carbon sink. *Nature* **631**, 563-569 (2024).
10 Silveira, M. V. *et al.* Observed shifts in regional climate linked to Amazon deforestation. *Communications Earth & Environment* **6**, 948 (2025).
11 Qin, Y. *et al.* Carbon loss from forest degradation exceeds that from deforestation in the Brazilian Amazon. *Nature Climate Change* **11**, 442-448 (2021).
12 Bourgoin, C. *et al.* Human degradation of tropical moist forests is greater than previously estimated. *Nature* **631**, 570-576 (2024).
13 Vancutsem, C. *et al.* Long-term (1990–2019) monitoring of forest cover changes in the humid tropics. *Science advances* **7**, eabe1603 (2021).
14 Lapola, D. M. *et al.* The drivers and impacts of Amazon forest degradation. *Science* **379**, eabp8622 (2023).
15 Gatti, L. V. *et al.* Increased Amazon carbon emissions mainly from decline in law enforcement. *Nature* **621**, 318-323 (2023).
16 MapBiomas – Collection 9 of annual series of Maps of mining of Brazil, accessed on GEE through the link: https://brasil.mapbiomas.org/.
17 Siqueira-Gay, J., Metzger, J. P., Sánchez, L. E. & Sonter, L. J. Strategic planning to mitigate mining impacts on protected areas in the Brazilian Amazon. *Nature Sustainability* **5**, 853-860 (2022).
18 Kalamandeen, M. *et al.* Pervasive rise of small-scale deforestation in Amazonia. *Scientific reports* **8**, 1600 (2018).
19 Xu, Y. *et al.* Small persistent humid forest clearings drive tropical forest biomass losses. *Nature* **649**, 375-380 (2026).
20 Heinrich, V. H. A. *et al.* Large carbon sink potential of secondary forests in the Brazilian Amazon to mitigate climate change. *Nature Communications* **12**, 1785 (2021). https://doi.org:10.1038/s41467-021-22050-1
21 Liu, S. *et al.* Mapping previously undetected trees reveals overlooked changes in pan-tropical tree cover. *Nature Communications* **16**, 5561 (2025).
22 Hansen, M. C. *et al.* High-resolution global maps of 21st-century forest cover change. *science* **342**, 850-853 (2013).
23 Reiche, J. *et al.* Forest disturbance alerts for the Congo Basin using Sentinel-1. *Environmental Research Letters* **16**, 024005 (2021).

24 Silva Junior, C. H. *et al.* Benchmark maps of 33 years of secondary forest age for Brazil. *Scientific data* **7**, 269 (2020).

25 Santoro, M. & Cartus, O. ESA Biomass Climate Change Initiative (Biomass_cci): Global datasets of forest above-ground biomass for the years 2007, 2010, 2015, 2016, 2017, 2018, 2019, 2020, 2021 and 2022, v6.0. *NERC EDS Centre for Environmental Data Analysis* (2025). https://doi.org:https://dx.doi.org/10.5285/95913ffb6467447ca72c4e9d8cf30501

26 Xu, L. *et al.* Changes in global terrestrial live biomass over the 21st century. *Science Advances* **7**, eabe9829 (2021).

27 Yang, H. *et al.* Global increase in biomass carbon stock dominated by growth of northern young forests over past decade. *Nature Geoscience* **16**, 886-892 (2023).

28 Bourgoin, C. *et al.* Human degradation of tropical moist forests is greater than previously estimated. *Nature* **631**, 570-576 (2024). https://doi.org:10.1038/s41586-024-07629-0

29 Dupuis, C., Fayolle, A., Bastin, J.-F., Latte, N. & Lejeune, P. Monitoring selective logging intensities in Central Africa with sentinel-1: a canopy disturbance experiment. *Remote Sensing of Environment* **298**, 113828 (2023).

30 Nunes, M. H. *et al.* Edge effects on tree architecture exacerbate biomass loss of fragmented Amazonian forests. *Nature Communications* **14**, 8129 (2023). https://doi.org:10.1038/s41467-023-44004-5

31 Flores, B. M. *et al.* Critical transitions in the Amazon forest system. *Nature* **626**, 555-564 (2024). https://doi.org:10.1038/s41586-023-06970-0

32 Siqueira-Gay, J., Soares-Filho, B., Sanchez, L. E., Oviedo, A. & Sonter, L. J. Proposed Legislation to Mine Brazil's Indigenous Lands Will Threaten Amazon Forests and Their Valuable Ecosystem Services. *One Earth* **3**, 356-362 (2020). https://doi.org:10.1016/j.oneear.2020.08.008

33 Wagner, F. H. *et al.* High Resolution Tree Height Mapping of the Amazon Forest using Planet NICFI Images and LiDAR-Informed U-Net Model. *arXiv preprint arXiv:2501.10600* (2025).

34 Jackson, T. D. *et al.* Tall Bornean forests experience higher canopy disturbance rates than those in the eastern Amazon or Guiana shield. *Global Change Biology* **30**, e17493 (2024).

35 Heinrich, V. H. A. *et al.* The carbon sink of secondary and degraded humid tropical forests. *Nature* **615**, 436-442 (2023). https://doi.org:10.1038/s41586-022-05679-w

36 Duncanson, L. *et al.* Aboveground biomass density models for NASA's Global Ecosystem Dynamics Investigation (GEDI) lidar mission. *Remote Sensing of Environment* **270**, 112845 (2022).

37 Holcomb, A., Burns, P., Keshav, S. & Coomes, D. A. Repeat GEDI footprints measure the effects of tropical forest disturbances. *Remote Sensing of Environment* **308**, 114174 (2024). https://doi.org:https://doi.org/10.1016/j.rse.2024.114174

38 Milenković, M. *et al.* Assessing Amazon rainforest regrowth with GEDI and ICESat-2 data. *Science of Remote Sensing* **5**, 100051 (2022).

39 Dubayah, R. *et al.* GEDI L2A elevation and height metrics data global footprint level V002. *NASA EOSDIS Land Processes Distributed Active Archive Center (DAAC) data set*, GEDI02_A. 002 (2021).

40 Potapov, P. *et al.* The global 2000-2020 land cover and land use change dataset derived from the Landsat archive: first results. *Frontiers in Remote Sensing* **3**, 856903 (2022).

41 FAO. Global Forest Resources Assessment 2020: Main report. Rome. (2020).

42 Longo, M. *et al.* Aboveground biomass variability across intact and degraded forests in the Brazilian Amazon. *Global Biogeochemical Cycles* **30**, 1639-1660 (2016).

43 Dionizio, E. A. *et al.* Aboveground carbon stocks for different forest types in eastern Amazonia. *Environmental Research Communications* **7**, 045006 (2025).

44 Mitchard, E. T. *et al.* Markedly divergent estimates of A mazon forest carbon density from ground plots and satellites. *Global ecology and biogeography* **23**, 935-946 (2014).

45 Lopez-Gonzalez, G. *et al.* Amazon forest biomass measured in inventory plots. Plot Data from 'Markedly divergent estimates of Amazon forest carbon density from ground plots and satellites'. (2014).

46 Ometto, J. P. *et al.* A biomass map of the Brazilian Amazon from multisource remote sensing. *Scientific Data* **10**, 668 (2023).

47 Ometto, J. L3A-Summary of Airborne LiDAR transects collected by EBA in the Brazilian Amazon. *Zenodo https://doi. org/10.5281/zenodo* **4968706** (2021).

48 Dos-Santos, M., Keller, M. & Morton, D. LiDAR surveys over selected forest research sites, Brazilian Amazon, 2008-2018. *ORNL DAAC, Oak RIdge, Tennessee, USA* (2019).

49 Brasileiro, S. F. & José Humberto, C. LiDAR data collected in the Caxiuanã National Forest, State of Pará, Brazil, in the year 2022. (2025).

50 Brasileiro, S. F. & José Humberto, C. LiDAR data collected in the Caxiuanã National Forest, State of Pará, Brazil, in the years 2018, 2019, 2020 and 2021. (2025).

51 Brasileiro, S. F. & Chaves, J. H. LiDAR data collected in the Jamari National Forest, State of Rondônia, Brazil, in the years 2018, and 2019. (2025).

52 Brasileiro, S. F. & Chaves, J. H. LiDAR data collected in the Jamari National Forest, State of Rondônia, Brazil, in the year 2022. (2025).

53 Dalagnol, R. *et al.* Mapping tropical forest degradation with deep learning and Planet NICFI data. *Remote Sensing of Environment* **298**, 113798 (2023). https://doi.org:https://doi.org/10.1016/j.rse.2023.113798

54 Wagner, F. H. *et al.* Mapping tropical forest cover and deforestation with planet NICFI satellite images and deep learning in Mato Grosso State (Brazil) from 2015 to 2021. *Remote Sensing* **15**, 521 (2023).

55 Welsink, A.-J. *et al.* Monitoring fine-scale natural and logging-related tropical forest degradation using Sentinel-1. *Remote Sensing of Environment* **328**, 114878 (2025).

56 Cushman, K., Detto, M., García, M. & Muller‐Landau, H. C. Soils and topography control natural disturbance rates and thereby forest structure in a lowland tropical landscape. *Ecology Letters* **25**, 1126-1138 (2022).

57 Csillik, O. *et al.* A large net carbon loss attributed to anthropogenic and natural disturbances in the Amazon Arc of Deforestation. *Proceedings of the National Academy of Sciences* **121**, e2310157121 (2024). https://doi.org:doi:10.1073/pnas.2310157121

58 Barber, C. P., Cochrane, M. A., Souza Jr, C. M. & Laurance, W. F. Roads, deforestation, and the mitigating effect of protected areas in the Amazon. *Biological conservation* **177**, 203-209 (2014).

59 Sonter, L. J. *et al.* Mining drives extensive deforestation in the Brazilian Amazon. *Nature communications* **8**, 1013 (2017).

60 Tyukavina, A. *et al.* Types and rates of forest disturbance in Brazilian Legal Amazon, 2000–2013. *Science advances* **3**, e1601047 (2017).

61 Fadrique, B., Gann, D., Nelson, B. W., Saatchi, S. & Feeley, K. J. Bamboo phenology and life cycle drive seasonal and long‐term functioning of Amazonian bamboo‐dominated forests. *Journal of Ecology* **109**, 860-876 (2021).

62 Unep-Wcmc, I. Protected Planet: The World Database on Protected Areas (WDPA) and World Database on Other Effective Area-based Conservation Measures (WD-OECM). *Cambridge, UK: UNEP-WCMC and IUCN* (2025).

933 63 Qin, Y. *et al.* Forest conservation in Indigenous territories and protected areas in the
934 Brazilian Amazon. *Nature Sustainability* **6**, 295-305 (2023).
935 https://doi.org:10.1038/s41893-022-01018-z
936 64 Wolf, C., Levi, T., Ripple, W. J., Zárrate-Charry, D. A. & Betts, M. G. A forest loss report
937 card for the world's protected areas. *Nature Ecology & Evolution* **5**, 520-529 (2021).
938 65 Marengo, J. A. & Espinoza, J. C. Extreme seasonal droughts and floods in Amazonia: causes,
939 trends and impacts. *International Journal of Climatology* **36**, 1033-1050 (2016).
940 66 Albert, J. S. *et al.* Human impacts outpace natural processes in the Amazon. *Science* **379**,
941 eabo5003 (2023).
942 67 Robinson, N. *et al.* Protect young secondary forests for optimum carbon removal. *Nature*
943 *Climate Change*, 1-8 (2025).
944 68 Cook-Patton, S. C. *et al.* Mapping carbon accumulation potential from global natural forest
945 regrowth. *Nature* **585**, 545-550 (2020).
946 69 Sims, M. J. *et al.* Global drivers of forest loss at 1 km resolution. *Environmental Research*
947 *Letters* **20**, 074027 (2025).
948 70 Long, T. *et al.* 30 m resolution global annual burned area mapping based on Landsat Images
949 and Google Earth Engine. *Remote Sensing* **11**, 489 (2019).
950 71 Liu Shidong, C. P., Zhang Jie, Penuelas Josep, Ding Shengping, Nath Biswajit, Song
951 Wanjuan, Wu Xia, Zhang Yaping, Jacquet Iskid, Li Wang, Huang Ni, Niu Zheng, Wang Li.
952 Road-induced fragmentation endangers half of the global tropical tree cover. *In preparation*
953 (2025).
954 72 Espírito-Santo, F. D. B. *et al.* Size and frequency of natural forest disturbances and the
955 Amazon forest carbon balance. *Nature Communications* **5**, 3434 (2014).
956 https://doi.org:10.1038/ncomms4434
957 73 Duncanson, L. *et al.* The effectiveness of global protected areas for climate change
958 mitigation. *Nature Communications* **14**, 2908 (2023).
959 74 Nobre, C. A. *et al.* Land-use and climate change risks in the Amazon and the need of a novel
960 sustainable development paradigm. *Proceedings of the National Academy of Sciences* **113**,
961 10759-10768 (2016).
962 75 Mataveli, G. & de Oliveira, G. Protect the Amazon's Indigenous lands. *Science* **375**, 275-
963 276 (2022).

76 Ronneberger, O., Fischer, P. & Brox, T. in *Medical image computing and computer-assisted intervention–MICCAI 2015: 18th international conference, Munich, Germany, October 5-9, 2015, proceedings, part III 18.* 234-241 (Springer).

77 Qi, W. & Dubayah, R. O. Combining Tandem-X InSAR and simulated GEDI lidar observations for forest structure mapping. *Remote sensing of Environment* **187**, 253-266 (2016).

78 Pauls, J. *et al.* Estimating canopy height at scale. *arXiv preprint arXiv:2406.01076* (2024).

79 Fischer, F. J. *et al.* A global map of wood density. *bioRxiv*, 2025.2008.2025.671920 (2025). https://doi.org:10.1101/2025.08.25.671920

80 Fischer, F. J. *et al.* Beyond species means – the intraspecific contribution to global wood density variation. *bioRxiv*, 2025.2008.2025.671896 (2025). https://doi.org:10.1101/2025.08.25.671896

81 Chave, J. *et al.* Tree allometry and improved estimation of carbon stocks and balance in tropical forests. *Oecologia* **145**, 87-99 (2005).

82 Martin, A. R., Doraisami, M. & Thomas, S. C. Global patterns in wood carbon concentration across the world's trees and forests. *Nature Geoscience* **11**, 915-920 (2018).

83 Cuni-Sanchez, A. *et al.* High aboveground carbon stock of African tropical montane forests. *Nature* **596**, 536-542 (2021).

84 Mann, H. B. Nonparametric tests against trend. *Econometrica: Journal of the econometric society*, 245-259 (1945).

85 Kendall, M. G. Rank correlation methods. (1948).

86 Dubayah, R. *et al.* GEDI L2B Canopy Cover and Vertical Profile Metrics Data Global Footprint Level V002. *NASA EOSDIS Land Processes Distributed Active Archive Center (DAAC) data set* (2021).

87 Su, Y. *et al.* Asymmetric influence of forest cover gain and loss on land surface temperature. *Nature Climate Change* **13**, 823-831 (2023).

88 Alkama, R. & Cescatti, A. Biophysical climate impacts of recent changes in global forest cover. *Science* **351**, 600-604 (2016).

89 Roy, D. P., Kashongwe, H. B. & Armston, J. The impact of geolocation uncertainty on GEDI tropical forest canopy height estimation and change monitoring. *Science of Remote Sensing* **4**, 100024 (2021).

90 Lang, N., Jetz, W., Schindler, K. & Wegner, J. D. A high-resolution canopy height model of the Earth. *Nature Ecology & Evolution* **7**, 1778-1789 (2023).

91 de Conto, T., Armston, J. & Dubayah, R. Characterizing the structural complexity of the Earth's forests with spaceborne lidar. *Nature Communications* **15**, 8116 (2024).

92 Burns, P., Hakkenberg, C. R. & Goetz, S. J. Multi-resolution gridded maps of vegetation structure from GEDI. *Scientific Data* **11**, 881 (2024).

93 Olofsson, P. *et al.* Good practices for estimating area and assessing accuracy of land change. *Remote sensing of Environment* **148**, 42-57 (2014).

94 Fan, L. *et al.* Satellite-observed pantropical carbon dynamics. *Nature plants* **5**, 944-951 (2019).

95 Bourgoin, C. *et al.* Extensive fire-driven degradation in 2024 marks worst Amazon forest disturbance in over 2 decades. *Biogeosciences* **22**, 5247-5256 (2025).

96 Tyukavina, A. *et al.* Global trends of forest loss due to fire from 2001 to 2019. *Frontiers in Remote Sensing* **3**, 825190 (2022).

97 Bipm *et al.* Evaluation of measurement data — Guide to the expression of uncertainty in measurement.

**Supplementary information**

# Previously undetected disturbances are the dominant driver of carbon loss in protected Amazonian forests

Liang Wan[1,*], Philippe Ciais[1], Aurélien de Truchis[2], Ewan Sean[2], Fabian Jörg Fischer[3], Ricardo Dalagnol[4], Clément Bourgoin[5], Yidi Xu[1], Nan Meng[1], Xiaojun Li[6], Arthur Fendrich[5], Clément Albergel[7], Youngryel Ryu[8], Stephen Sitch[9], Thais Michele Rosan[9], Jean-Pierre Wigneron[10], Fabien H. Wagner[4], Shidong Liu[11], Lei Zhu[1], Agnès Pellissier-Tanon[1], Ibrahim Fayad[1,2], Gabriel Belouze[1], Clement J. F. Delcourt[1], Sassan Saatchi[4,12], Luiz E. O. C. Aragão[13,9], Jean P. Ometto[13]

**Supplementary Text 1– Text 13**

**Supplementary Fig. 1– Fig. 45**

**Supplementary Table 1– Table 14**

## Supplementary Text 1. Canopy height mapping using a deep learning model

Our study region covers forested land across the Amazon forest (Amazonia *sensu lato*), including Amazonia *sensu stricto*, the Guiana Shield, and Gurupí, based on commonly used geographical definitions of Amazonia[1].

We employed multi-source remote sensing data to produce annual canopy height (CH) maps at 10-m resolution across the Amazon forest, integrating Sentinel-2 L2A, Sentinel-1 SAR, and GEDI L2A data (**Supplementary Fig. 1**)[2]. Sentinel-2 L2A imagery provides atmospherically corrected multispectral data, from which we selected four 10 m bands (B02–B04, B08) and one resampled SWIR band (B11) for their spectral sensitivity to vegetation structure and biochemistry [3]. To mitigate persistent cloud cover in tropical forests [4], we incorporated Sentinel-1 SAR VH polarization from Level-1 GRD IW mode products, which is less affected by atmospheric conditions and strongly responsive to forest structural attributes, particularly in tall and dense forests [5]. Annual mean VH backscatter was used, given its stronger contribution to CH estimation

than VV polarization [6,7]. GEDI RH100 data served as the reference CH data [8,9], capturing upper canopy profiles within a 25 m footprint. RH100 footprints from 2019–2022 were filtered for quality ('quality_flag = 1', num_detectedmodes > 0), and only full-power beams acquired within ±6 months of the Sentinel image dates were retained. GEDI footprints were rasterized to 10 m resolution using a center-based collocation strategy, which has been shown to outperform coarser methods [10].

To construct training and validation datasets, Sentinel-1 VH data were calibrated, orthorectified, and denoised. Ten images from the dry season (June–October) with the lowest VH values were selected per tile to reduce residual moisture effects, and their temporal mean was scaled to [0, 1]. For Sentinel-2, three cloud-free L2A scenes were selected per tile based on ESA masks and water vapor conditions, and all bands were similarly normalized. We trained a U-Net model (Ronneberger *et al.*, 2015) for pixel-wise CH prediction, using six input bands (five Sentinel-2 and one Sentinel-1 VH) and filtered GEDI CH as the target. The model was trained using 80% of the total samples, while the remaining 20% were equally divided into independent validation (10%) and test (10%) datasets to ensure spatial independence. To increase sample diversity and reduce overfitting, we applied data augmentation (random crops, flips, rotations) and randomly sampled acquisition years (2019–2023) per epoch to introduce temporal variation. Training proceeded in two stages: initial training using all high-quality GEDI data, followed by fine-tuning with temporally aligned samples. Annual CH predictions were generated from three cloud-free Sentinel-2 images per tile (within ±6 months of GEDI), and median composites were used to reduce noise and inconsistencies. Final outputs were exported as seamless, annual 10 m CH maps in Cloud-Optimized GeoTIFF format from 2019 to 2023.

**Supplementary Text 2. Reference datasets for canopy height validation**

To clarify the definition of canopy top height at 10 m resolution, we followed the interpretation consistent with GEDI RH100, which represents the highest point within each footprint. Accordingly, our model was trained to predict the maximum canopy height (ALS max height) within each 10 m grid cell. However, we acknowledge that some published height maps were trained using the canopy height as the mean/median of high-resolution returns (ALS mean height), which may lead to systematic underestimation when validating against GEDI-like metrics. To ensure a fair comparison across datasets, we also report validation results using ALS mean height. Related descriptions and results are presented below.

To validate the model performance, we evaluated the CH map against the independent GEDI and ALS height data (**Supplementary Fig. 2**). The independent GEDI RH100 data were derived from the model testing data, not used for model training. The ALS height data were derived from two ALS datasets collected across the Brazilian Amazon forests.

The first ALS dataset was collected for the EBA project between 2016 and 2018, including 667 ALS transects [11,12]. Each transect covered 375 ha (12.5 × 0.3 km) of forested areas across the Brazilian Amazon, with locations stratified by TerraClass primary and secondary forest masks. The ALS data were collected using a Harrier 68i sensor aboard a Cessna 206 aircraft at ~600 m altitude, with a point density exceeding 4 points $m^{-2}$ and vertical/horizontal accuracy of ±0.5 m and ±1.0 m, respectively. We used the classifications of point clouds by Reis, et al. [13]. The CH data were derived by subtracting DTM elevation from vegetation returns, and a 1-m resolution CH model was produced using the pit-free algorithm [14].

The second ALS dataset was collected as part of the Sustainable Landscapes Brazil Project between 2008 and 2018[15]. For this analysis, we used 823 ALS transects acquired in 2016, 2017 and 2018, which is close to our mapping year. The dataset was acquired at a spatial resolution of approximately 10 points per $m^2$, covering key field research sites across the region. The point clouds were georeferenced, noise-filtered, and corrected for misalignments in overlapping flight lines. The data are provided in 1 $km^2$ tiles and are publicly available in LAZ format (https://doi.org/10.3334/ORNLDAAC/1644). To generate CH maps from LAZ point cloud files, we use the PDAL Python package to extract ground points for building a 1-m DTM, and non-ground points for creating a 1-m DSM from the highest returns. The DSM is then reprojected to align with the DTM grid, and the CH data is calculated as the difference between DSM and DTM.

To ensure consistency with the ALS reference data, we resampled all ALS CH maps to a 10-m resolution by taking the maximum height within each original 1-m grid cell. This approach is consistent with our model training strategy, which relies on GEDI top-of-canopy height observations. We evaluated our generated CH map (using the 2019 product as a reference) against several existing published CH datasets (**Supplementary Table 1**), using independent GEDI RH100 measurements and ALS-derived maximum canopy height for validation. Because some published CH products represent mean/median height rather than maximum height (e.g., CTrees [16] and Meta [17]), we additionally validated these datasets using **mean heights** aggregated from the 1-m ALS data.

Most existing CH datasets have spatial resolutions comparable to ours (5–30 m); these products were therefore resampled to 10 m using the nearest-neighbor method. For the Meta CH product, we derived both maximum (**Meta max**) and mean (**Meta mean**) CH at 10-m resolution by aggregating the original 1-m height data. Prior to validation, we applied a morphological dilation filter to the

ALS height maps to remove edge-adjacent pixels, thereby minimizing boundary effects during canopy height model (CHM) computation. Finally, because some ALS tiles contained too few valid pixels (< 10) within our study region, we retained ~1,400 ALS tiles for the final validation of satellite-derived CH products.

**Supplementary Text 3. Evaluation of canopy height mapping**

The generated 10-m CH map shows good agreement with published CH maps, although substantial differences in CH values are observed among them. As shown in **Supplementary Fig. 3**, the CH maps share similar spatial patterns across the dense Amazon forest, such as clearly visible short forests in the northwest and southeast regions, likely due to disturbance events. Our CH map shows a more consistent spatial distribution with the GLAD, GTDX, and ETH maps, with only slight underestimations compared to the GTDX and ETH maps. Although the Meta map offers uniquely high spatial resolution (1 m), it significantly underestimates CH values and exhibits strong artifact effects. The CTrees map (2020–2024), trained using ALS median height data for the 2016–2018 period, generally displays lower CH values. The Pauls CH map, which was generated using a similar method to ours, shows clear underestimations, likely due to the limited number of training samples.

Our CH map demonstrates better performance against the independent GEDI and ALS height data compared to the published CH products. As shown in **Supplementary Fig. 4**, our height estimates achieved the highest accuracy when validated against GEDI RH100 ($R^2$ = 0.78, MAE = 3.83 m), followed by the ETH map ($R^2$ = 0.74, MAE = 4.49 m) and the GTDX map ($R^2$ = 0.72, MAE = 4.89 m). These maps performed better than the GLAD CH map derived from Landsat imagery. The Pauls CH showed a strong correlation with GEDI RH100 but suffered from substantial underestimation. Furthermore, the developed CH maps demonstrated consistent performance across years ($R^2$ = 0.74–0.76; MAE = 3.98–4.19 m) when validated against independent GEDI RH100 data (**Supplementary Fig. 5**). A similar pattern was observed when validated against ALS maximum height data (**Supplementary Fig. 6**): our CH map achieved the best performance ($R^2$ = 0.56, MAE = 4.37 m). Compared to GEDI RH100, our CH map also showed minimal bias (0.14 m), while the ETH and GTDX maps exhibited larger overestimations, with biases of –1.51 m and –2.45 m, respectively. CH maps, such as CTrees and Meta, showed good consistency with ALS mean height (**Supplementary Fig. 7**), but exhibited some underestimations compared to GEDI RH100 values and ALS maximum height (**Supplementary Fig. 4, Supplementary Fig. 6**).

The CH map demonstrates consistently strong performance across varying forest height ranges. As shown in **Supplementary Fig. 8**, the differences between our CH and GEDI RH100 are generally close to the y = 0 line when CH is below 30 m, outperforming the GLAD, GTDX, ETH, CTrees, and Meta CH maps. Although the Pauls CH also shows a reasonable match with GEDI RH100, its performance declines above 20 m. The comparison of model errors (MAE) indicates that our CH map maintains low errors (MAE < 5 m) across height ranges below 35 m. While some underestimations are observed compared to the GTDX CH, our map more accurately captures lower canopy heights. A similar pattern was observed when validating against ALS maximum height data, with a slight overestimation for shorter canopies (**Supplementary Fig. 8b**). Although the Meta and CTrees height maps showed a better agreement with ALS mean height data (**Supplementary Fig. 8c**), they underestimated taller canopies, particularly > 30 m. Overall, these results suggest that our map provides accurate CH estimates across the Amazon forest.

Our CH maps showed good spatial consistency with the ALS-derived maximum CH. The results indicate that our developed CH products successfully capture the spatial patterns of dense forests ($R^2$ = 0.43–0.62; MAE = 4.68–5.64 m; **Supplementary Fig. 9**), although some small biases remain, with a tendency to underestimate canopy height in certain pixels. Compared to our CH maps, the GTDX and ETH products exhibited noticeable overestimations, while the other datasets tended to underestimate CH. In forests affected by disturbances (**Supplementary Fig. 9b, d**), our CH maps revealed clear and consistent disturbance patterns aligned with the ALS CH ($R^2$ = 0.62–0.77; MAE = 4.14–4.84 m). Other CH datasets were less effective in capturing these disturbances, likely due to temporal mismatches in mapping, and showed limited CH contrast between disturbed and undisturbed areas. Furthermore, our CH maps provide finer spatial detail at 10-m resolution than GTDX, ETH, and Pauls products. Although CTrees and Meta maps exhibited greater spatial detail due to their higher resolution, they were less effective in characterizing the top-of-canopy structure.

**Supplementary Text 4. Biomass model establishment and validation**

From the predicted CH maps, we derived the 30-m AGB map using distinct CH-AGB allometric models integrated with the new 1-km WD map [18,19], calibrated with field inventory data as:

$$AGB1 = a \times CH^{b} \quad (1)$$

$$AGB2 = a \times (CH \times WD)^{b} \quad (2)$$

To train the AGB model, we applied cross-validation by using 80% of the field inventory samples (n = 544), the remaining 20% reserved for validation. We used the field inventory data from the published studies: (1) Eighteen Brazilian Amazon study areas were surveyed with 40 × 40 m or 50 × 50 m plots and 20 × 500 m transects to measure live trees, palms, lianas, and snags between 2011 and 2015, applying allometric equations to estimate above-ground carbon stocks in intact versus degraded forests and then converted the aboveground carbon to the AGB based on the ratio of 0.5 [20]; (2) The Carajás National Forest (CNF) in southeastern Pará, Brazil, was surveyed using 387 forest plots of varying sizes (0.01–0.25 ha) established between 2014 and 2022, primarily near mining areas and infrastructure in the eastern CNF, with data collected through environmental and scientific studies. Due to the open-access dataset providing only two decimal places for latitude and longitude, many plots share identical coordinates; in this study, we averaged the AGB values for plots with the same reported location [21]; (3) The ForestPlots dataset [22,23] includes Amazon forest biomass data measured in field inventory plots. The data were collected between the 1990s and 2010s, with most plot sizes being less than 1 ha. Field-inventory AGB was primarily calculated using the three-parameter moist forest allometric equation [24], incorporating regional height models and stem-level wood density derived from species-level information [22].

Due to the time lag between satellite mapping and field inventories, we excluded inventory plots that had experienced deforestation or large regrowth, as identified by the long-term Tropical Moist Forest (TMF) disturbance dataset [25]. As shown in **Supplementary Fig. 10a, b**, the AGB model incorporating both CH and WD, defined as $AGB = 1.3354 \times (CH \times WD)^{1.8146}$, outperformed the CH-only model, yielding a higher coefficient of determination ($R^2 = 0.56$ vs. 0.47) and a lower mean absolute error (MAE = 66.3 Mg/ha vs. 72.4 Mg/ha). We also evaluated an AGB model developed in our recent study on African dense forests. Although it achieved a slightly lower MAE of 65.8 Mg/ha, it exhibited greater saturation at high AGB values (**Supplementary Fig. 10c, d**), highlighting the advantage of using locally calibrated inventory data to improve model performance.

Furthermore, our AGB map was also compared with some published datasets (**Supplementary Table 1**) against the filed inventory data. The developed AGB model at 30 m resolution, $AGB = 1.3354 \times (CH \times WD)^{1.8146}$, showed the best agreement with field-inventory AGB data (**Supplementary Fig. 11**), achieving $R^2 = 0.52$, MAE = 71.0 Mg/ha, and Bias = 9.5 Mg/ha. Both the EBA and GEDI L4B AGB products also performed reasonably well, with $R^2$ values of 0.46 and 0.49 and MAE values of 88.1 and 88.3 Mg/ha, respectively, though they significantly

underestimated biomass (Bias = 58.9 and 63.4 Mg/ha). Although the GTDX CH product demonstrated high accuracy, the GTDX AGB derived from GEDI AGB did not perform comparably, likely due to underestimations in the GEDI AGB data. Notably, the Baccini AGB map had a small bias (−6.4 Mg/ha), but its model error was relatively high. Other AGB datasets remained limited by low correlation and/or large errors.

The developed AGB map exhibits a spatial pattern similar to the CH map shown in **Supplementary Fig. 3a** and provides finer spatial detail compared to previously published AGB products (**Supplementary Fig. 12**). While the GEDI L4B AGB offers high nominal resolution (~25 m), it lacks spatial variability, resulting in uniformly low values across the region. This also contributes to the low AGB estimates observed in the GTDX map. In contrast, most AGB maps developed for earlier periods, such as Avitabile, GlobBiomass, Baccini, and Saatchi (2000s), do not capture recent disturbances, making them less comparable to our product. Among these, Avitabile, GlobBiomass, and Saatchi (2000s) [26] maps show relatively low biomass values, while the Baccini AGB map reports comparatively higher values. While the new Saatchi AGB map (2020) [27] captures strong spatial gradients, it reports comparatively elevated AGB values in the northeastern Amazon. Notably, although the ESACCI AGB map corresponds to the same reference year as ours and shows large biomass estimates, its coarse resolution limits its ability to represent spatial detail. As a result, the ESACCI AGB map displays only minor spatial variation across dense forest regions.

## Supplementary Text 5: Mann-Kendall test for CH gain and loss

To identify noise of CH gain ($\Delta CH > 0$), we used Mann-Kendall test [28-30] to calculate the trend of $\Delta CH$ as:

$$S = \sum_{k=2019}^{2021} \sum_{j=k+1}^{2022} sign(CH_j - CH_k) \quad (1)$$

$$sign(CH_j - CH_k) = \begin{cases} +1 \; if \; CH_j - CH_k > 0 \; (gain) \\ 0 \; if \; CH_j - CH_k = 0 \; (no \; change) \\ -1 \; if \; CH_j - CH_k < 0 \; (loss) \end{cases} \quad (2)$$

The Mann–Kendall statistic ($S$) is based on the sign of six pairwise canopy height (CH) differences from 2019 to 2022: $\Delta CH_{2020-2019}$, $\Delta CH_{2021-2019}$, $\Delta CH_{2022-2019}$, $\Delta CH_{2021-2020}$, $\Delta CH_{2022-2020}$, and $\Delta CH_{2022-2021}$. For forest growth, CH typically increases continuously over time, so the pairwise differences between $CH_j$ and $CH_k$ are expected to be consistently positive, yielding a Mann-Kendall sum ($S$) of 6. In contrast, for CH loss, it is often unclear in which year degradation or deforestation occurred, and CH reductions may not follow a consistent temporal trajectory. This

makes using the Mann-Kendall sum (*S*) alone less effective for filtering noise in CH loss. Therefore, we additionally used changes in Sentinel-1 VV backscatter to validate CH loss. To avoid discarding genuine changes, for CH gain we retained pixels identified as regrowth in the Tropical Moist Forest (TMF) dataset, while for CH loss we kept pixels supported either by a strong negative Mann–Kendall trend ($S \leq -4$) or by degradation and deforestation detected in the TMF dataset.

**Supplementary Text 6: Annual canopy cover mapping**

The **annual canopy cover maps** for the Amazon forest were produced using a deep learning model similar to the CH model (**Supplementary Text 1**), integrating Sentinel-1, Sentinel-2, and GEDI canopy cover data[31] . Consistent with the CH maps, we generated annual canopy cover maps at 10 m resolution. We evaluated the performance of canopy cover maps using independent GEDI canopy cover data. The results showed good consistency between the estimated canopy cover and GEDI observations from 2019 to 2022, with $R^2$ values of 0.63–0.67 and a close MAE value of ~13% (**Supplementary Fig. 13**). Note that we used this dataset only as a reference for undisturbed forests (cover change ≤ 2%) in order to exclude inconsistent canopy height change trends, and we employed the TMF dataset as an additional reference to further reduce uncertainty. Therefore, the uncertainty in canopy cover data has only a minor impact on the processing of canopy height change.

**Supplementary Text 7: Performance of forest height and biomass across forest types**

To further assess the robustness of the canopy height and biomass maps across heterogeneous Amazonian ecosystems, we performed additional ecosystem-specific evaluations across four major vegetation formations derived from the MapBiomas land-cover classification, including Forest formation, Savanna formation, Mangrove, and Flooded forest classes (**Supplementary Fig. 15**). Using independent airborne lidar (ALS) observations, our canopy height estimates showed relatively consistent performance across ecosystem types, although some biome-dependent differences remained, particularly in structurally complex environments such as mangroves and flooded forests.

Among the evaluated vegetation formations, the highest agreement between predicted and ALS-derived canopy height was observed in Savanna formations ($R^2 = 0.65$; MAE = 2.40 m), likely reflecting their comparatively open canopy structure and lower vertical complexity. Forest

formations also showed relatively strong performance ($R^2$ = 0.47; MAE = 4.34 m), although the regression slope lower than unity indicated an underestimation tendency at high canopy heights. In contrast, Mangrove and Flooded forest systems exhibited lower correlations and larger uncertainties. Mangroves showed moderate agreement ($R^2$ = 0.63; MAE = 4.99 m), but canopy heights were systematically underestimated for taller stands, likely due to dense and vertically heterogeneous canopy structures, species composition, and complex coastal environmental conditions affecting radar and optical signal responses. Flooded forests exhibited the lowest performance ($R^2$ = 0.51; MAE = 4.05 m), with clear compression of high canopy values and larger bias, potentially associated with seasonal inundation, mixed water–vegetation spectral signals, and variable canopy structures that complicate remote sensing retrievals.

For biomass, because independent field inventory datasets covering all ecosystem types were not consistently available across the Amazon, we evaluated ecosystem-specific biomass relationships through comparison with the ESA CCI Biomass product as an intercomparison benchmark (**Supplementary Fig. 16**). We found that biomass relationships varied substantially across ecosystem types. Forest formations generally showed the strongest consistency with the ESA CCI product, whereas flooded forests and mangroves exhibited larger deviations and increased scatter. These differences likely reflect both the intrinsic ecological heterogeneity of these ecosystems and the higher uncertainties associated with biomass retrieval in structurally complex or hydrologically dynamic environments. In flooded forests, for example, inundation dynamics can alter radar backscatter and canopy reflectance properties, while in mangrove systems strong salinity gradients, mixed vegetation assemblages, and saturated high-biomass conditions may further increase retrieval uncertainty.

Overall, these ecosystem-specific evaluations demonstrate that the canopy height and biomass products maintain broadly consistent performance across major Amazonian vegetation formations, while also highlighting the importance of interpreting biomass and structural estimates within their ecological context. The observed variability among ecosystem types further suggests that uncertainties in large-scale biomass products are not spatially uniform and may be amplified in ecosystems with complex canopy architecture or strong hydrological influences.

## Supplementary Text 8: High-resolution forest height change estimates

We used a deep learning approach (U-Net model) to predict annual tree height maps at 10 m resolution, using carefully pre-processed Sentinel-1/-2 images trained on GEDI top-of-canopy-height data (**Supplementary Fig. 1**). We then derived annual AGC maps at 30 m resolution by applying an allometric model based on height and wood density (**Methods, Supplementary Text 1–4**). The new tree height maps performed well when evaluated against GEDI data unseen for training the U-Net model ($R^2$ = 0.78, MAE = 3.83 m) and independent airborne lidar data covering in total ~1400 flights over areas of 5270 $km^2$ ($R^2$ = 0.56, MAE = 4.37 m) (**Supplementary Fig. 2, 4, 6, 14**). Compared to existing single-year products evaluated on the maximum height data from the same ALS dataset (MAE = 4.59–10.29 m), our annual maps have a lower error by 5 to 58% and provide consistent estimates across multiple years (**Supplementary Fig. 3–9)**. The maps also showed good agreement AGC ($R^2$ = 0.56, MAE = 30.22 Mg C $ha^{-1}$) with field inventory data from 109 independent forest plots [20-23] (**Supplementary Fig. 10–12, 14**).

We mapped tree height changes annually from 2019 to 2022 (**Fig. 1**) (**Methods**). Validation was performed against changes from clusters of GEDI footprints aggregated over small regions, because a single footprint has no revisit of the same location. Our analysis revealed consistency between predicted continuous maps of height changes and GEDI clusters of footprints, capturing spatial patterns of gains and losses that aligned well with changes derived from aggregated GEDI observations (**Supplementary Fig. 22**), even though noise levels were high ($R^2$ = 0.24, MAE = 4.90 m at 1 km; **Supplementary Fig. 17**). Agreement declined at smaller aggregation scales although estimation errors remained comparable (**Supplementary Figs. 23, 24**).

The accuracy of our detection of height losses is also supported by independent evidence from tree cover loss, fire, and logging events (**Supplementary Fig. 18**) in the Brazilian state of Mato Grosso mapped using high-resolution Planet NICFI imagery and U-Net model (~5 m) [32,33]. Detection rates showed that height loss more consistently captured Planet-derived tree cover loss (43%–86%) than tree cover loss captured height loss (20%–100%), particularly at fine scales (**Supplementary Fig.**

**19, 20**). Our height-loss mapping showed substantially better agreement with 5-m Planet-derived tree cover loss than the Tropical Moist Forest (TMF) [25], Landsat-derived Global Forest Change (GFC) tree cover loss dataset [34], and the Sentinel-1 radar-based RAdar for Detecting Deforestation (RADD) product[5], particularly at fine spatial scales (such as 30 m), where those datasets captured less than 20% of the Planet-derived tree cover loss. Height loss also detected fire (33%–99%) and logging (22%–88%) events. As logging maps delineate broader harvesting zones, and many canopy gaps are occluded, replaced, or rapidly recover[44,46], not all logged pixels exhibit measurable height loss.

## Supplementary Text 9: CH change classification

To categorize canopy height (CH) changes into disturbance types consistent with the TMF framework, we adopted a multi-step classification strategy that assigns ΔCH values to four categories: deforestation, degradation, regrowth, and other forests. This approach complements the TMF Annual Change product by capturing smaller-scale disturbances not detected by TMF, while maintaining consistency for overlapping events.

(1) **Other forests:**

Pixels labeled as undisturbed forest in the TMF product were classified as other forests if their absolute CH change (|ΔCH|) was <= 5 m. This threshold follows definitions in prior studies[35] and accounts for minor fluctuations not considered indicative of disturbance. These pixels comprised 30.1% of all detected change. TMF undisturbed pixels exhibiting larger CH changes were further reassigned to disturbance types based on subsequent criteria.

(2) Deforestation and degradation (ΔCH < 0):

Because satellite CH estimates at 10–30 m resolution tend to overestimate short vegetation, complete canopy loss is not always reflected as near-zero CH values. By analyzing CH loss in TMF-labeled deforested areas, we observed ΔCH values ranging from –30 to 0 m, typically clustering between –5 and 0 m, and residual canopy heights in 2022 between 5 and 45 m (see **Supplementary Fig. 27**). Based on this, we defined deforested pixels as those with ΔCH < –5 m and final CH < 10 m, aligning with canopy gap detection criteria used in airborne LiDAR

analyses[35]. Disturbed pixels not meeting these thresholds (and not categorized as other forests) were classified as degraded.

(3) Regrowth and degradation (ΔCH > 0):

To assign disturbance types to positive CH change pixels, we used TMF's classification of regrowth, degradation, and an "uncertain" class (12.7% of disturbed pixels). For the uncertain group, we trained an XGBoost classifier[36] using labeled TMF samples of regrowth and degraded forests (**Supplementary Table 14**). Input features included CH values from 2019 to 2023, multiple ΔCH combinations (e.g., 2023–2019, 2022–2019), and canopy cover change (ΔCC). This classification step allowed us to assign a disturbance type to pixels not explicitly labeled by TMF.

To assess the impact of the filtering process, we summarized the change in CH-loss pixels after each step (**Supplementary Table 13**). The results show that the filtering primarily excluded pixels with CH change < 10 m (14.1%–77.3%), while only 0%–4.2% of pixels were removed when CH loss exceeded 20 m.

## Supplementary Text 10: Comparison with atmospheric inversion and other carbon flux estimates

Comparisons with top-down atmospheric inversion models[37-39], bottom-up flux estimates and hybrid approaches[40] confirm considerable differences across methods (**Supplementary Table 11)**. If we approximate belowground biomass losses using a median belowground-to-aboveground carbon ratio of ~23% across the Amazon[41], the total biomass carbon loss (~316 Tg C $yr^{-1}$) becomes broadly comparable in magnitude to recent inversion-based estimates of Amazonian carbon emissions (−290 ± 400 during 2010–2018[38]; −440 ± 100 Tg C $yr^{-1}$ in 2019[39]). However, these numbers are not directly comparable. Top-down atmospheric inversion models estimate net ecosystem carbon exchange, integrating $CO_2$ fluxes from multiple sources including soil respiration, inland waters, litter decomposition, fires, and legacy effects, whereas our estimates are restricted to structural aboveground biomass changes. Nonetheless, our approach offers improved spatial attribution of small-scale degradation, afforestation, plantations, and post-disturbance regrowth. As

such, our estimates offer a complementary but not equivalent perspective on the Amazon carbon balance.

**Supplementary Text 11: Patch-size and disturbance-type effects on biomass density change**

Deforestation and degradation always cause a substantial biomass carbon (AGC) density decline (**Supplementary Fig. 33a**). Deforestation events cause AGC density losses of 8–29 Mg C $ha^{-1}$ $yr^{-1}$ (67–91% of the initial AGC) increasing with patch size and reaching 13–35 Mg C $ha^{-1}$ $yr^{-1}$ in the largest events (**Supplementary Fig. 34**), consistent with ref. [42]. Degradation events cause smaller AGC density losses going from 0.1 to 11 Mg C $ha^{-1}$ $yr^{-1}$ (1 to 42% of the initial AGC). Regrowth events classified as such in TMF show an increase of AGC density with time (mean = 3.5 Mg C $ha^{-1}$ $yr^{-1}$) with recovery being more pronounced in patches larger than 100 ha (**Supplementary Fig. 33c**) which correspond to planned afforestation (**Supplementary Fig. 35**).

The temporal trajectories of AGC density change following previous degradation and regrowth activity also varies with patch sizes (**Supplementary Fig. 33b**, **d**). Degradation is followed by a reduction of AGC density losses, especially in large patches, whereas smaller patches showed more modest reductions. On the other hand, regrowth led to very gradual gains of AGC density[43]. Typically, we found that regrowth of forests recovering after past degradation events takes 20 to 30 years or more (**Supplementary Fig. 36**), consistent with prior findings [43]. Similar but weaker and temporally more stable AGC density change rates were observed in protected areas compared to non-protected ones (**Supplementary Fig. 37**), reflecting the influence of governance on carbon density dynamics [44,45].

The AGC density change per unit disturbed area found in this study shows good agreement with previous findings [46-48] (**Supplementary Table 12**), with comparable values representative of regional-scale forest dynamics, despite differences in spatial coverage, sampling density, and methodology. The average AGC density loss rate for disturbed forests (−19 Mg C $ha^{-1}$) was close

to that derived from sparse GEDI observations (−23 Mg C $ha^{-1}$) [46], with some discrepancies possibly due to uneven spatial coverage by GEDI. The AGC density growth rate of regrowing forests (3.5 Mg C $ha^{-1}$ $yr^{-1}$) was consistent with LiDAR-based estimates (3.8 Mg C $ha^{-1}$ $yr^{-1}$) [47] and field inventory data (3.4–4.6 Mg C $ha^{-1}$ $yr^{-1}$) [48], and exceeded the IPCC default growth rates for tropical rainforests (2.8 Mg C $ha^{-1}$ $yr^{-1}$) [48,49]. Our estimates were close to the highest modelled regrowth rate (3.2 ± 0.6 Mg C $ha^{-1}$ $yr^{-1}$) derived from ESA-CCI biomass[50]. The lower average rates reported in the latter study may reflect the inclusion of older regrowth forests (over 30 yrs.) and methodological differences[51], though overlaps between data approaches increase our confidence in the results. Within protected areas, our growth rate of 3.1 Mg C $ha^{-1}$ $yr^{-1}$ from regrowing forests is more consistent with the IPCC default value but significantly lower than in non-protected areas where our growth rate is 3.6 Mg C $ha^{-1}$ $yr^{-1}$ (**Supplementary Fig. 38**). This difference may reflect the greater presence of young regrowth forests in non-protected areas, where early-stage biomass accumulation is typically faster. In contrast, the more complex and varied disturbance drivers in protected areas may result in slower or less consistent regrowth.

Across all disturbance types, increasing disturbance density was consistently associated with more negative AGC density change (**Supplementary Fig. 39**). Both degradation and deforestation densities showed significant negative relationships with total and mean AGC change, indicating that areas with higher concentrations of forest disturbances experienced disproportionately greater carbon losses. The relationship was particularly strong for disturbance density integrated across all disturbance types, which exhibited the steepest decline in AGC density change. Mean AGC change showed a stronger sensitivity to disturbance density than total AGC change, suggesting that increasing disturbance aggregation not only expands the affected area but also intensifies per-area carbon loss. Notably, AGC density declined rapidly at low-to-moderate disturbance densities and then gradually stabilized at higher densities, implying a nonlinear response where relatively small increases in disturbance concentration can trigger substantial reductions in forest carbon stocks. These results highlight the critical role of disturbance clustering and spatial concentration in shaping regional carbon dynamics across Amazon forests.

## Supplementary Text 12: Multiple degradation pathways and their carbon signatures

Forest degradation in the Amazon is driven by multiple interacting climatic and anthropogenic processes rather than a single mechanism, including drought, fire, selective logging, road expansion, fragmentation, edge effects, land-use transitions, and differences in forest recovery stage. To better characterize this complexity, we examined the relationships between AGC change and several disturbance-related factors, including burned-area fraction, logging area, edge area, distance to roads, forest age, land-use transition type, and disturbance density.

**Road proximity** showed a clear negative association with degradation-related AGC loss (**Fig. 4c**). Both total AGC loss and mean AGC density loss were strongest near roads and declined rapidly with increasing distance from the nearest road, indicating that road accessibility is an important spatial predictor of forest carbon loss. The estimated road influence distance extended approximately 2.5–3.5 km from the nearest road, slightly larger than the ~2 km effect reported using GEDI data[52]. Sensitivity tests further showed that the estimated influence distance shortened under lower road-fraction thresholds and lengthened under higher thresholds, suggesting that fragmented road margins and major road corridors generate different spatial footprints of carbon loss (**Supplementary Fig. 41**).

**Fire, logging, and edge-related degradation showed distinct but complementary carbon signatures (Supplementary Fig. 42)**. Although total AGC losses were often concentrated in areas with relatively low burned-area fractions, small edge areas, and limited logging area, mean AGC density loss generally increased with disturbance intensity. In particular, grid cells with burned-area fractions exceeding ~50% were associated with substantially stronger declines in mean AGC density, suggesting that severe or repeated fire disturbances can markedly intensify per-area carbon loss. Similarly, extensive edge influence and large-scale logging were associated with stronger mean AGC density declines, highlighting the importance of fragmentation and selective extraction as degradation pathways that may not always appear as complete canopy removal.

**Forest age** further modulated the vulnerability of forests to AGC decline (**Fig. 4d)**. Carbon losses were dominated by old-growth forests (>200 years), reflecting both their large carbon stocks and

high exposure to degradation processes. However, young forests (0–20 years) and forests of uncertain age also contributed to total AGC losses, suggesting that both mature forest degradation and disturbance of recovering secondary forests shape the regional carbon budget. These age-dependent patterns indicate that forest carbon loss cannot be interpreted solely as a function of disturbance area, but also depends on pre-disturbance carbon density and recovery stage.

**Disturbance density** (defined as the proportion of 30-m pixels classified as the corresponding disturbance type within each 5-km grid cell) provided an additional indicator of the spatial concentration of degradation processes (**Supplementary Fig. 39**). Areas with higher degradation, deforestation, or combined disturbance density showed more negative AGC density change, indicating that clustered disturbances are associated with stronger carbon losses. This pattern suggests that the spatial aggregation of disturbance events can amplify carbon impacts through cumulative degradation, repeated disturbance, and reduced recovery potential.

Together, these results show that Amazon forest carbon loss reflects the combined influence of multiple interacting degradation pathways rather than a single dominant driver. Roads, fire, logging, fragmentation, forest age, and disturbance clustering each capture different dimensions of degradation pressure and forest vulnerability. However, these drivers often overlap in space and time and depend on climate e.g. during droughts, fires and edge degradation are more severe, making exact causal attribution difficult using currently available large-scale datasets. Therefore, our driver analysis should be interpreted as identifying dominant disturbance associations and carbon signatures, rather than assigning each pixel to a single causal mechanism.

## Supplementary Text 13: Uncertainties and limitations in biomass carbon change estimates

Despite the good spatial agreement with independent datasets and the additional PlanetScope-based validation, several limitations and uncertainties remain in the derived canopy height and AGC change products. First, canopy height change was estimated from annual Sentinel-based canopy height maps, and uncertainty may therefore propagate and accumulate through year-to-year

differencing. Although multiple spatial and temporal consistency constraints were applied to reduce isolated noise and unstable retrievals, some commission errors and residual artefacts are likely unavoidable, particularly for subtle canopy disturbances involving low-magnitude height loss (<5 m) or very small disturbance patches (<2 ha). These subtle disturbances are inherently difficult to detect because their structural signals are often close to the uncertainty range of remote sensing retrievals and may only weakly modify optical or radar reflectance properties.

The independent validation itself also has important limitations. Visual interpretation using high-resolution optical imagery, including PlanetScope observations, may underestimate the occurrence of subtle structural canopy changes, especially in humid tropical forests characterized by dense canopy cover, rapid vegetation recovery, shadow effects, and strong spectral heterogeneity. In many cases, low-intensity degradation, understory disturbance, selective branch removal, or partial canopy opening may generate measurable canopy height reductions without producing clear spectral signatures detectable from optical imagery alone. Consequently, the true uncertainty associated with subtle canopy disturbances likely lies between the omission and commission rates estimated from optical interpretation. This challenge is particularly important for small height-loss events, which represent a substantial fraction of the mapped carbon loss but remain difficult to independently verify using currently available large-scale reference datasets.

Although our height and AGC change estimates provide substantially finer spatial detail than previous large-scale products, direct comparisons remain limited by differences in spatial resolution, temporal coverage, disturbance sensitivity, and biomass model assumptions. Evaluation against independent airborne and spaceborne datasets (ALS and GEDI) indicates a small negative bias in detected canopy height change, suggesting that our carbon-loss estimates are likely conservative. Additional uncertainty arises from canopy height saturation in tall forests and the potential underrepresentation of understory biomass[53], which may lead to underestimated carbon stocks in structurally mature forests where canopy height saturates while stem diameter and biomass continue to increase[54]. Field inventory comparisons (**Supplementary Fig. 38**) [55] further support this

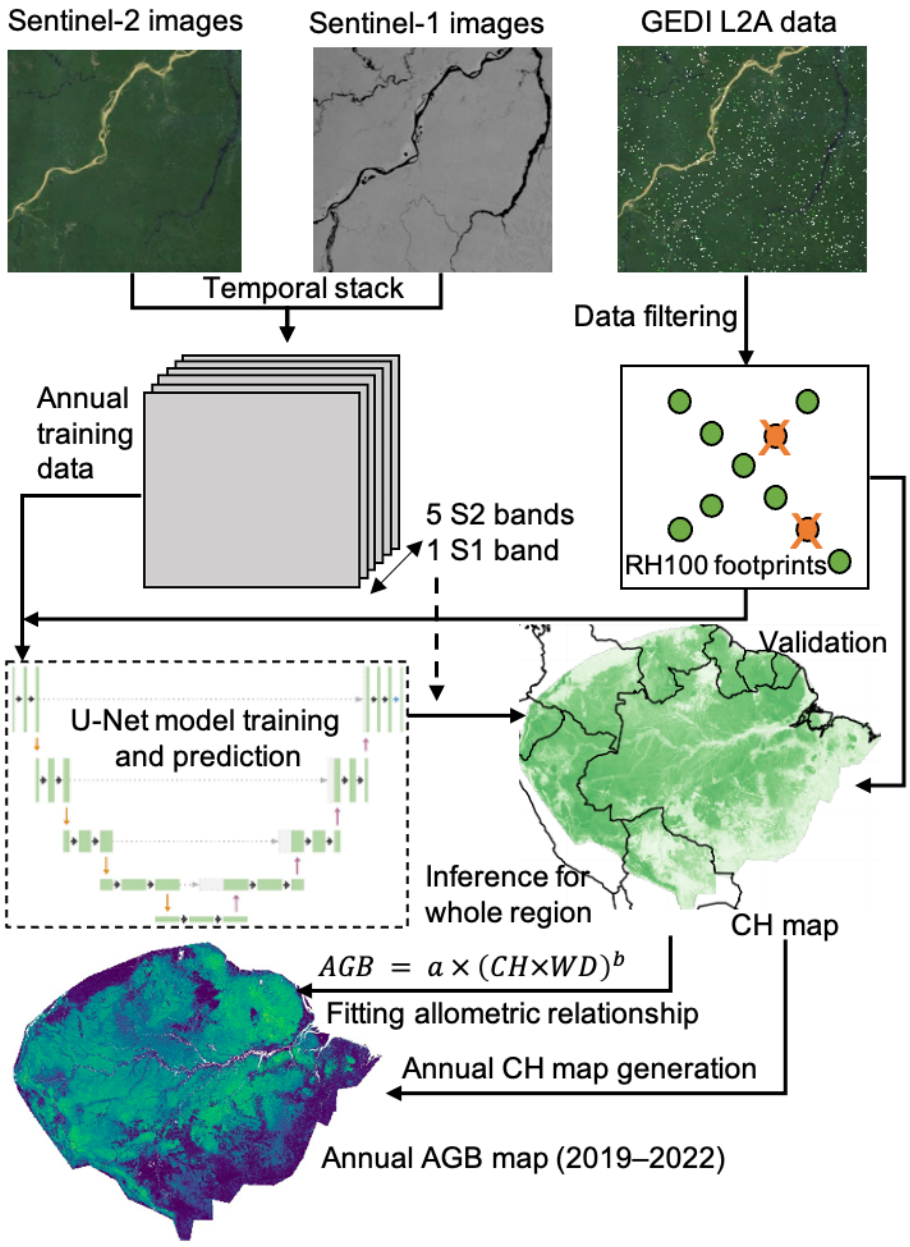
interpretation. Moreover, biomass-gain estimates were derived from a relatively short observation period (2019–2022), limiting the detection of subtle growth in mature forests. Consequently, biomass gains in old-growth forests may be underestimated, whereas the detected gains likely primarily reflect recovery dynamics in younger secondary forests rather than long-term steady-state carbon accumulation.

In addition, the Amazon Basin experiences highly heterogeneous environmental and ecological/diversity conditions, including dense forests, flooded forests, mangroves, transitional ecotonal systems, and savanna formations, all of which may respond differently to climate variability and disturbance processes. Although evaluations against a large sample of airborne LiDAR datasets indicated generally consistent model performance across the major forest types considered in this study, uncertainties remained larger in structurally complex ecosystems such as flooded forests and mangroves. Hydrological variability, seasonal inundation, mixed vegetation–water spectral signals, and heterogeneous canopy architectures contribute to reduced retrieval performance in these environments. Furthermore, our framework integrates both optical and Sentinel-1 SAR observations, allowing the model to exploit complementary spectral, structural, and spatial contextual information. While this design may improve its ability to generalize across contrasting vegetation physiognomies, environmental heterogeneity remains an important source of uncertainty that should be considered when interpreting biomass estimates.

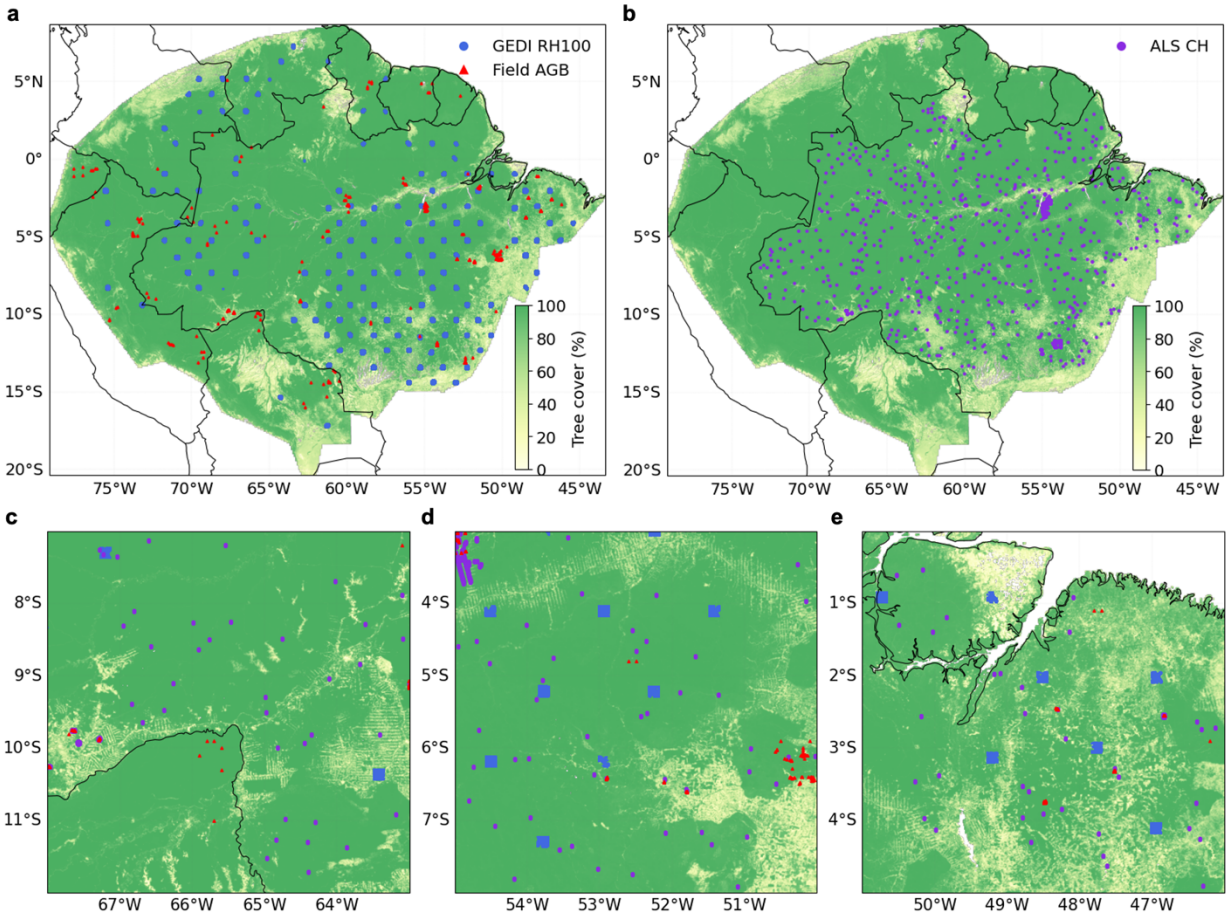
Several additional limitations also affect the interpretation of AGC change drivers and disturbance attribution. The disturbance driver framework combines multiple datasets with different spatial resolutions, temporal definitions, and disturbance classification schemes, including 1-km driver attribution products[56] and 30-m disturbance observations[25]. As a result, individual grid cells may contain multiple interacting degradation processes, including selective logging, fire, fragmentation, agricultural expansion, and subsequent recovery dynamics, which cannot always be disentangled robustly at regional scale. Therefore, the identified drivers should be interpreted as dominant disturbance associations rather than exact pixel-level causal attribution.

Finally, the relatively short study period (2019–2022) limits assessment of longer-term disturbance trajectories and interannual variability in Amazon carbon dynamics. Persistent cloud cover and reduced Sentinel-1 coverage after 2022 constrained the generation of spatially consistent canopy height products across the basin. Together, these limitations highlight the need for improved biomass models that incorporate both horizontal and vertical forest structure[57], longer temporal baselines, denser multi-sensor observations, and broader ground calibration datasets. More accurate attribution of interacting degradation pathways will likely require higher-frequency observations, improved disturbance chronologies, and integration of socioeconomic, infrastructure, and field-based disturbance information. Future foundation models trained across diverse tropical forest conditions, together with upcoming missions such as ESA BIOMASS[58] and NASA NISAR, as well as emerging high-resolution datasets including Planet-based CTrees height products[16], are expected to substantially improve long-term monitoring of subtle forest degradation and tropical forest carbon dynamics.

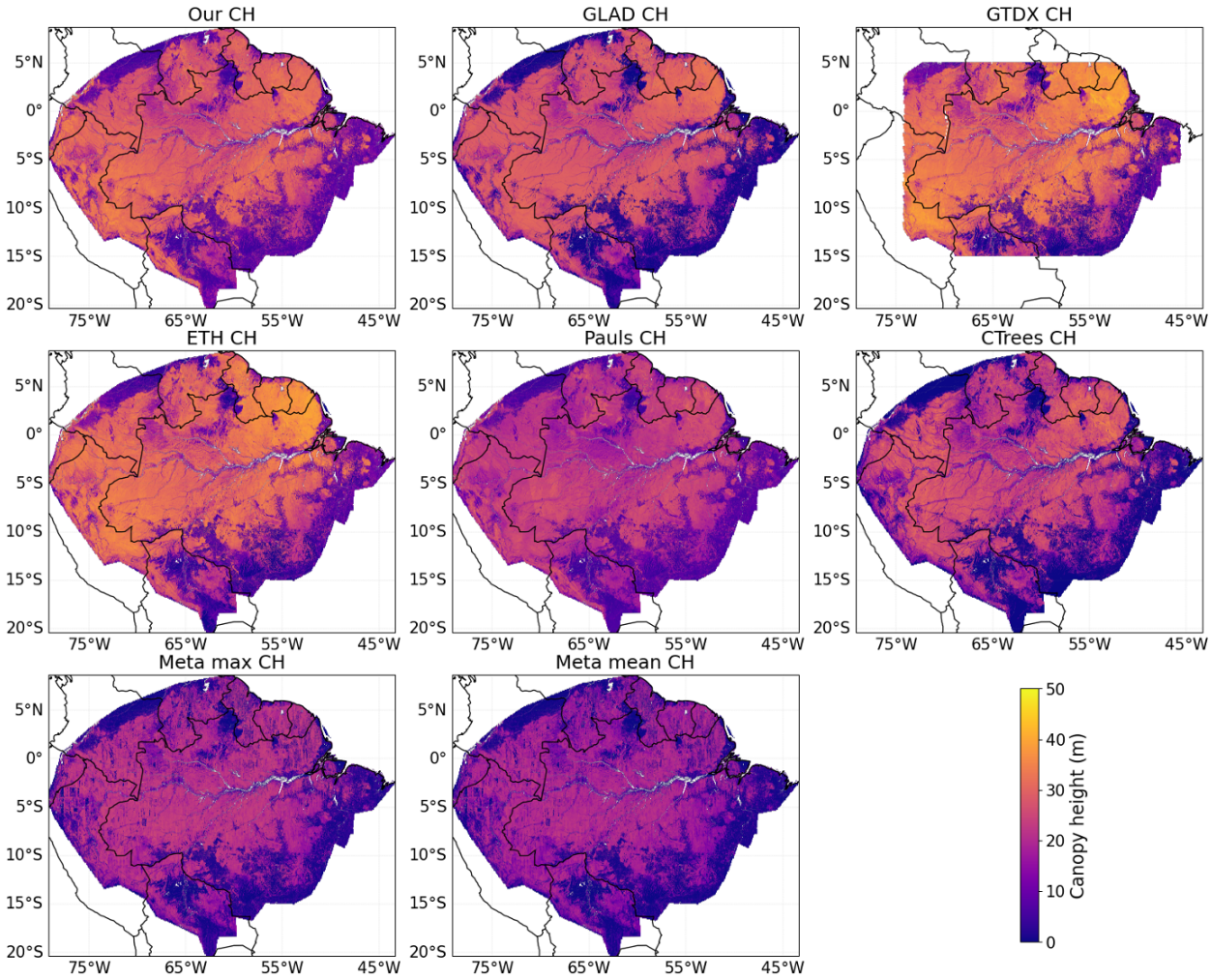
**Supplementary Fig. 1– Fig. 45**



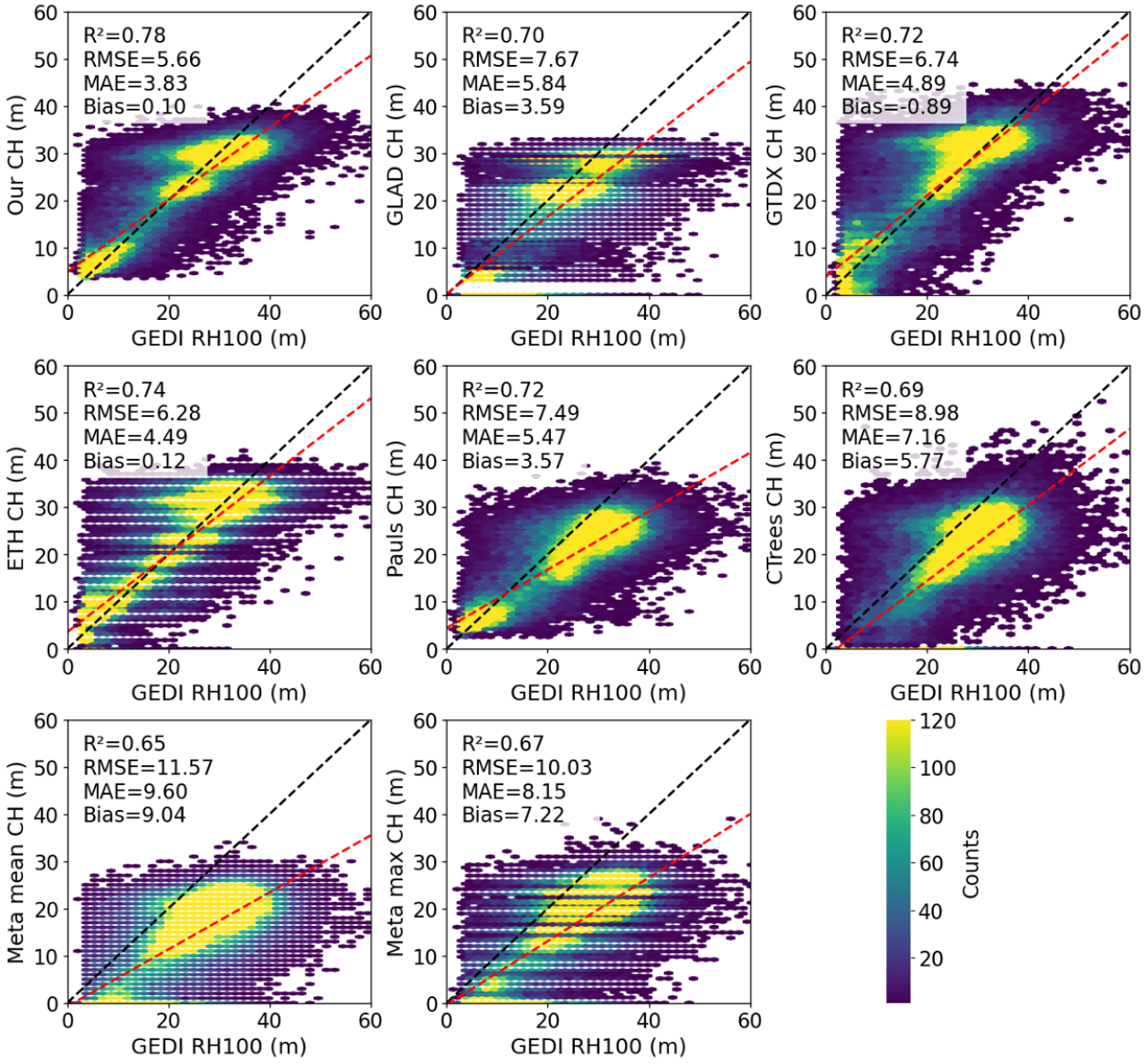

**Supplementary Fig. 1: Framework for generating annual canopy height (CH) and aboveground biomass (AGB) maps across the Amazon forest.** The workflow includes: (1) preprocessing of Sentinel-1, Sentinel-2, and GEDI RH100 data; (2) construction of the training dataset; (3) CH model training and prediction using a U-Net architecture; and (4) derivation of annual AGB maps using an allometric model based on wood density (WD) and the predicted annual CH maps.



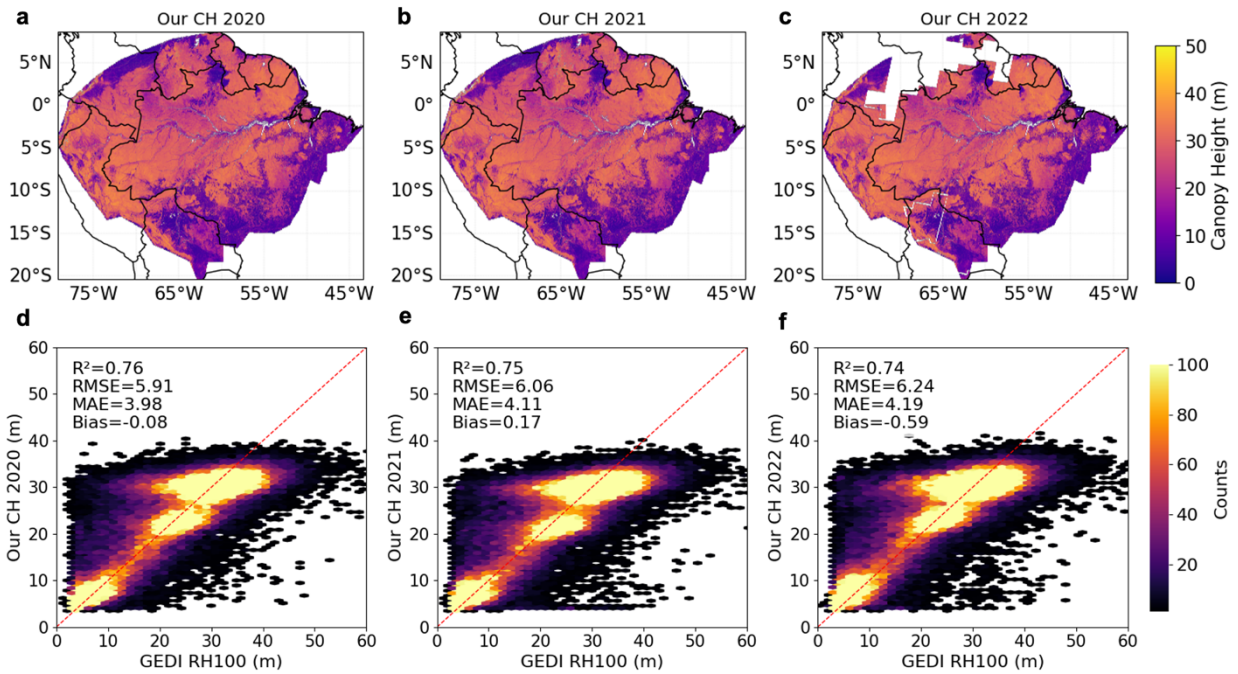

**Supplementary Fig. 2: Spatial distribution of height and biomass validation samples derived from GEDI, airborne LiDAR (ALS), and field inventory data. a,** Spatial distribution of top height (RH100) from GEDI footprints [59] and aboveground biomass (AGB) data derived from field inventories [20,21]. Clusters of closely spaced GEDI footprints are shown as groups. **b,** Spatial distribution of maximum canopy height from ALS data [13]. **c–e,** Three zoomed-in regions illustrating the detailed distribution of validation samples. Tree cover is based on the Global Forest Change (GFC) dataset [34] in 2019, resampled to 1 km resolution.



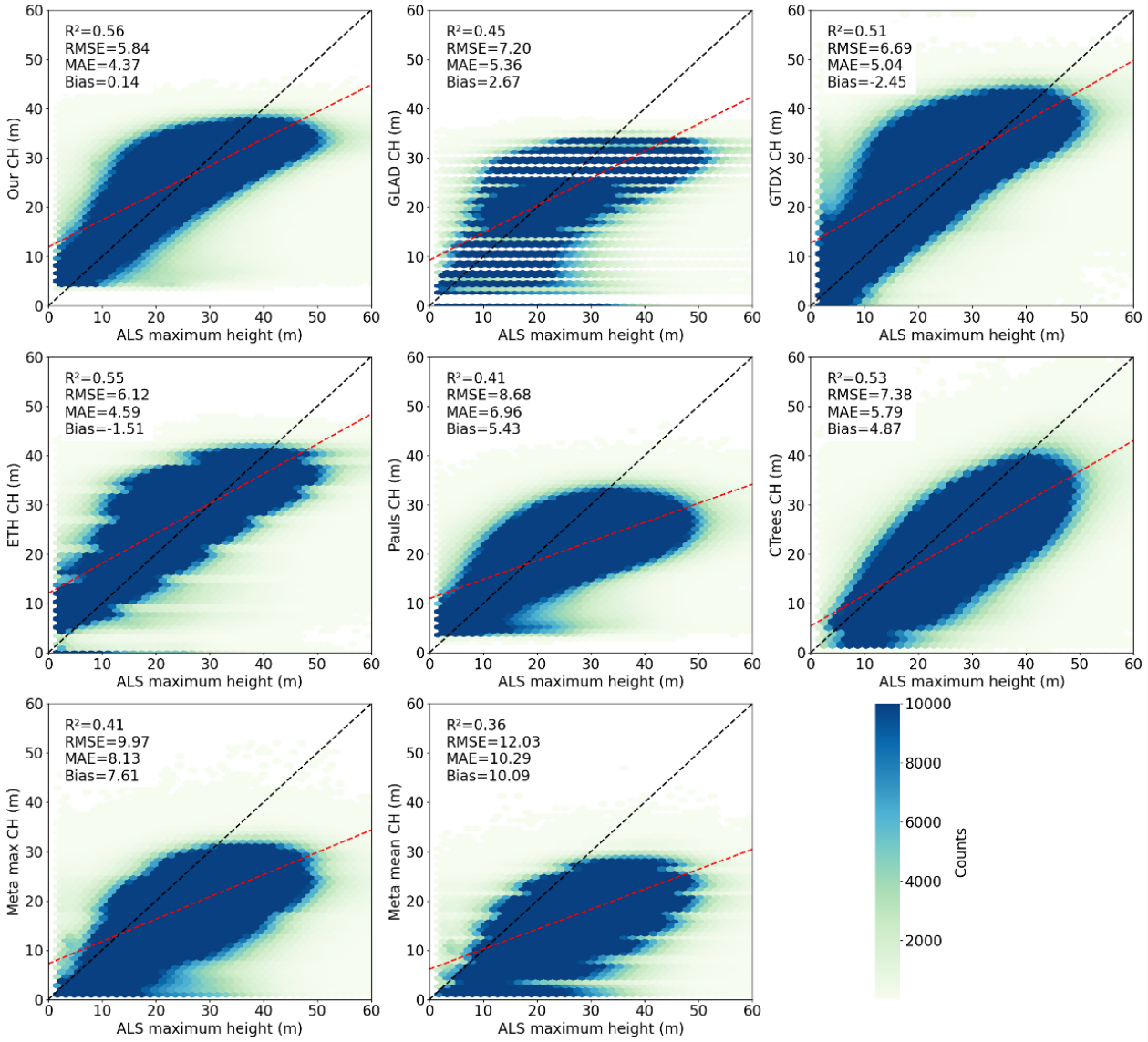

**Supplementary Fig. 3: Comparison of satellite-derived canopy height (CH) maps with independent GEDI RH100 data across the Amazon.** Model performance of our 2019 CH map is compared with several published CH datasets, including GLAD, GTDX, ETH, Pauls, CTrees, and Meta (both maximum and mean CH), using independent GEDI top-of-canopy height (RH100) data for validation. Details on spatial resolution and mapping year for each dataset are provided in **Supplementary Table 1**. The GTDX CH map had limited spatial coverage and did not span the full extent of the study area. The CTrees height map, trained using ALS median height data for the 2016–2018 period, represents the mean between 2020 and 2024 period. For the Meta CH product, we derived both maximum (Meta max) and mean (Meta mean) canopy height at 10 m resolution by aggregating the original 1 m height data.



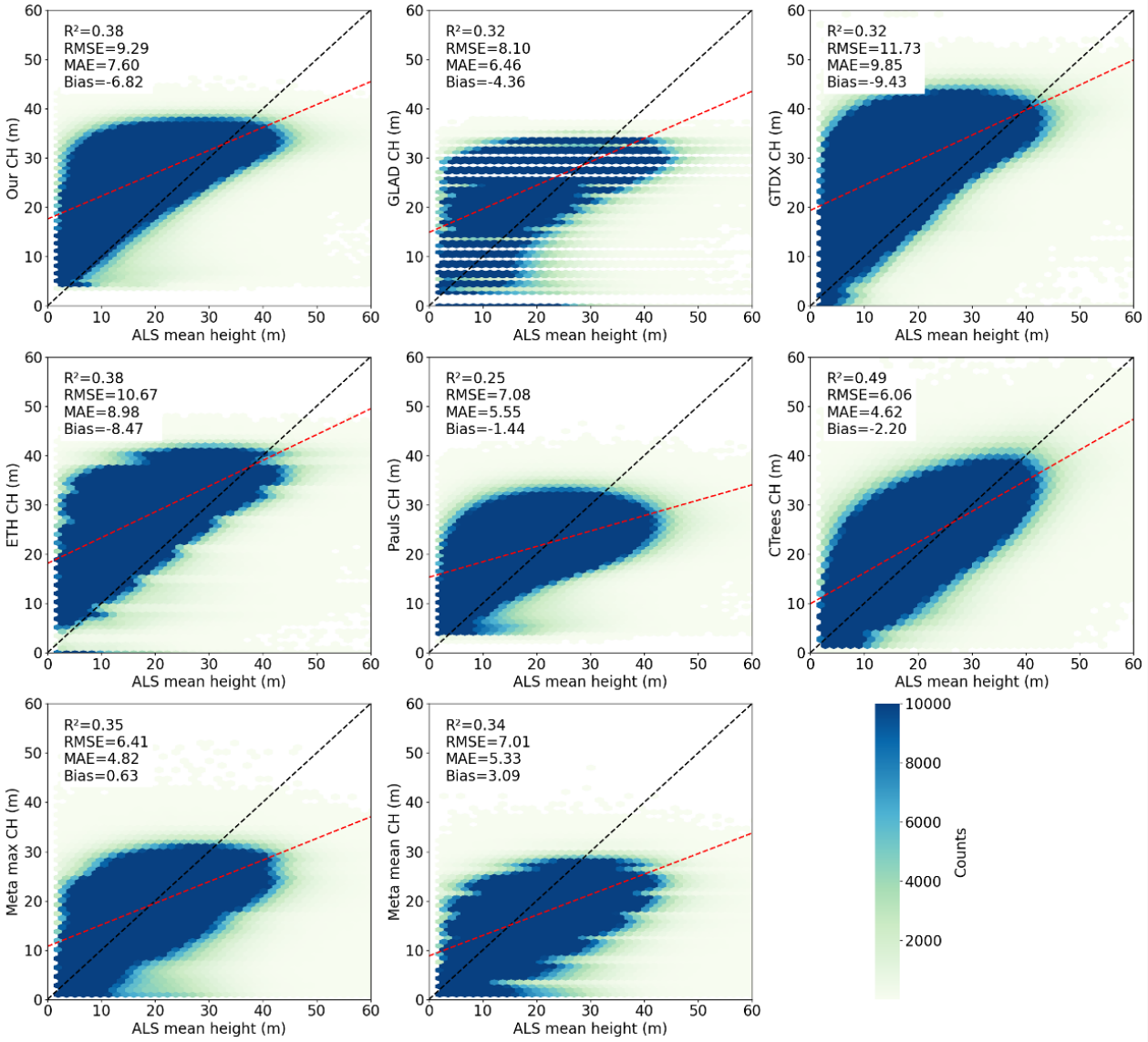

**Supplementary Fig. 4:** Comparison of satellite-derived CH maps with independent GEDI RH100 data **across the Amazon forest.** Model performance of our CH map in 2019 with published datasets, including GLAD, GTDX, ETH, Pauls, CTrees, and Meta max and mean CH, against GEDI top-of-canopy height data. Details on resolution and mapping year are provided in **Supplementary Table 1**. The GTDX CH map had limited spatial coverage and did not cover the entire region. For the Meta CH product, we derived both maximum (**Meta max**) and mean (**Meta mean**) CH at 10-m resolution by aggregating the original 1-m height data.



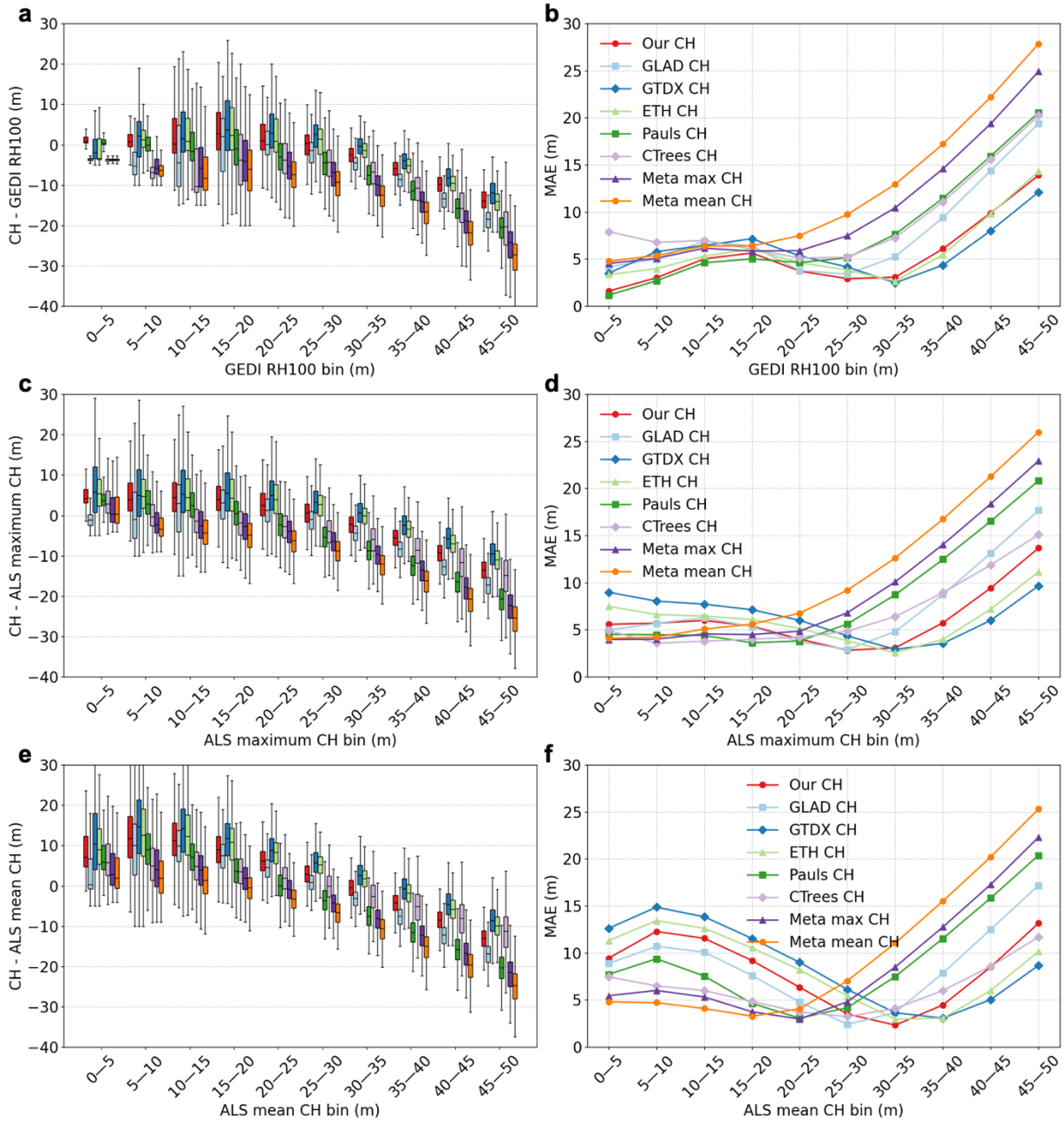

**Supplementary Fig. 5**. Annual canopy height (CH) maps and their validation against independent GEDI RH100 measurements. Panels (a–c) show the spatial distribution of CH across the Amazon dense forests in 2020, 2021, and 2022, respectively. The missing region in the 2022 CH map (c) resulted from data gaps in Sentinel-1 observations, which limited coverage in that area. Panels (d–f) present the validation results of the annual CH maps using independent GEDI RH100 footprints, not used for model training.




**Supplementary Fig. 6: Comparison of our canopy height (CH) map with published CH datasets using independent airborne LiDAR (ALS) data across the Amazon.** Details on resolution and mapping year are provided in **Supplementary Table 1**. The spatial distribution of the ALS data is shown in **Supplementary Fig. 2**. The maximum height from the ALS data was used as the reference.

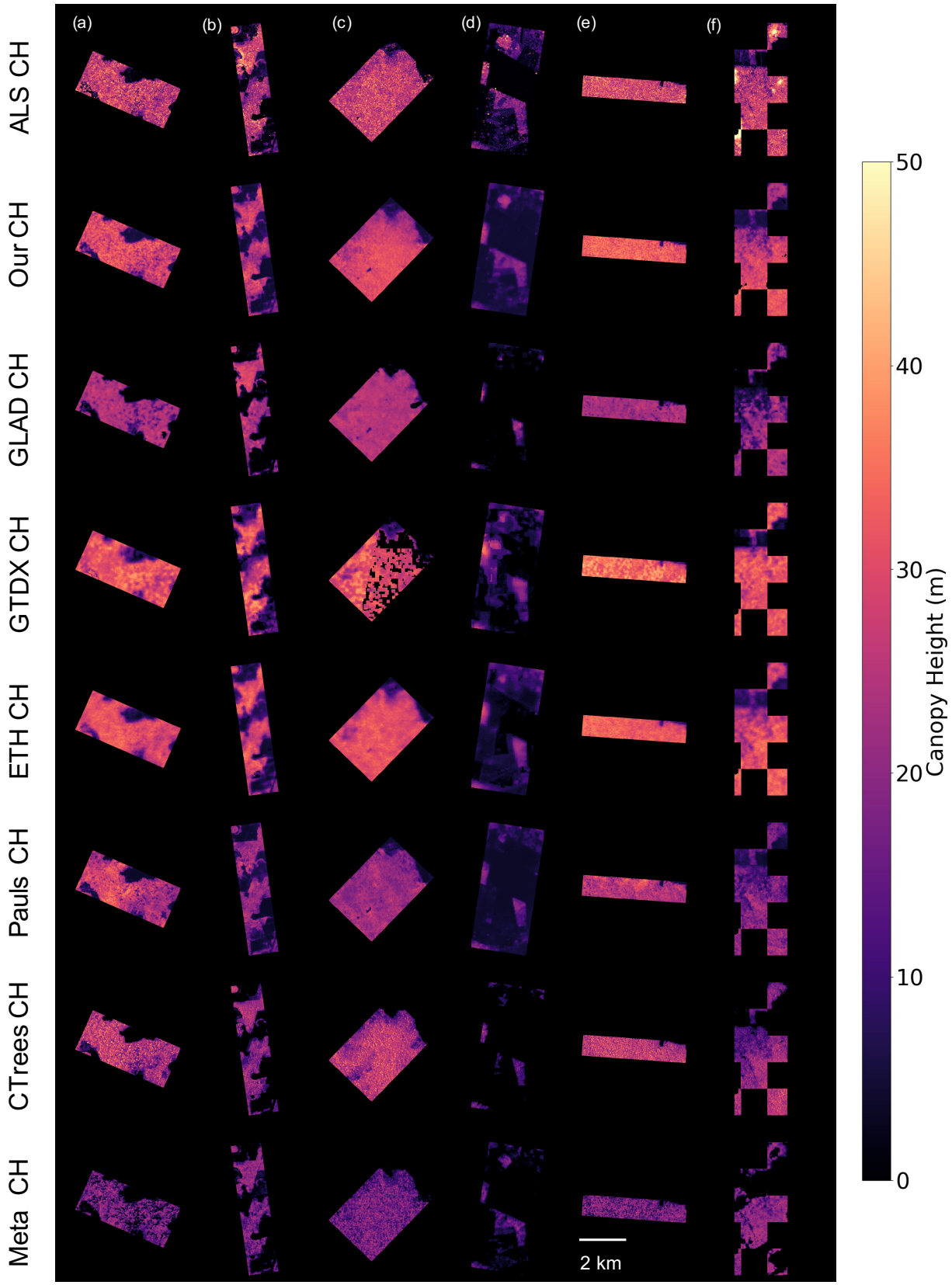



**Supplementary Fig. 7: Comparison of our canopy height (CH) map with published CH datasets using independent airborne LiDAR (ALS) data across the Amazon.** Details on resolution and mapping year are provided in **Supplementary Table 1**. The spatial distribution of the ALS data is shown in **Supplementary Fig. 2**. The mean height from the ALS data was used as the reference.



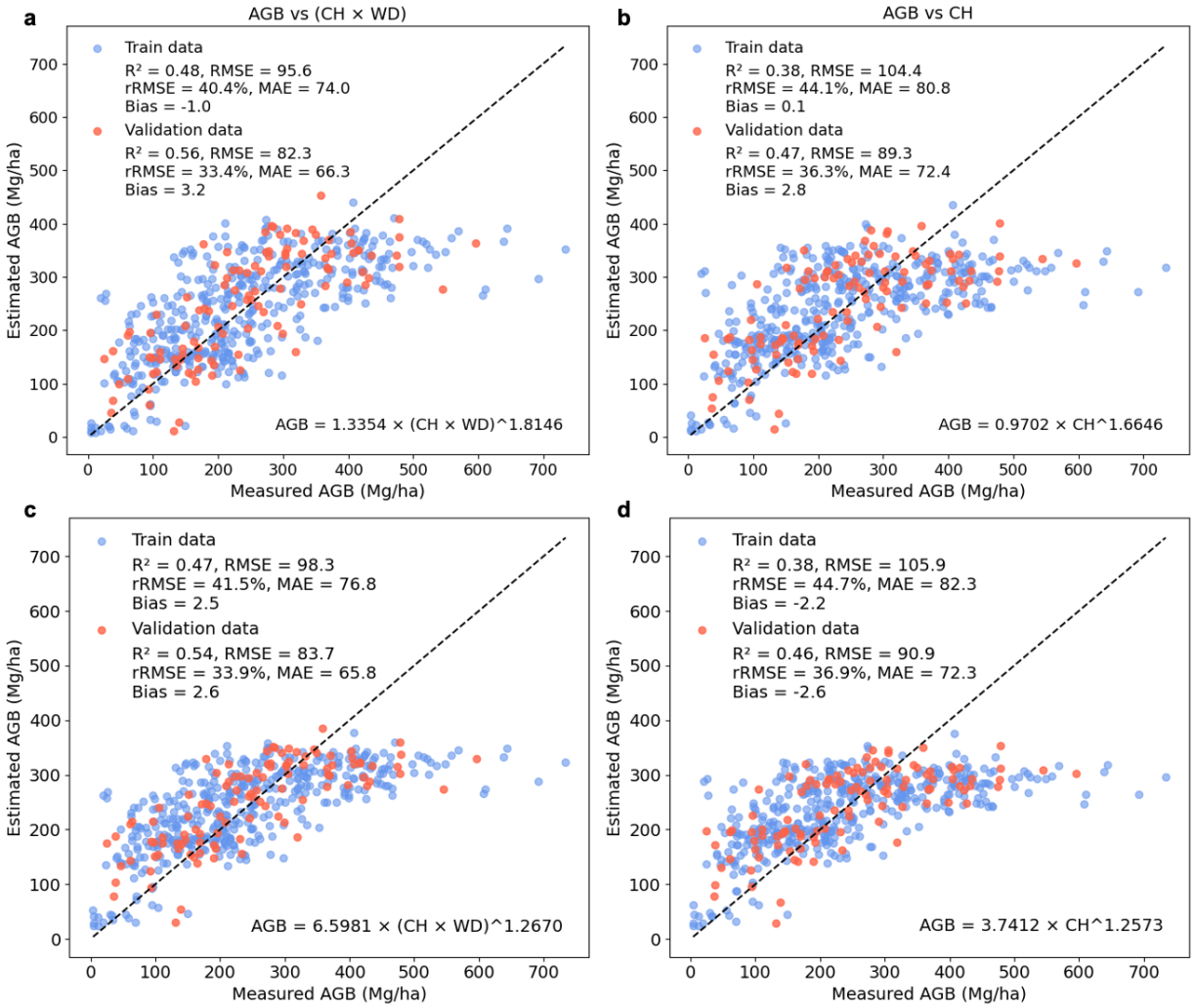

615

616 **Supplementary Fig. 8: Comparison of our canopy height (CH) map and six published CH**
617 **datasets against validation data across different ranges**. **a, b,** Distribution of differences
618 between satellite-derived CH and GEDI RH100 (**a**) and airborne LiDAR (ALS) maximum height
619 (**b**). The validation was made across different height ranges (0–50 m, in 5 m intervals). **c, d,**
620 Variations in CH estimation errors (mean absolute error, MAE) across height bins compared to
621 GEDI RH100 (**c**) and ALS maximum height (**d**). The satellite-derived CH includes seven datasets:
622 our CH and the six published products listed in **Supplementary Table 1**.

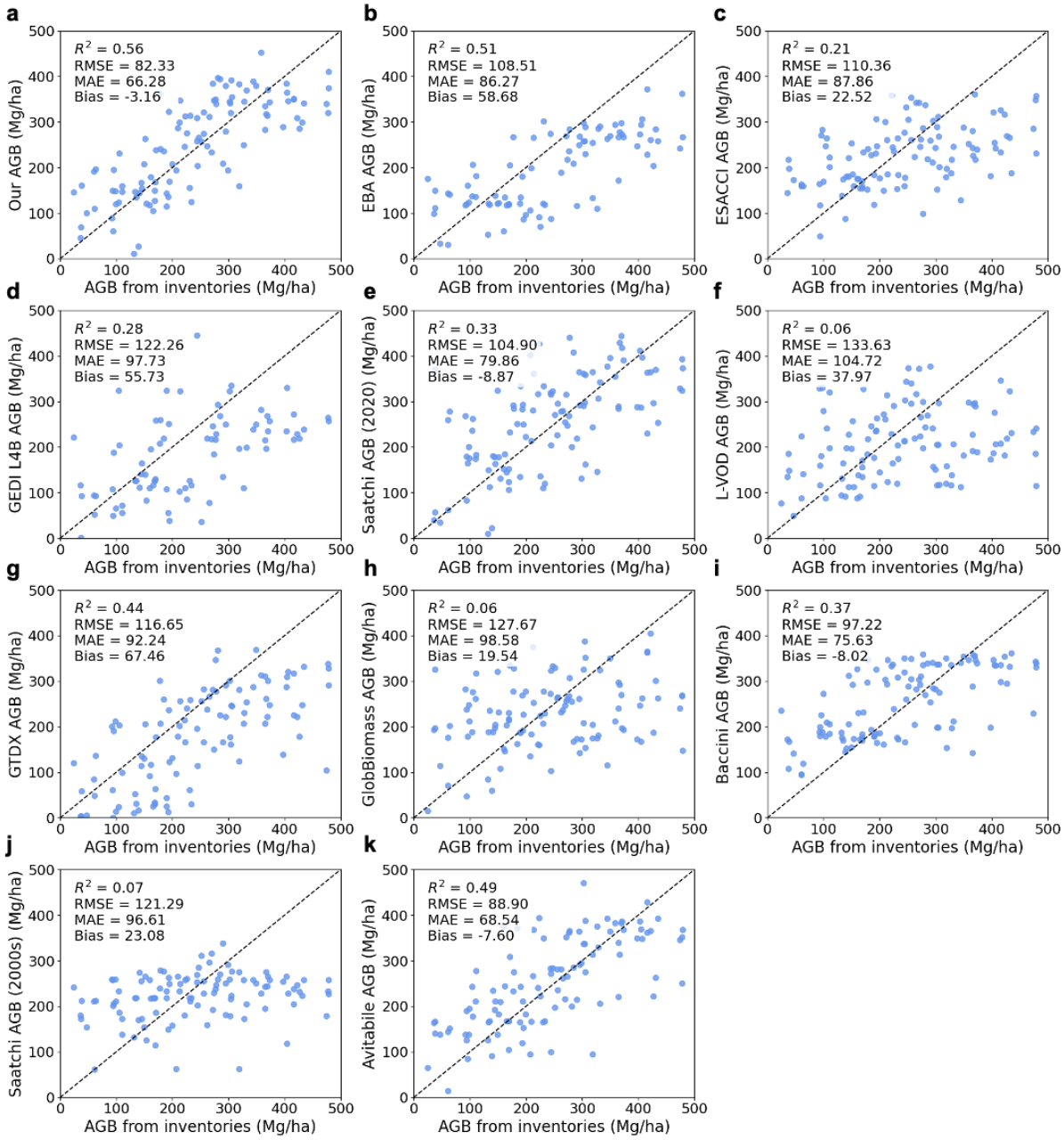



**Supplementary Fig. 9: Comparison of canopy height (CH) maps from airborne LiDAR and satellite-derived products.** Canopy height maps from airborne LiDAR (ALS, row 1), our model

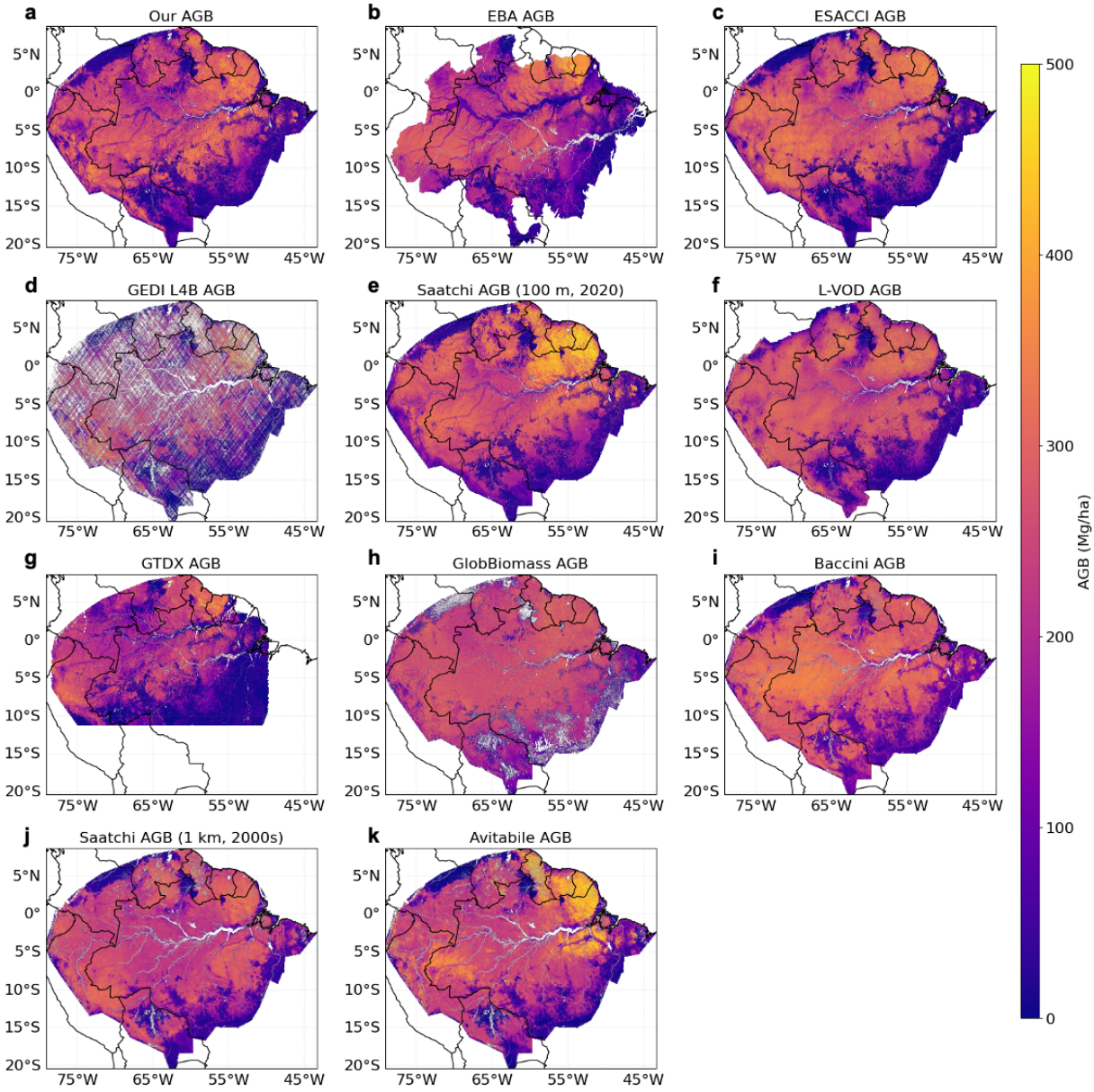
(row 2), and six existing products: GLAD (row 3), GTDX (row 4), ETH (row 5), Pauls (row 6), CTrees (row 7), and Meta mean CH (row 8), shown across six representative sites (**a–f**) in the Brazilian Amazon. ALS data were acquired as part of the Sustainable Landscapes Brazil Project (2016 to 2018) [15] and resampled to 10 meter resolution using maximum value aggregation within each grid cell.




**Supplementary Fig. 10: Fitted aboveground biomass (AGB) models using field inventory data**. Model performance for estimating AGB using either canopy height (CH) and wood density (WD) or CH alone. **a, b,** Training and validation results for models developed in Amazon dense forests using CH and WD (**a**) or CH only (**b**). **c, d,** Performance of AGB models developed in African dense forests when applied to the Amazon, using CH and WD (**c**) or CH only (**d**).



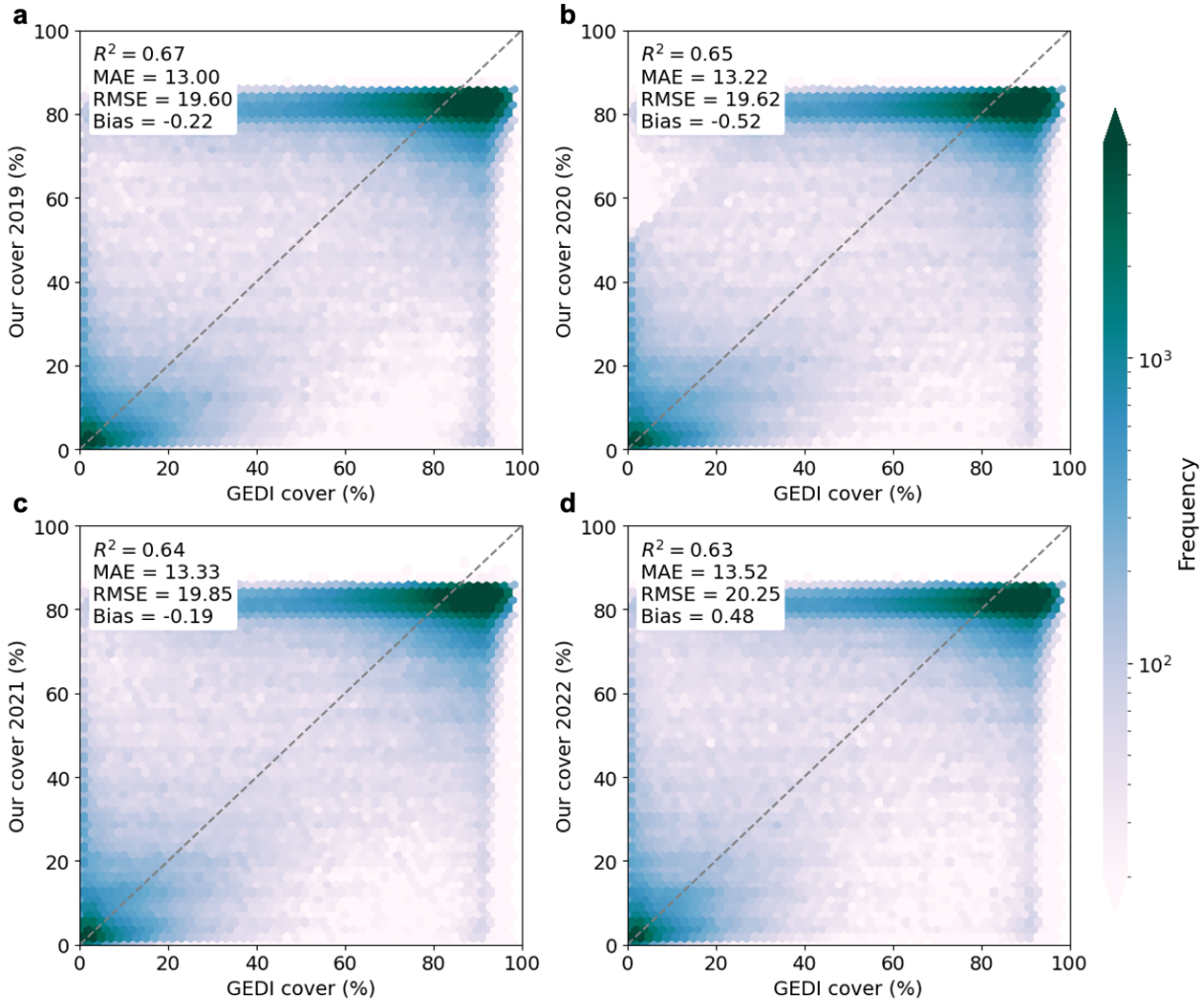

**Supplementary Fig. 11: Comparison of measured aboveground biomass (AGB) from field inventories with our AGB map and other published products. a,** Our AGB (30 m, 2019). **b,** EBA AGB [11]. **c,** ESACCI AGB (100 m, 2019) [60]. **d,** GEDI L4B AGB [61]. **e,** Saatchi AGB (100 m, 2020) [27]. **f,** L-VOD AGB (100 m, 2019). **g,** GDTX AGB [62]. **h,** GlobBiomass AGB [63]. **i,** Baccini AGB [64]. **j,** Saatchi AGB (1 km, 2020s) [26]. **k,** Avitabile AGB [65]. Performance was evaluated using an independent 20% validation subset of field inventory plots.



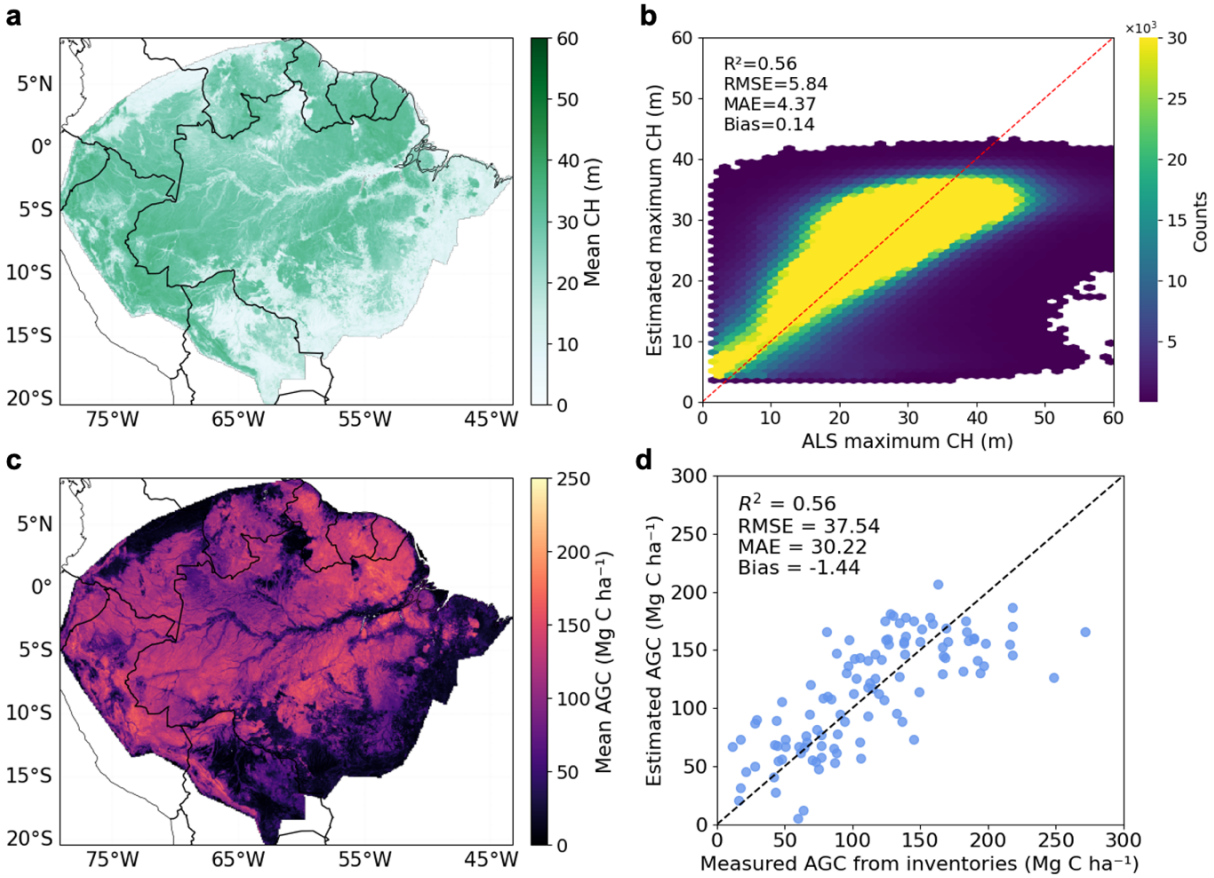

644

645 **Supplementary Fig. 12: Comparison of the spatial distribution of aboveground biomass (AGB)**
646 **in the Amazon forests. a,** our AGB (30 m). **b,** EBA AGB (250 m). **c,** ESACCI AGB (100 m, 2019).
647 **d,** GEDI L4B AGB (1 km). **e,** Saatchi AGB (100m, 2020). **f,** L-VOD AGB (100 m, 2019).**g,** GDTX
648 AGB (25 m). **h,** GlobBiomass (100 m). **i,** Baccini AGB (500 m). **j,** Saatchi AGB (1 km, 2000s). **k,**
649 Avitabile AGB (1km). Our AGB and GDTX AGB maps were resampled to 100 m resolution for
650 ease of presentation. All AGB maps were masked to match our mapping extent in the Amazon
651 forest.

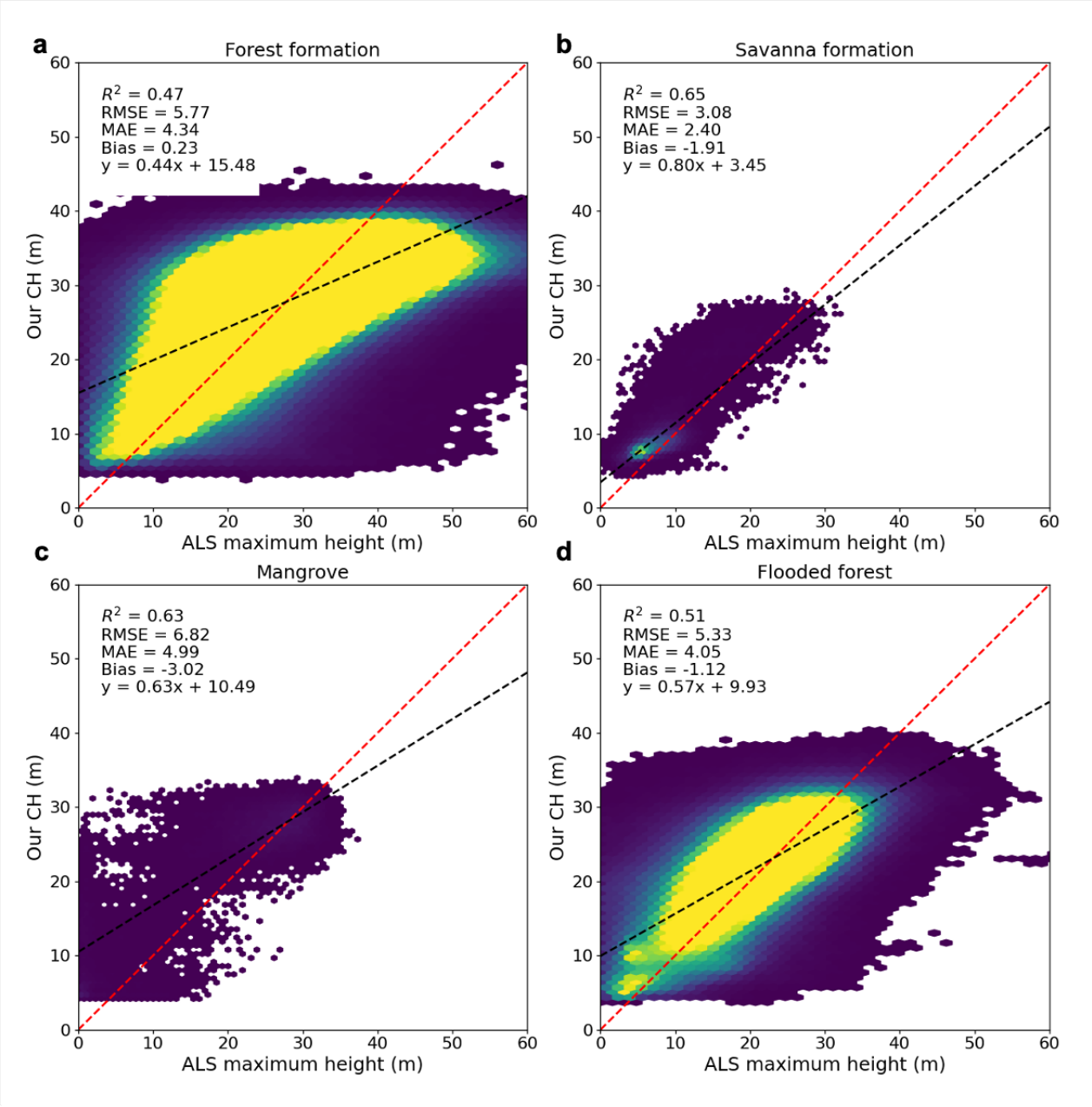
652




**Supplementary Fig. 13: Evaluation of annual canopy cover maps using independent GEDI canopy cover data in the Amazon forest. a–d,** All comparisons were conducted from 2019 to 2022. The GEDI cover data is derived from the GEDI Level 2B Canopy Cover and Vertical Profile Metrics product (GEDI02_B) [31].



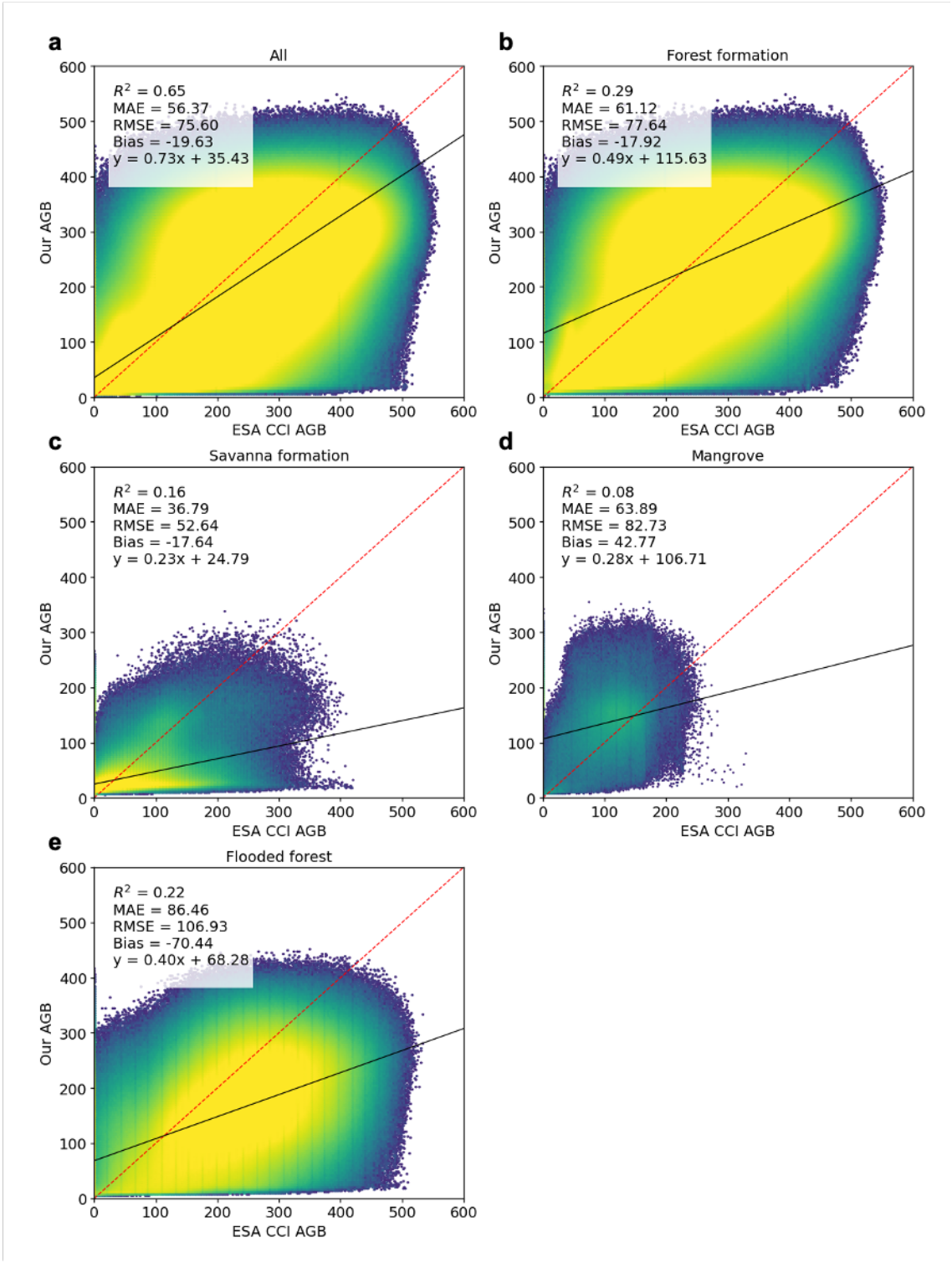

**Supplementary Fig. 14: Mapping of canopy height (CH) and aboveground carbon (AGC) in the Amazon forest. a, c,** Maps of 10-m CH and 30-m AGC for the Amazon forest in 2019, aggregated to a 5-km resolution by averaging to facilitate visualization at the regional scale. **b,** Validation of the 10-m CH estimates against independent airborne LiDAR (ALS)-derived maximum CH data. **d,** Validation of the 30-m AGC estimates against independent field inventory-based AGC measurements. AGC was derived from aboveground biomass (AGB) maps using a carbon fraction of 0.456 [66,67].




669

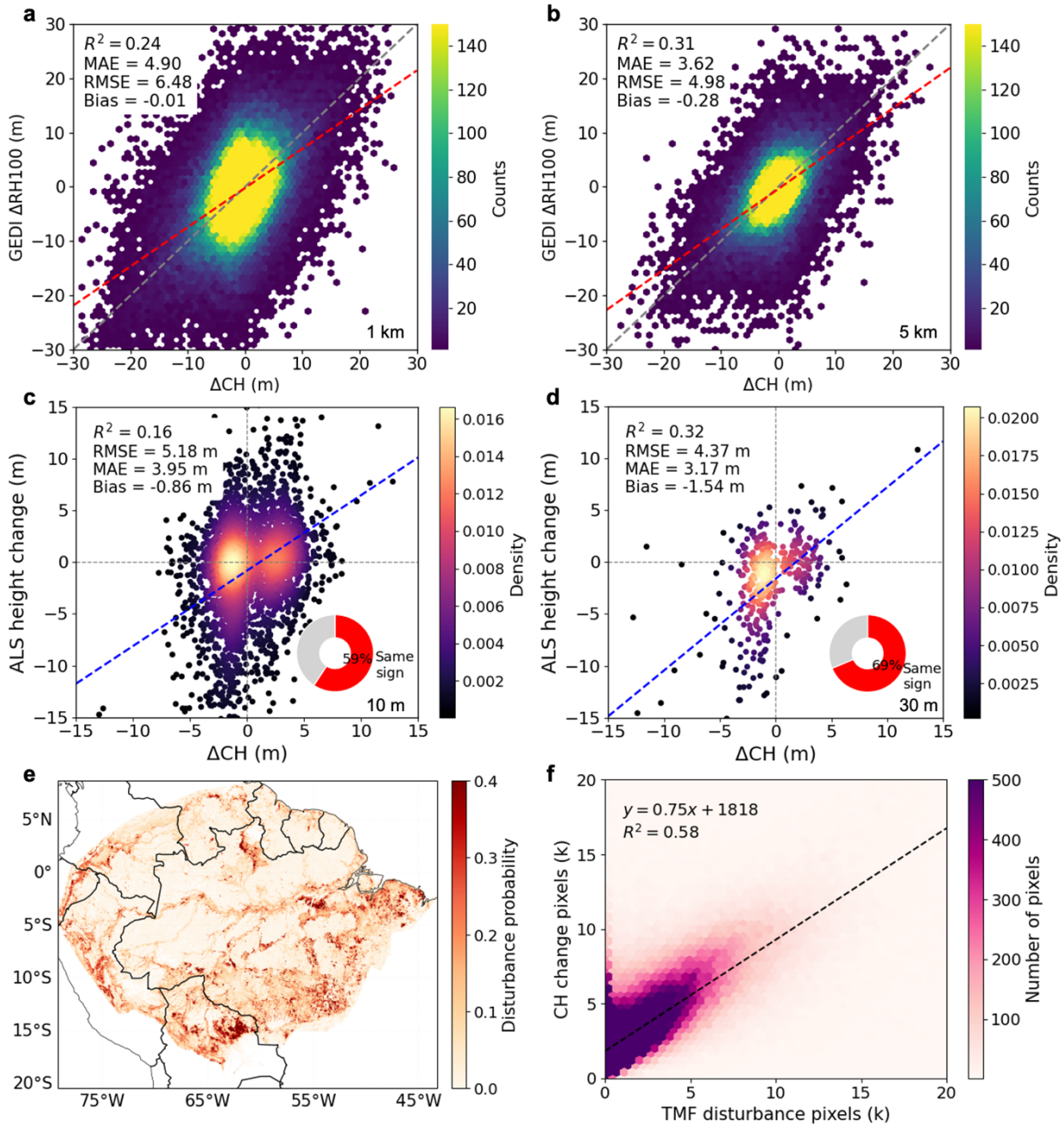
670 **Supplementary Fig. 15: Evaluation of canopy height estimates across major tropical**
671 **vegetation formations in the Amazon**. Hexagonal density plots comparing predicted canopy
672 height (Our CH) against airborne laser scanning (ALS) maximum height across four major
673 vegetation formations derived from the MapBiomas land-cover classification[68], including forest
674 formation (**a**), savanna formation (**b**), mangrove (**c**), and flooded forest (**d**). Colors indicate the
675 density of observations within each hexagonal bin. Red dashed lines represent the 1:1 relationship,
676 while black dashed lines indicate linear regression fits.

677



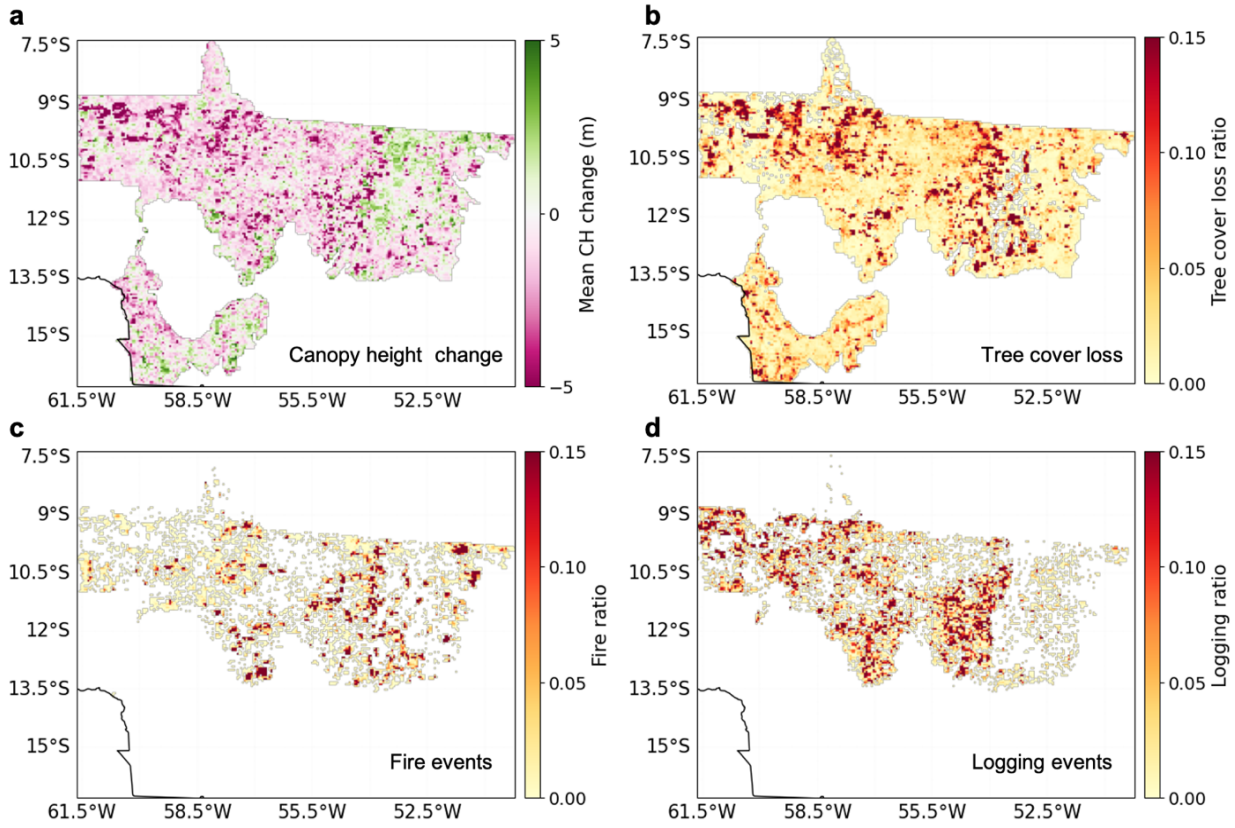

**Supplementary Fig. 16: Comparison of aboveground biomass estimates with ESA CCI biomass products across major tropical vegetation formations in the Amazon.** Hexagonal density plots comparing aboveground biomass (AGB) estimates derived in this study (Our AGB) against ESA Climate Change Initiative (ESA CCI) biomass products across all vegetation types (**a**) and four major MapBiomas land-cover formations[68], including forest formation (**b**), savanna formation (**c**), mangrove (**d**), and flooded forest (**e**). Colors indicate the density of observations

within each hexagonal bin. Red dashed lines represent the 1:1 relationship, while black solid lines indicate linear regression fits.

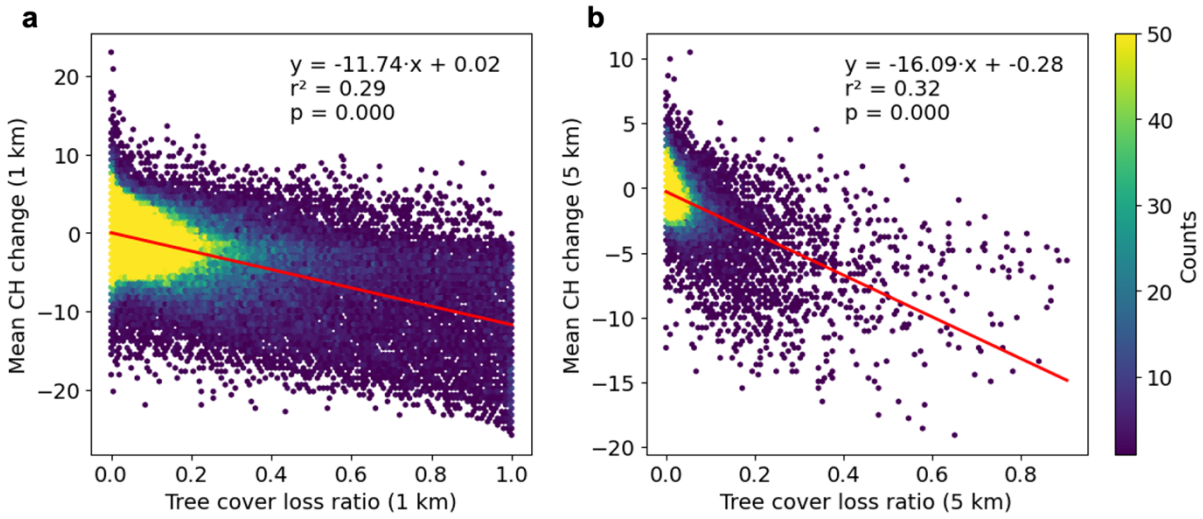



**Supplementary Fig. 17: Comparison of estimated canopy height change with reference datasets**. **a, b**, Comparison of estimated ΔCH and GEDI ΔRH100 at 1-km (**a**) and 5-km (**b**) resolution across the entire Amazon, with validation results across multiple spatial scales provided in **Supplementary Fig. 23**. The gray and red dashed lines indicate the 1:1 line and the linear regression line, respectively. **c, d**, Comparison of estimated ΔCH and maximum height change from airborne LiDAR (ALS) at 10 m (**c**) and 30 m (**d**) resolution collected in the Caxiuanã and Jamari

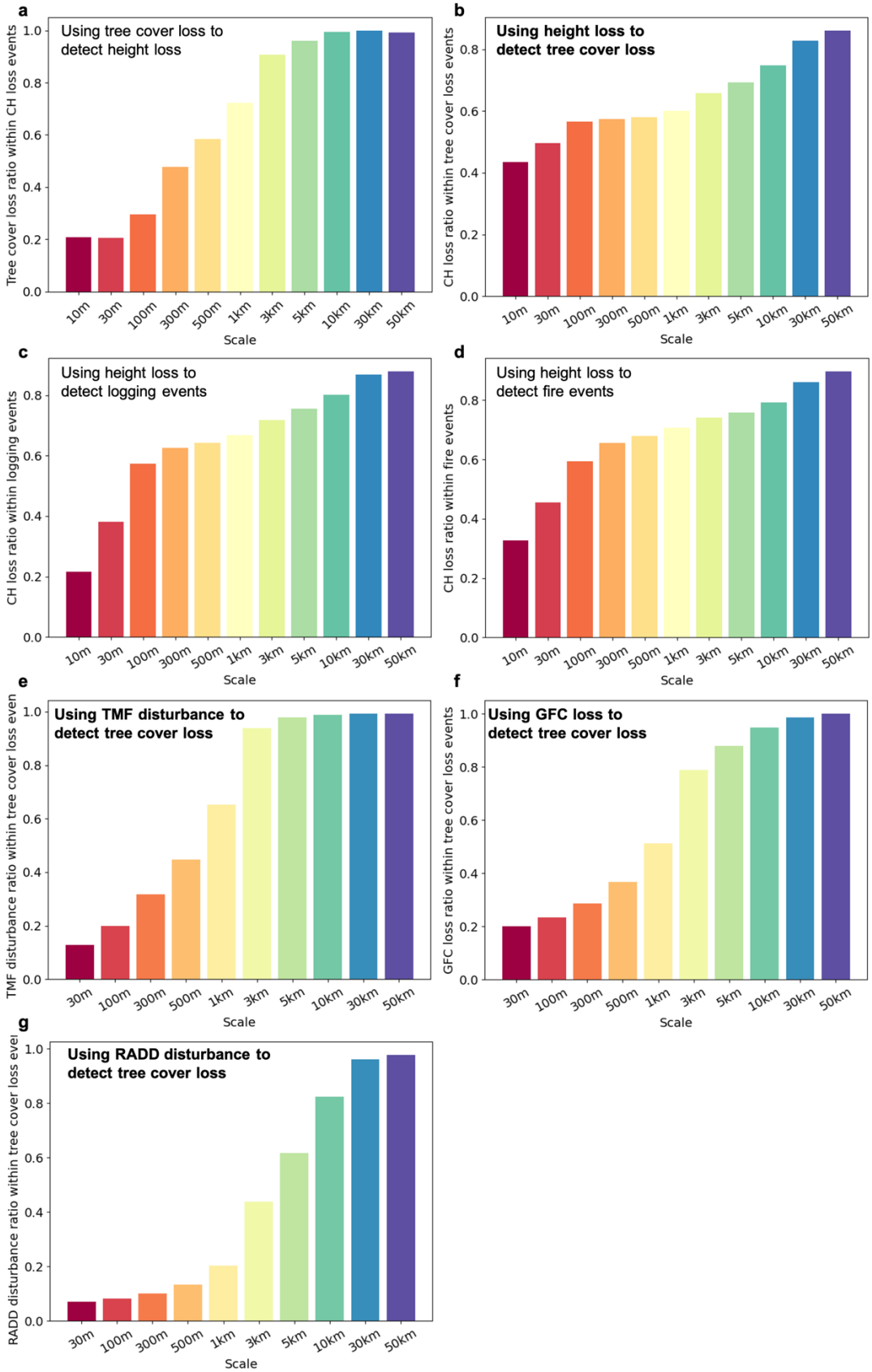
National Forest, which are primarily covered by undisturbed forests according to the TMF dataset. The percentage of pixels for which the two height-change datasets exhibit the same sign (gain or loss) is indicated. The blue dashed line represents the linear regression fit. **e,** Disturbance probability map aggregated at 5-km grid scale, derived from the Tropical Moist Forest (TMF) degradation and deforestation data. **f,** Comparison of the number of CH change pixels and TMF disturbance pixels within each 5-km grid cell.




**Supplementary Fig. 18: Comparisons of canopy height (CH) change and independent disturbance events in the Brazilian state of Mato Grosso. a–d**, Spatial distribution of mean CH change (**a**) and the proportion of tree cover loss (**b**), logging (**c**), and fire (**d**) within 5-km grid cells. Mean CH change was calculated from all pixels showing change, and the ratios of tree cover loss, logging, and fire were derived as the proportion of disturbance pixels relative to all pixels within each 5-km grid cell. Tree cover loss, logging, and fire data were derived from high-resolution Planet imagery (~5 m) [32,33]. We considered CH change and disturbance events occurring between 2019 and 2022.




**Supplementary Fig. 19**: **Comparison of canopy height (CH) change and tree cover loss in the Brazilian state of Mato Grosso. a,b,** Relationship between mean CH change and tree cover loss ratio within 1-km (**a**) and 5-km (**b**) grid cells. Mean CH change was calculated from all change pixels, and tree cover loss ratio was derived from the proportion of loss pixels relative to all pixels. Tree cover loss data were generated using high-resolution Planet imagery (~4.77 m) [33].

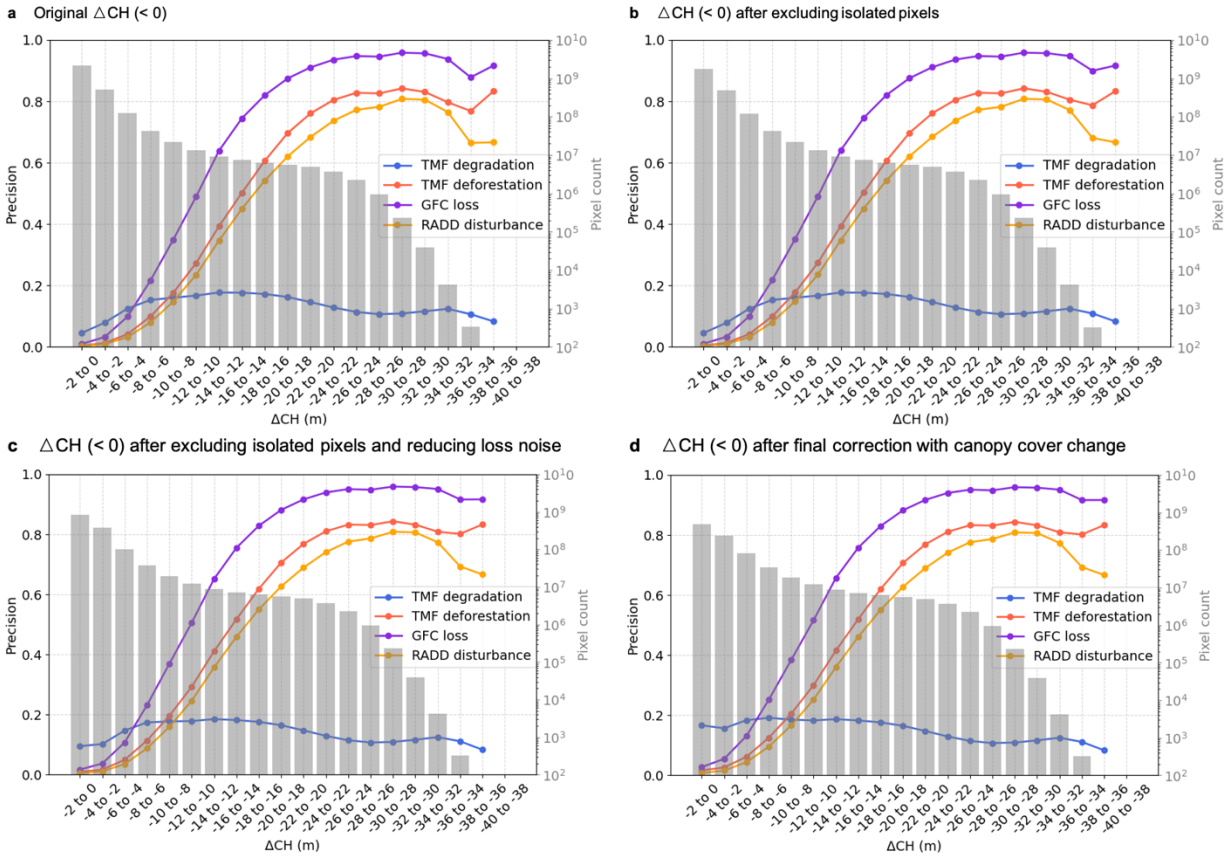



717

718 **Supplementary Fig. 20**: **Detection rates of canopy height loss and disturbance data relative to**

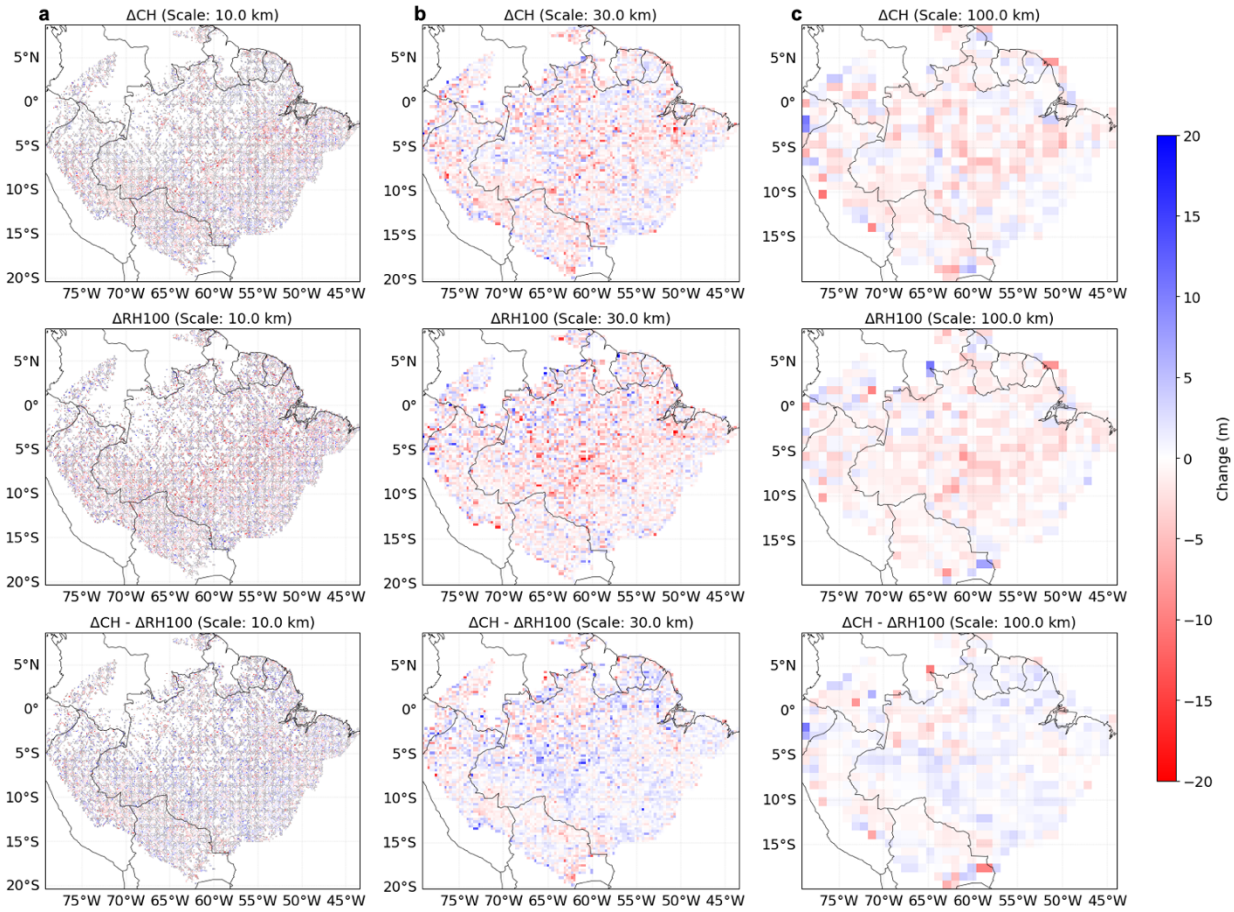
719 **independent disturbance events across scales in the Brazilian state of Mato Grosso.** Detection

rates of canopy height (CH) loss were compared against independent datasets of tree cover loss (**a, b**), logging (**c**), and fire (**d**) across spatial scales ranging from 10 m to 50 km. **a**, Fraction of CH loss pixels that coincide with mapped tree cover loss. **b**, Fraction of tree cover loss pixels that coincide with CH loss. **c**, Fraction of logging pixels with CH loss. **d**, Fraction of fire pixels with CH loss. Detection rates increased with spatial scale, indicating stronger correspondence at coarser resolutions, likely due to the differences in data type, resolution and detection timing. Detection rates of Tropical Moist Forest (TMF) disturbance (**e**), Global Forest Change (GFC) loss (**f**), and radar-based RAdar for Detecting Deforestation (RADD) disturbances (**g**) were compared against independent datasets of tree cover loss across spatial scales ranging from 30 m to 50 km. Tree cover loss, fire and logging data were generated using high-resolution Planet imagery (~5 m) [32,33].

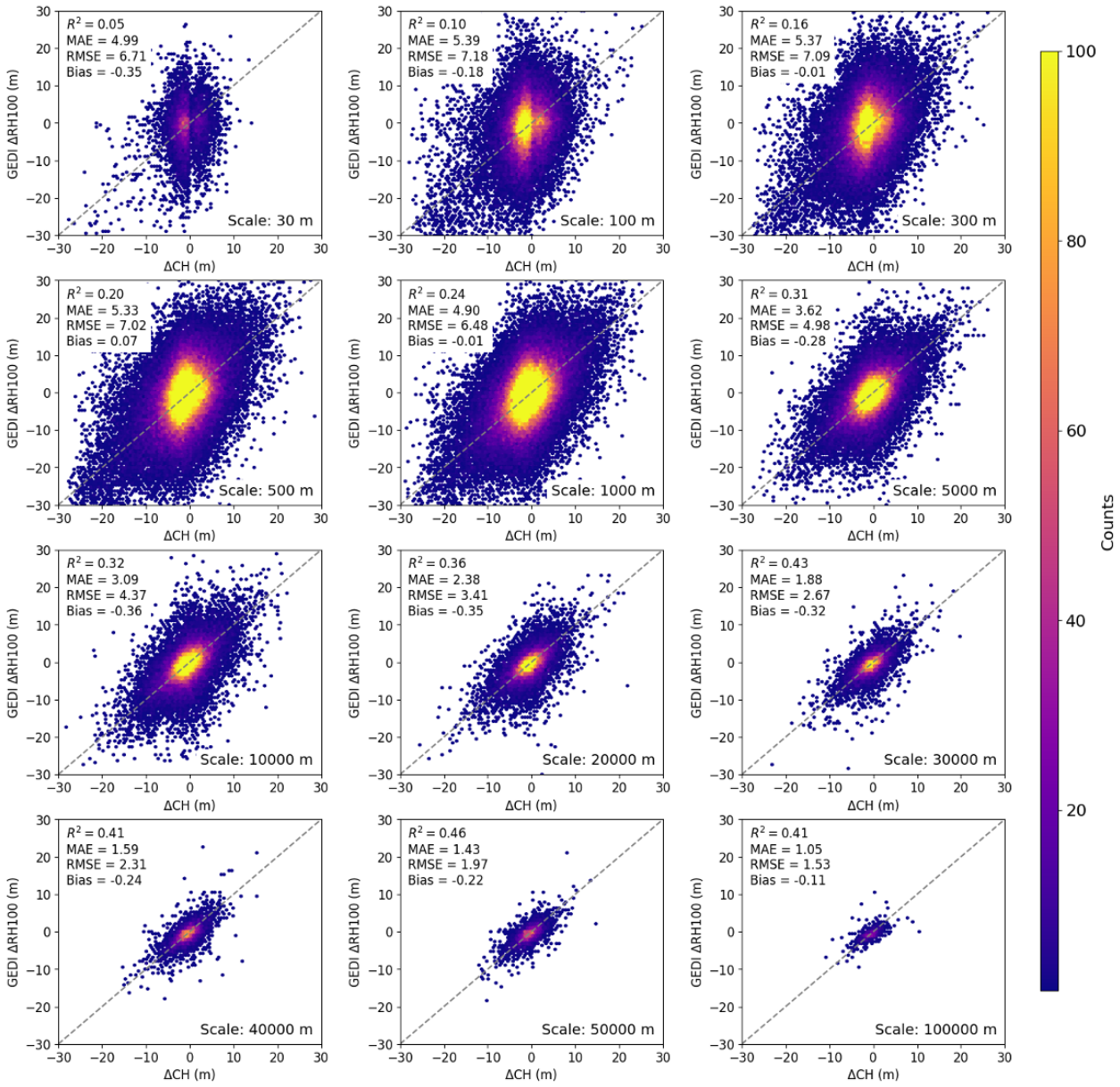



**Supplementary Fig. 21: Precision estimates of canopy height (CH) loss from 2019 to 2022 compared with various disturbance datasets.** We applied a three-step process to filter the original CH change maps and evaluated their agreement with commonly used disturbance datasets,

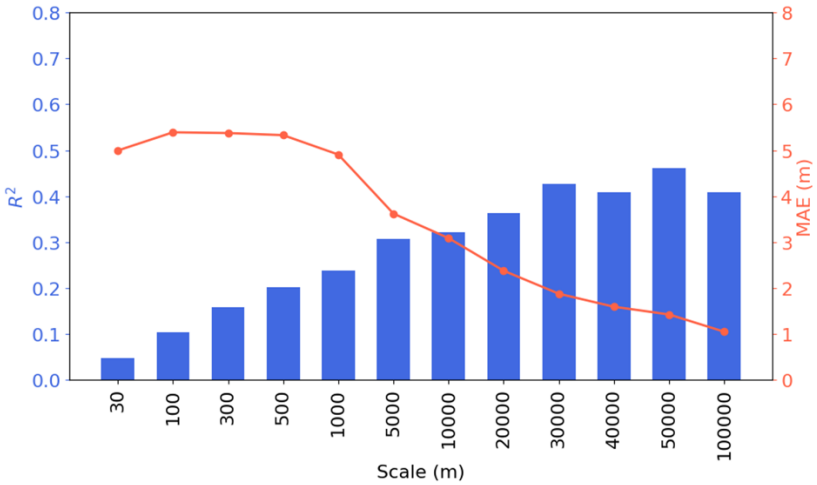
including Tropical Moist Forest (TMF) degradation, TMF deforestation, Global Forest Change (GFC) loss, and radar-based RAdar for Detecting Deforestation (RADD) alerts. Estimates of original CH loss (ΔCH < 0) are shown in: (a) the original map; (b) after excluding isolated pixels; (c) after further removal of noise-related loss; and (d) after final correction using canopy cover change.



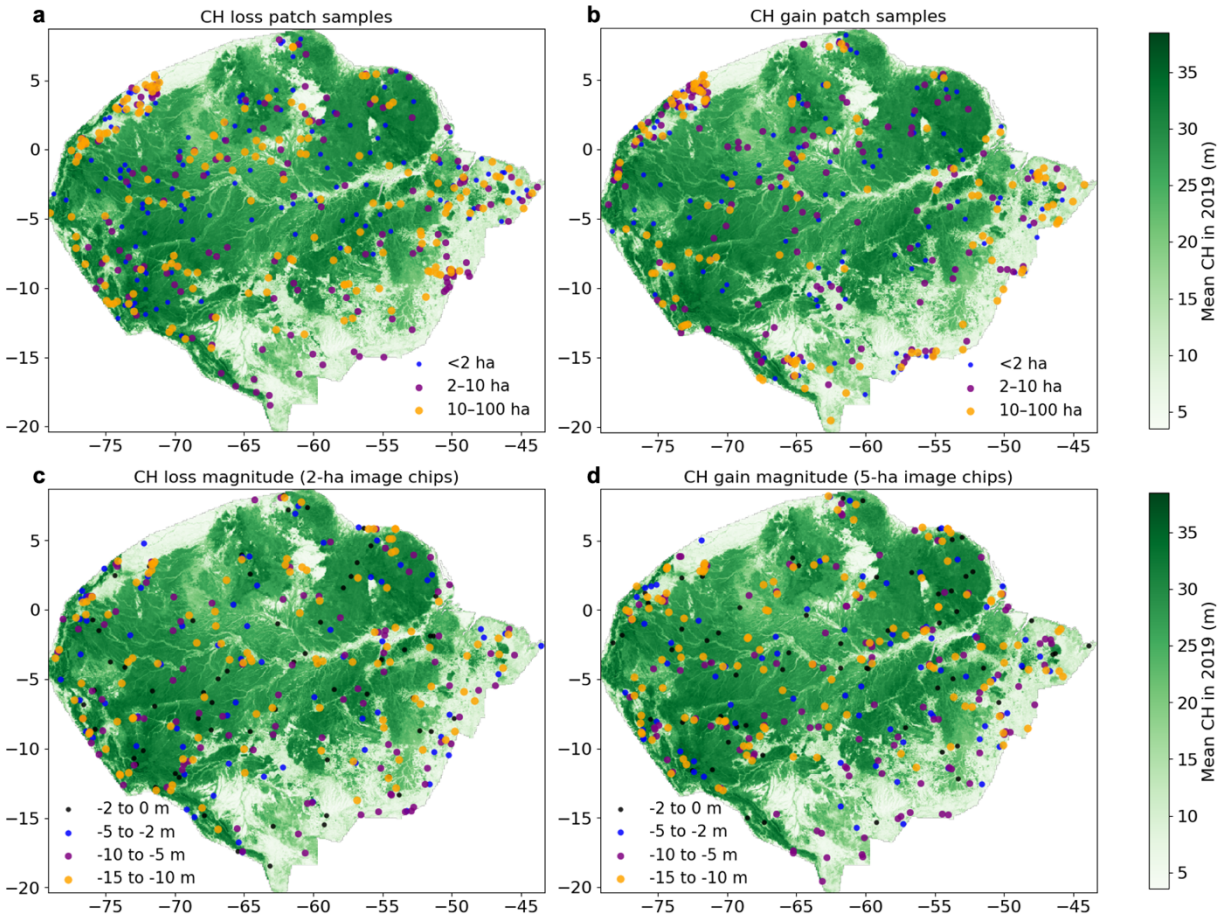

**Supplementary Fig. 22**: **Comparison of processed canopy height (CH) change and GEDI RH100 change maps, along with their differences, at three spatial scales.** CH change (ΔCH) and GEDI RH100 change (ΔRH100) were calculated as the difference between the 2022 and 2019 data. The 30 m data were aggregated to coarser resolutions for more robust comparisons: (a) 10 km; (b) 30 km; and (c) 100 km. CH change was processed to remove unchanged pixels as well as isolated or noisy pixels.




**Supplementary Fig. 23: Comparison of processed canopy height (CH) change and GEDI RH100 change from 2019 to 2022 in the Amazon.** Due to the limited availability of repeated GEDI observations in 2019 and 2022, as well as geolocation uncertainty, it is challenging to estimate height change at high spatial resolutions (e.g., 10–30 m). Therefore, the 30 m data were aggregated to coarser resolutions to enable more robust comparisons. CH change was processed to remove unchanged pixels as well as isolated or noisy pixels.




**Supplementary Fig. 24: Performance evaluation of processed canopy height (CH) change and GEDI RH100 change from 2019 to 2022 across multiple spatial scales.** ΔCH and ΔRH100 were calculated as the difference between the 2022 and 2019 data. The 30 m data were aggregated to coarser spatial resolutions to allow for more robust comparisons.

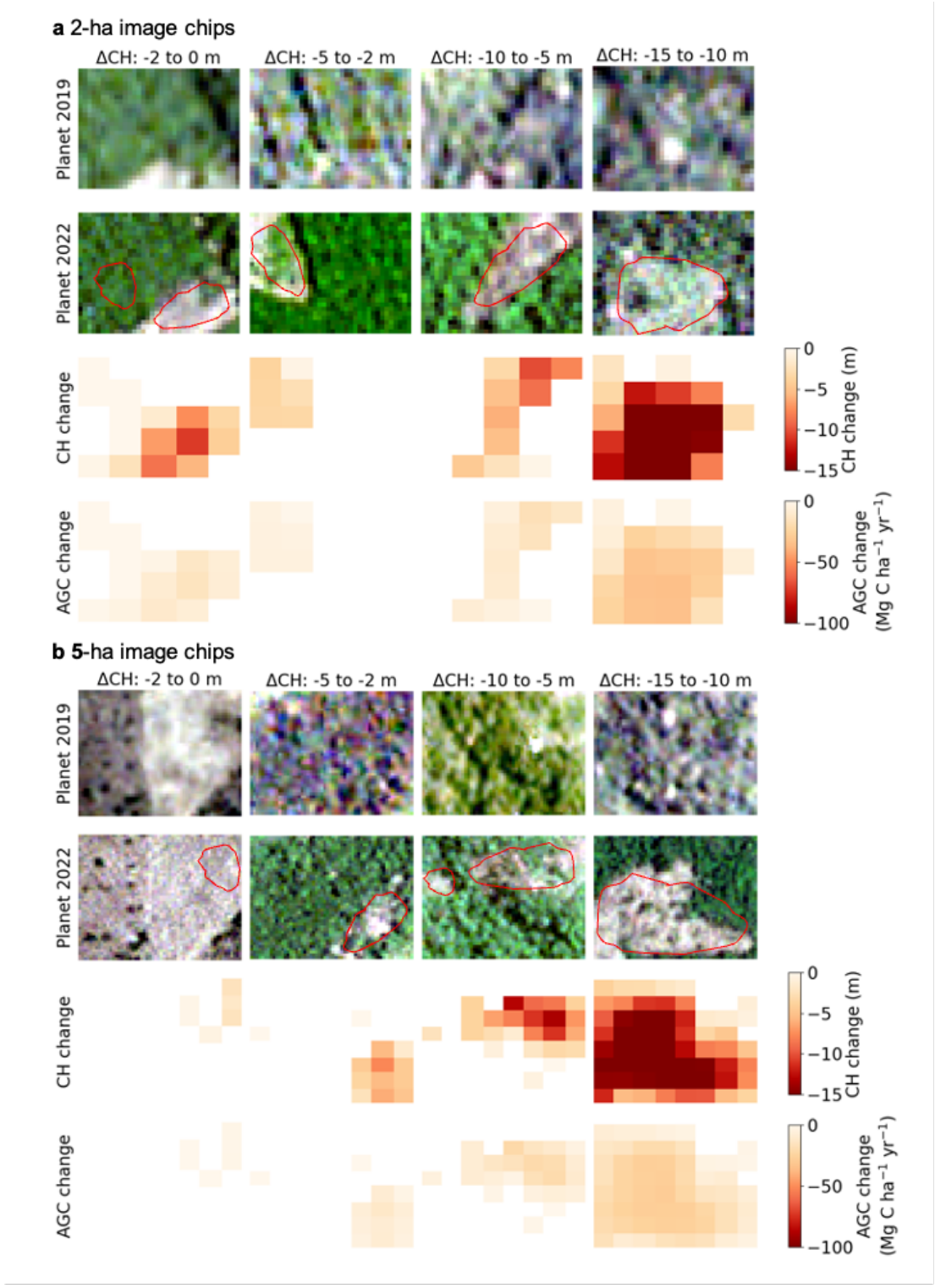



765

766 **Supplementary Fig. 25: Spatial distribution of canopy height (CH) loss and gain patch**
767 **samples and representative image chips from high-resolution (5 m) PlanetScope imagery**
768 **across the Amazon. a, b,** Spatial distribution of sampled CH-loss (**a**) and CH-gain (**b**) patches,
769 respectively, grouped into three patch-size classes (<2 ha, 2–10 ha, and 10–100 ha). **c, d,** Spatial
770 distribution of randomly sampled 2-ha (**c**) and 5-ha (**d**) image chips used for visual interpretation
771 of CH-loss magnitude classes ($-2 \leq \Delta CH < 0$ m, $-5 \leq \Delta CH < -2$ m, $-10 \leq \Delta CH < -5$ m, and
772 $-15 \leq \Delta CH < -10$ m), respectively. The background shows the mean canopy height (CH) in 2019
773 at 5-km resolution.

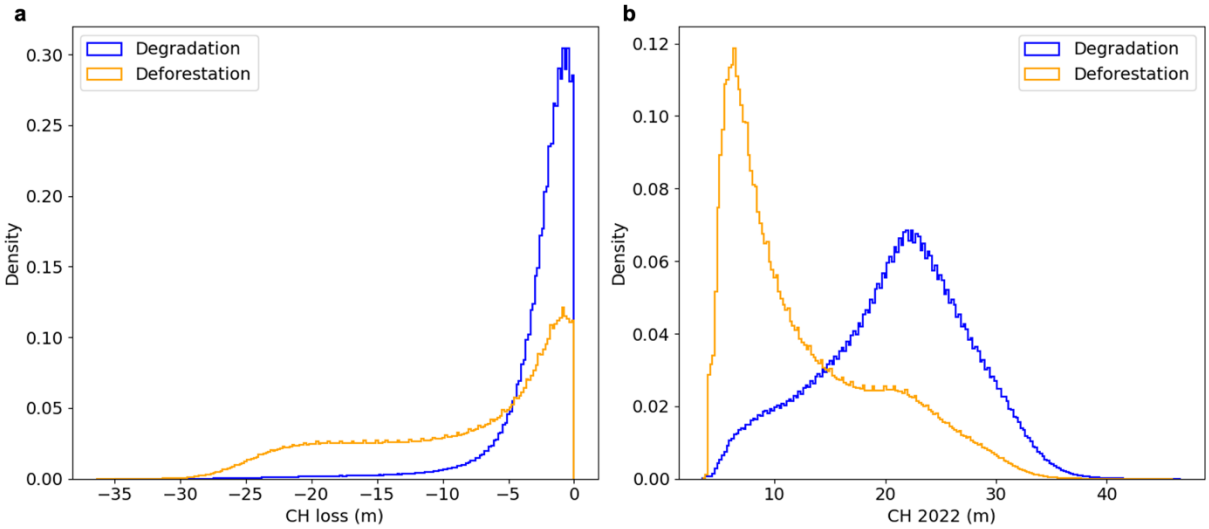
774

775

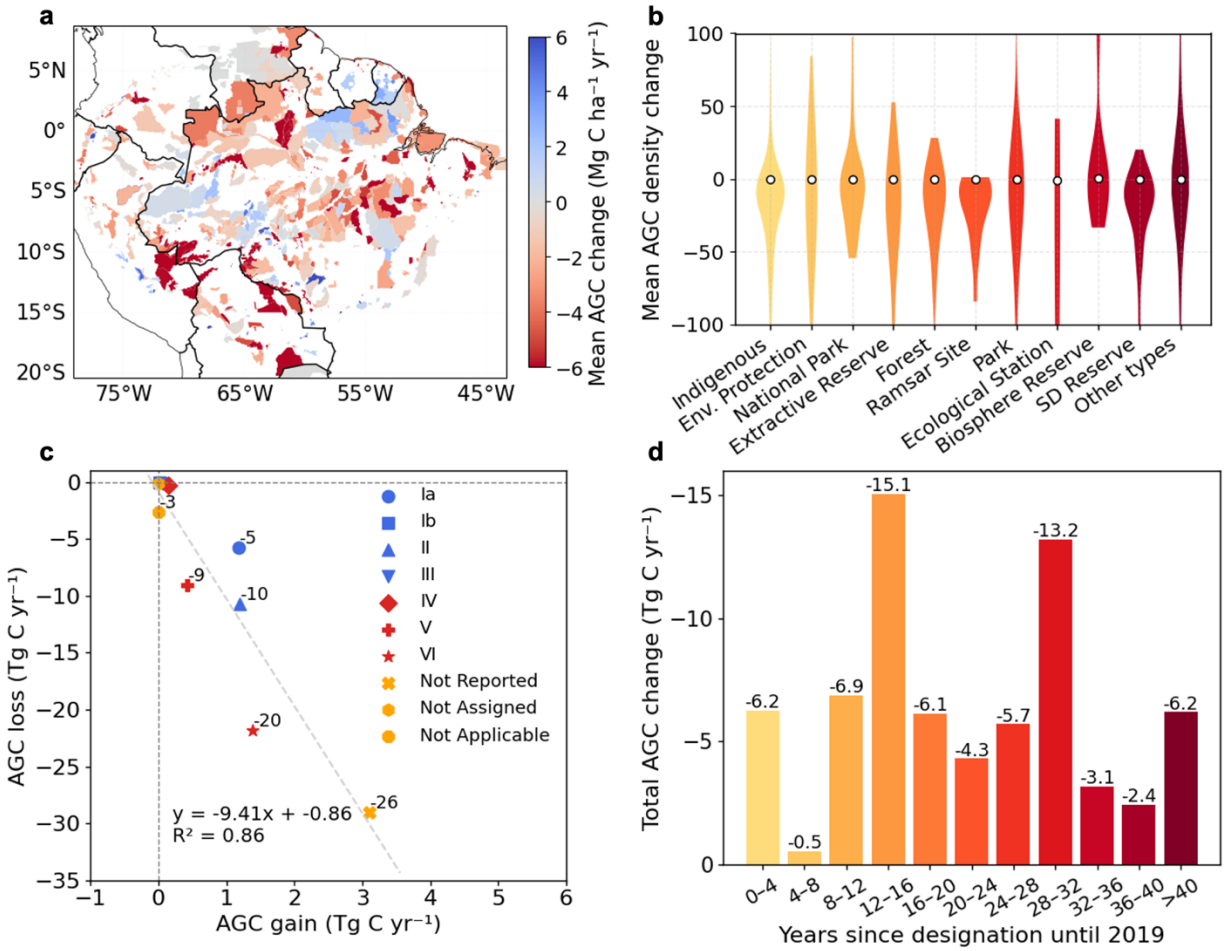



**Supplementary Fig. 26: Examples of canopy height (CH) loss and corresponding aboveground carbon (AGC) change across different CH-loss magnitude classes.** Representative examples of CH-loss detections are shown for four CH-loss magnitude classes ($-2 \leq \Delta CH < 0$ m, $-5 \leq \Delta CH < -2$ m, $-10 \leq \Delta CH < -5$ m, and $-15 \leq \Delta CH < -10$ m), using randomly sampled 2-ha (**a**) and 5-ha (**b**) image chips interpreted from 5-m Planet imagery. For each example, the top two rows show PlanetScope imagery acquired in 2019 and 2022, respectively, followed by

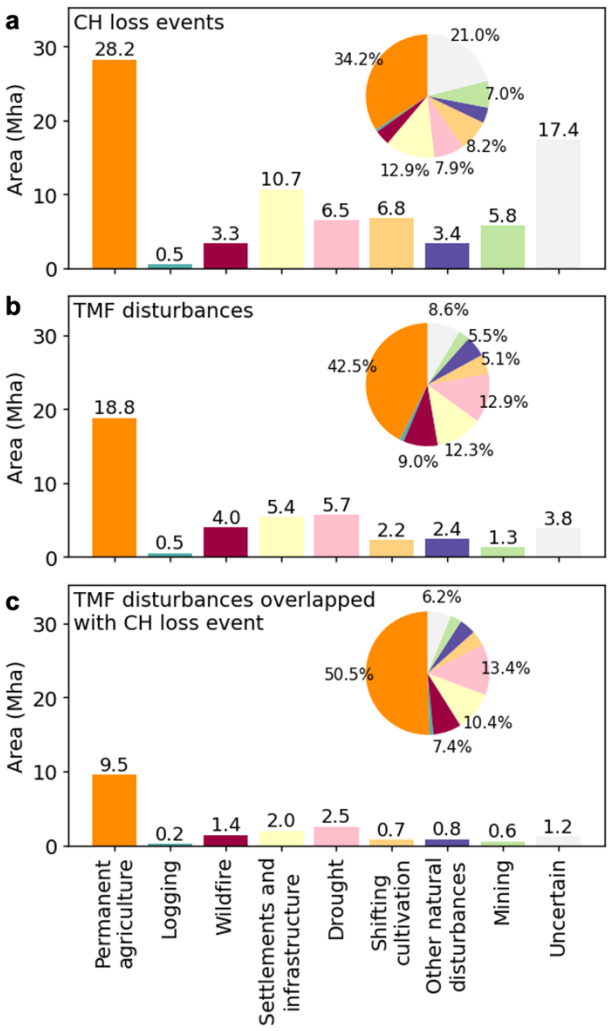
the corresponding 30-m CH-change map and AGC-change map (2019–2022). Red outlines delineate the regions that exhibit visible changes between the 2019 and 2022 PlanetScope images. These examples illustrate how visually identifiable canopy disturbances correspond to progressively greater canopy-height loss and associated AGC loss across the four CH-loss magnitude classes.



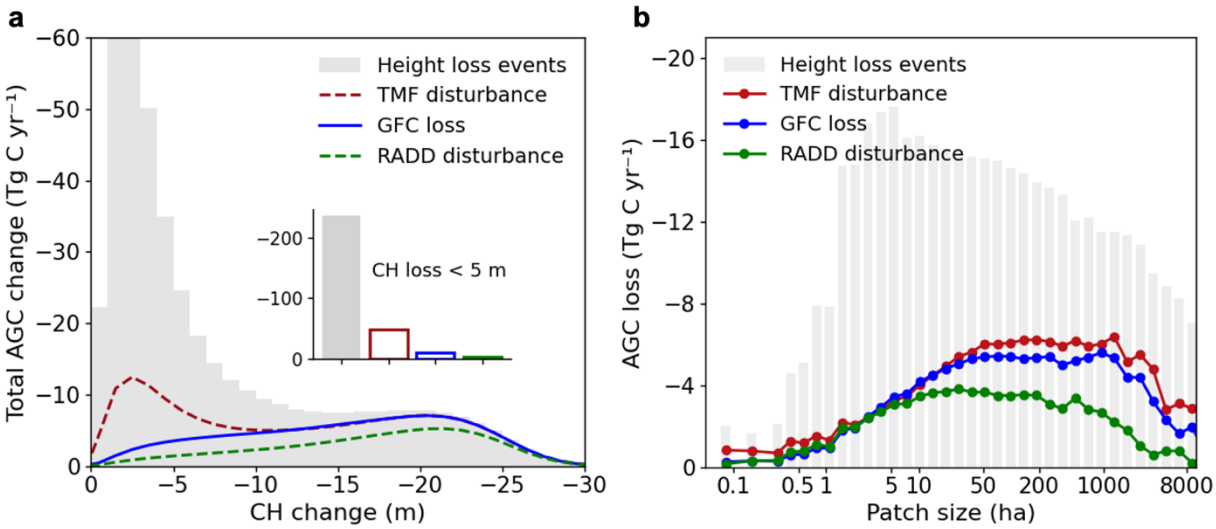

**Supplementary Fig. 27: Distribution of canopy height (CH) loss and CH in 2022 in areas of Tropical Moist Forest (TMF) degradation and deforestation. a,** CH loss in pixels labeled as TMF degradation and deforestation between 2019 and 2022, after processing. **b,** CH in 2022 in pixels labeled as TMF degradation and deforestation between 2019 and 2022.




**Supplementary Fig. 28: Aboveground carbon (AGC) changes across protected area types, management categories, and designation ages. a,** Spatial patterns of mean AGC density change from 2019 to 2022, displayed for each protected area. **b**, The distribution of mean AGC density change (Mg C $ha^{-1}$ $yr^{-1}$) by protected area type, including Indigenous land, Environmental Protection Area, Extractive Reserve, and others. The top 10 categories with the greatest AGC loss are shown; remaining types are grouped as "other types". **c,** AGC gain versus loss for different IUCN protected area categories. Each point represents one IUCN category, with marker shape and color indicating category type. Horizontal and vertical dashed lines denote zero AGC loss and gain, respectively. As in panel a, only categories with substantial net AGC change (> 2 Tg C $yr^{-1}$) are labeled. **d,** Total AGC change from 2019 to 2022 for protected areas, grouped by year of designation (until 2019) in 4-year intervals.

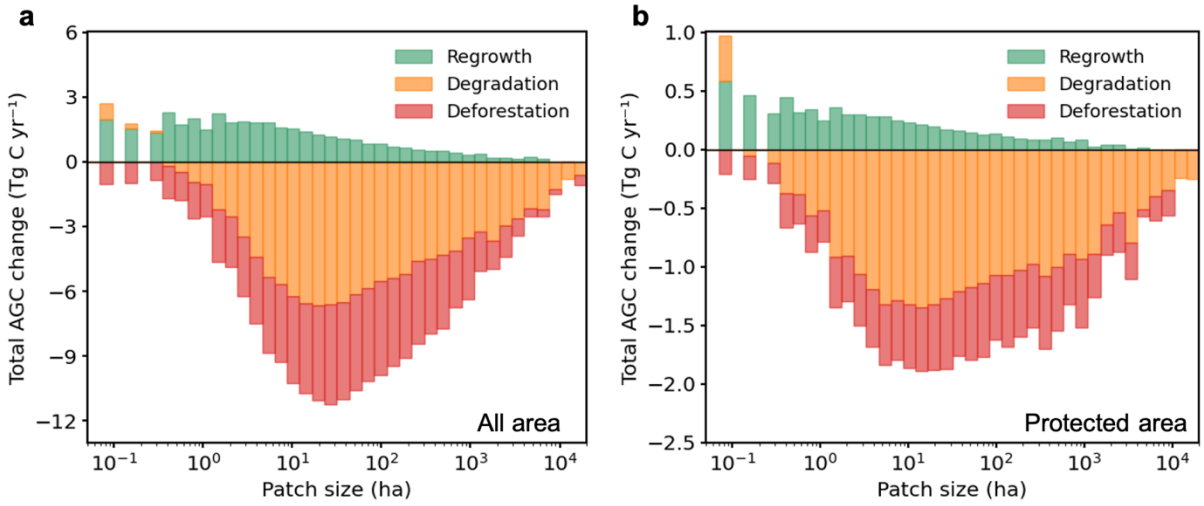



**Supplementary Fig. 29: Comparison of canopy height (CH) loss and Tropical Moist Forest (TMF) disturbances by loss driver. a,** Total area of canopy height loss events from 2019 to 2022 attributed to different disturbance drivers, with inset pie chart showing their percentage contributions. **b,** Total TMF disturbance area during the same period grouped by driver, with corresponding percentage breakdown. **c,** Area of TMF disturbances that overlapped with CH loss events, indicating structural disturbance, categorized by driver type. All values are in million hectares (Mha). Pie charts display proportional contributions of each driver. The analyses were conducted at 1-km grid cell resolution, consistent with the spatial resolution of the loss driver data. (see **Methods**).

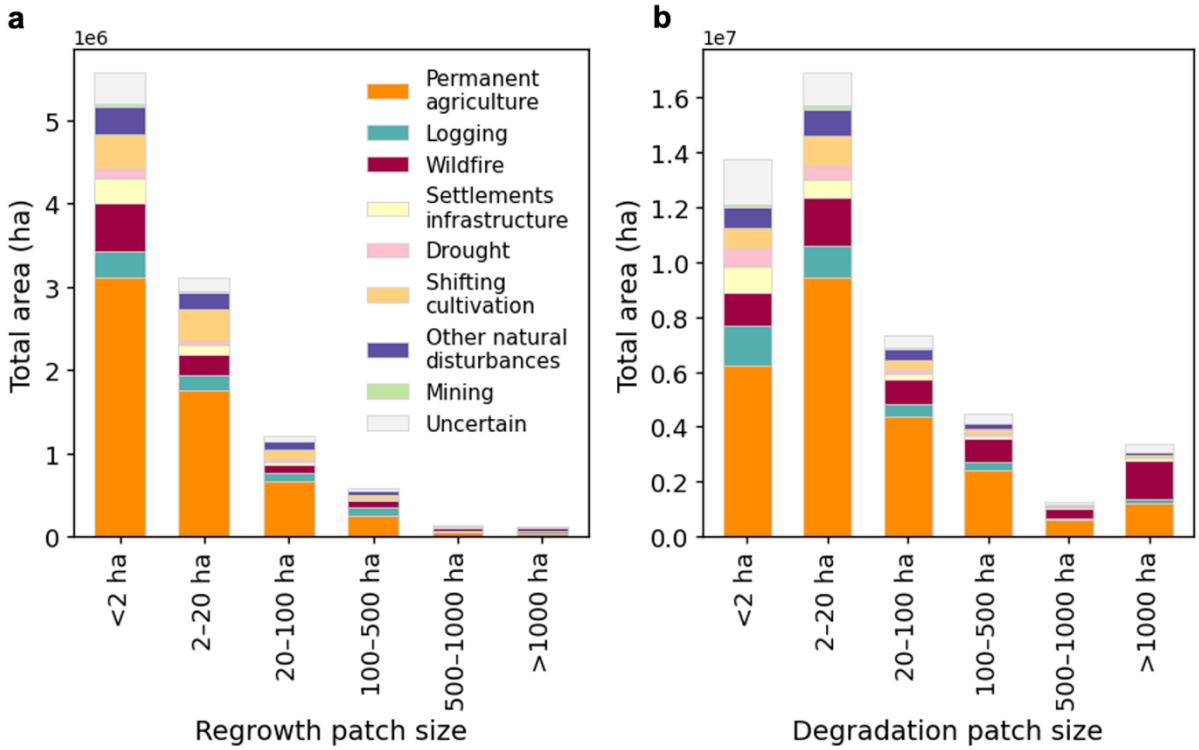



819

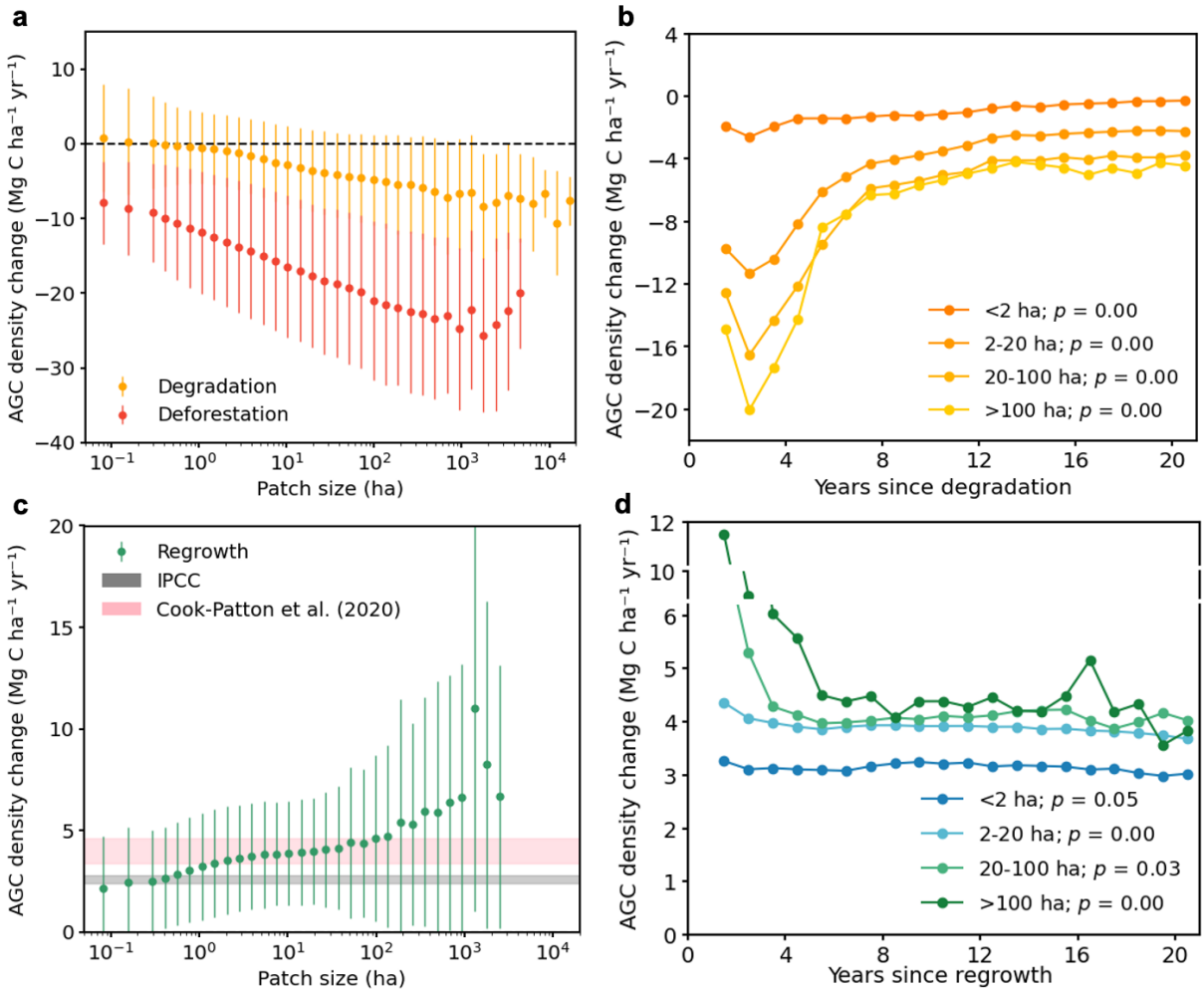
820 **Supplementary Fig. 30: Comparison of carbon loss detected by different reference**
821 **disturbance datasets**. **a,** Total aboveground carbon (AGC) change associated with CH loss (ΔCH
822 < 0) and other disturbance datasets across CH loss bins, including the Tropical Moist Forest (TMF),
823 Global Forest Change (GFC), and radar-based RAdar for Detecting Deforestation (RADD) datasets.
824 Inset shows total AGC loss from CH loss <10 m compared across datasets. We overlaid the AGC
825 change map with various disturbance datasets to quantify carbon change. **b,** AGC loss by patch size
826 class for CH loss and other disturbance datasets. Grey bars indicate AGC loss from CH loss patches.
827 Patch size was grouped into 51 logarithmically spaced bins ranging from 0.01 to 100,000 ha. A
828 logarithmic scale was applied to better visualize variation that would be obscured on a linear scale.




**Supplementary Fig. 31: Aboveground carbon (AGC) change (2019 to 2022) across varying patch size in the Amazon forest. a, b,** Total AGC change in the Amazon (**a**) and protected area (**b**) from forest regrowth, degradation and deforestation across patch sizes. Patch sizes were derived from canopy height change maps specific to each disturbance class.

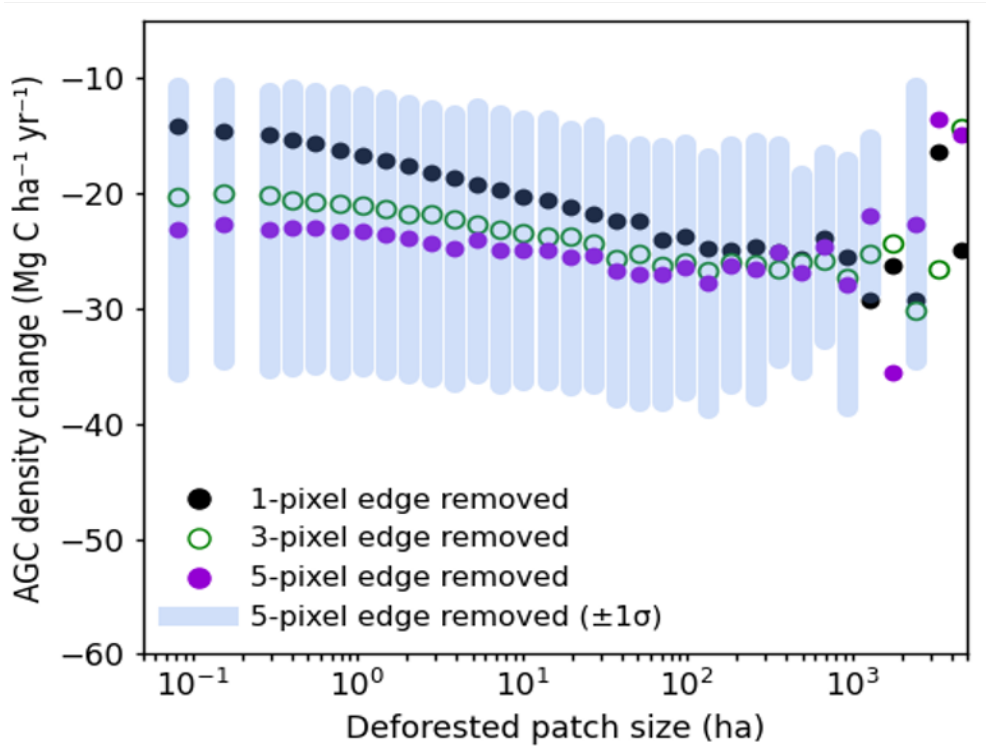



**Supplementary Fig. 32: Distribution of loss driver areas across patch size classes. a, b,** Total area of loss drivers across and proportions (**b**) of afforestation, plantation, burned, and other pixels across regrowth (**a**) and degradation (**b**) patch size classes. We generated the loss drivers map by integrating the existing 1-km dataset covering global patterns of primary forest loss drivers [56], a 30-m Landsat-based burned area map [69], a 5-m high-resolution road map drawn from Planet data [70], and additional inputs from coarse-resolution Amazon forest degradation driver maps (0.09–0.5°)[71] (**Methods**).

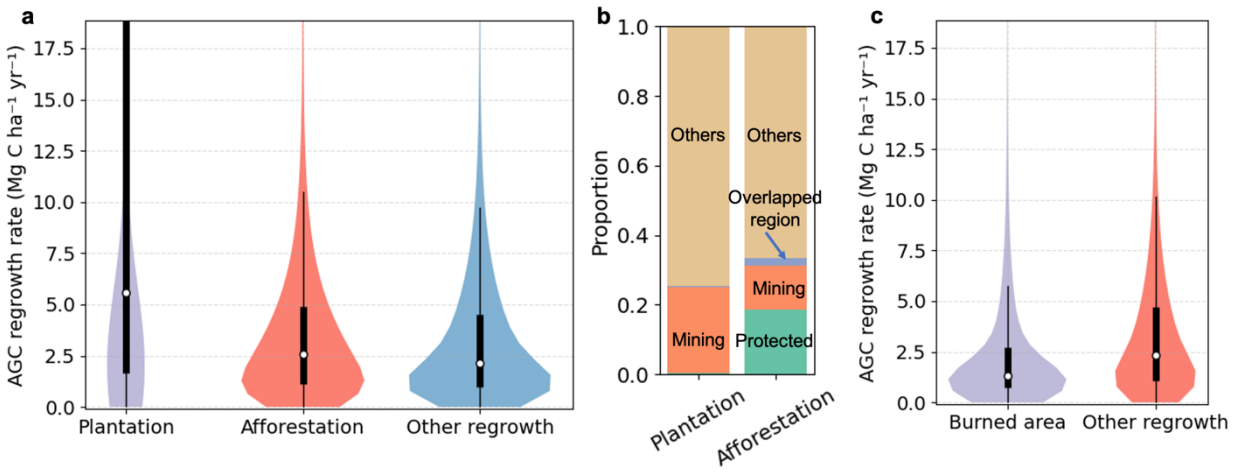



**Supplementary Fig. 33: Distribution of aboveground carbon (AGC) density change (2019 to 2022) by patch size and disturbance years in the Amazon. a, c,** AGC density change associated with degradation and deforestation (**a**) and forest regrowth (**c**) across different patch size bins. For each patch-size bin, mean values and associated standard deviations are shown for bins containing at least three valid observations. Patch sizes were derived from canopy height change maps specific to each TMF disturbance class. We compared the estimated AGC density growth rate with values from the refined IPCC defaults [49] and Cook-Patton et al. (2020) [48], and the displayed ranges represent values typical of tropical rainforests and moist forests (**Supplementary Table 12**). **b,** AGC density changes across patch sizes over post-degradation years. Mean values and trend lines (slope and *p*) are shown. AGC density change was quantified for 2019–2022, while the age of degradation and regrowth patches was derived from the long-term Tropical Moist Forests dataset,

enabling analysis of carbon dynamics up to 21 years after disturbance. **d,** AGC density changes across patch sizes over regrowth years after deforestation. A broken y-axis is used for patches >100 ha, where AGC density changes are disproportionately large, to enhance visibility of trends across smaller patch sizes.

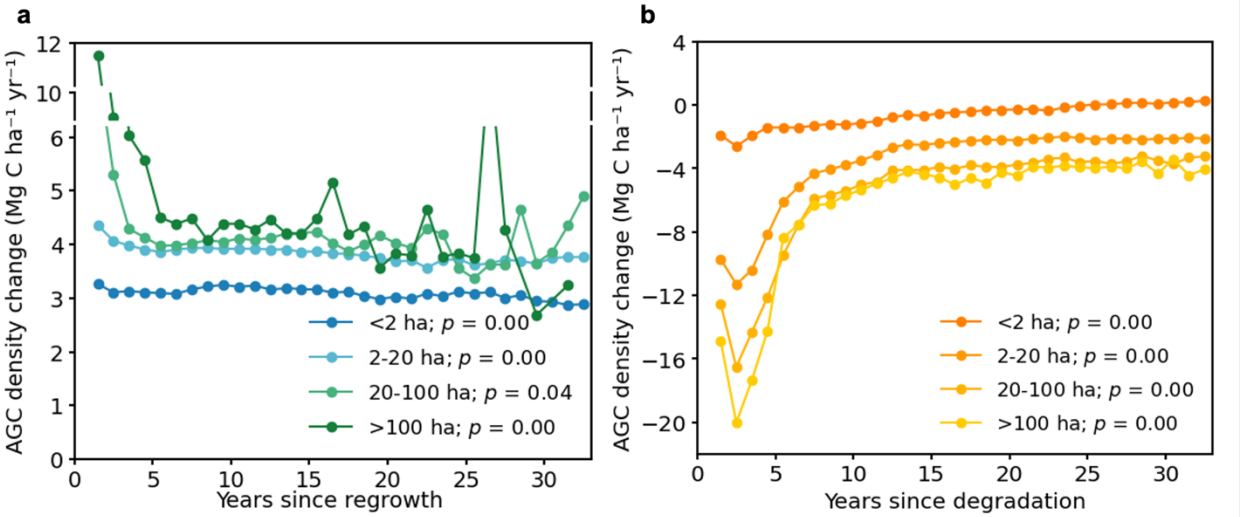



**Supplementary Fig. 34: Changes in aboveground carbon (AGC) density from deforestation across different patch sizes in the Amazon, with edge pixels excluded.** '1-pixel edge removed' indicates that the outermost one-pixel boundary was excluded; the same applies for three-pixel and five-pixel removals.

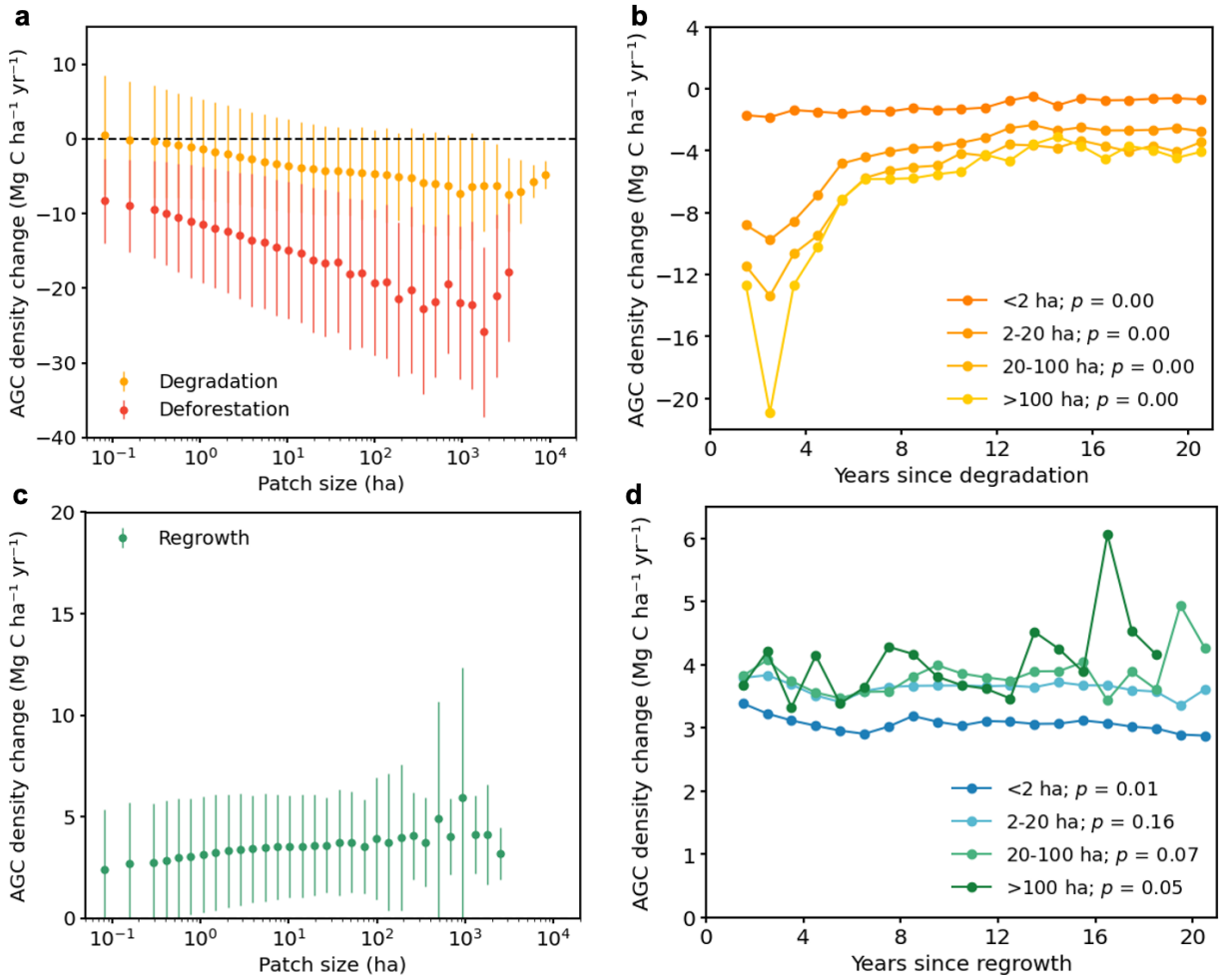



869

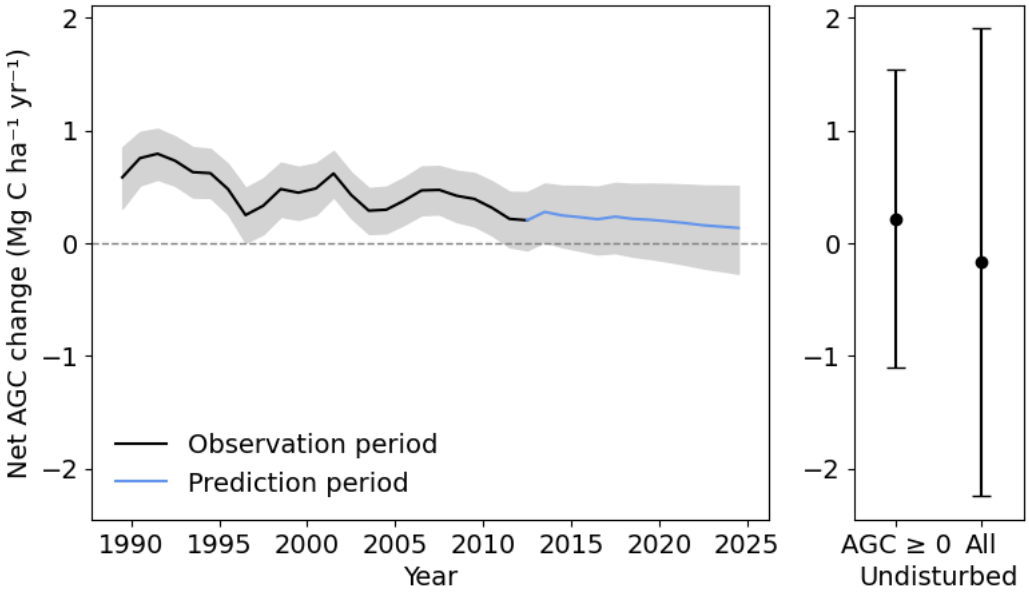
870 **Supplementary Fig. 35:** Comparisons of aboveground carbon (AGC) density regrowth rates in
871 regrowth forests across different land-use types. **a,** AGC density regrowth rates in plantation,
872 afforestation, and other regrowth areas. **b,** Proportions of mining, protected areas, and their overlap
873 within plantation and afforestation areas. **c,** AGC density regrowth rates in burned and non-burned
874 (other) areas. The plantation and afforestation maps are extracted from the Tropical Moist Forests
875 (TMF )map[72], and the burned area map (2014–2018) is derived from the 30 m Global Annual
876 Burned Area Maps (GABAM)[69]. The boundaries of protected areas and mining concessions were
877 obtained from the World Database on Protected Areas (WDPA) [73] and Global Forest Watch
878 (https://data.globalforestwatch.org/).



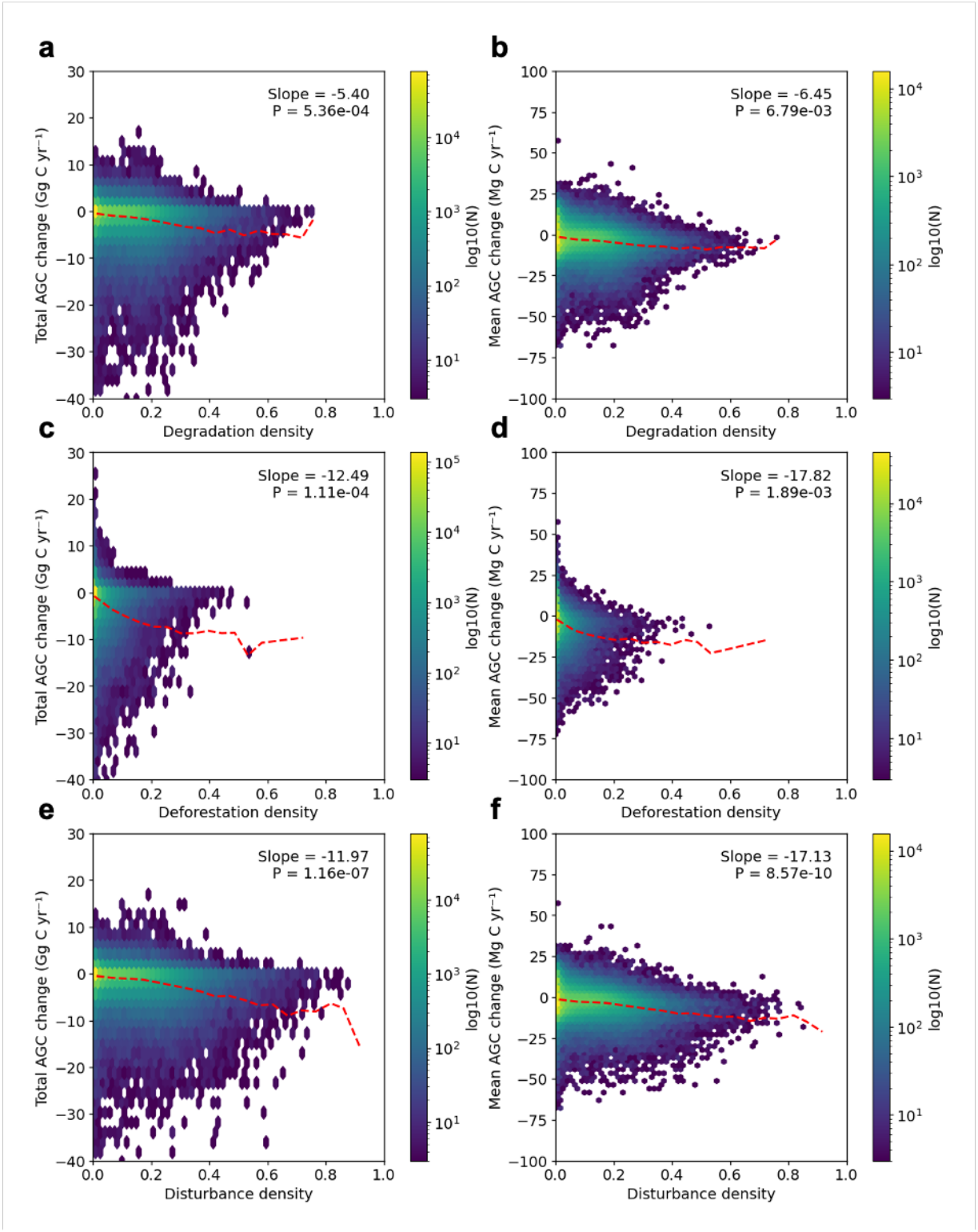

**Supplementary Fig. 36: Aboveground carbon (AGC) density change (2019 to 2022) across long-term (1990–2022) disturbance years. a, b,** AGC density change across patch sizes over regrowth years (**a**) and degradation years (**b**). Mean values and trend lines (slope and *p*) are shown. Long-term records (1990–2022) of degradation and regrowth events are from the Tropical Moist Forests dataset.




**Supplementary Fig. 37: Distribution of aboveground carbon (AGC) density change (2019 to 2022) by patch size and disturbance years within the Amazon protected area. a, c,** AGC density change associated with forest regrowth (**a**) and degradation and deforestation (**c**) across different patch size bins. For each patch size bin, the mean ± standard deviation is shown. Patch sizes were derived from canopy height change maps specific to each disturbance class. **b, d,** AGC density change across patch sizes over regrowth years (**b**) and degradation years (**d**). Mean values and trend lines (slope and *p*) are shown. Long-term records of degradation and regrowth events, extending up to 21 years before the observation period, are from the Tropical Moist Forests dataset.

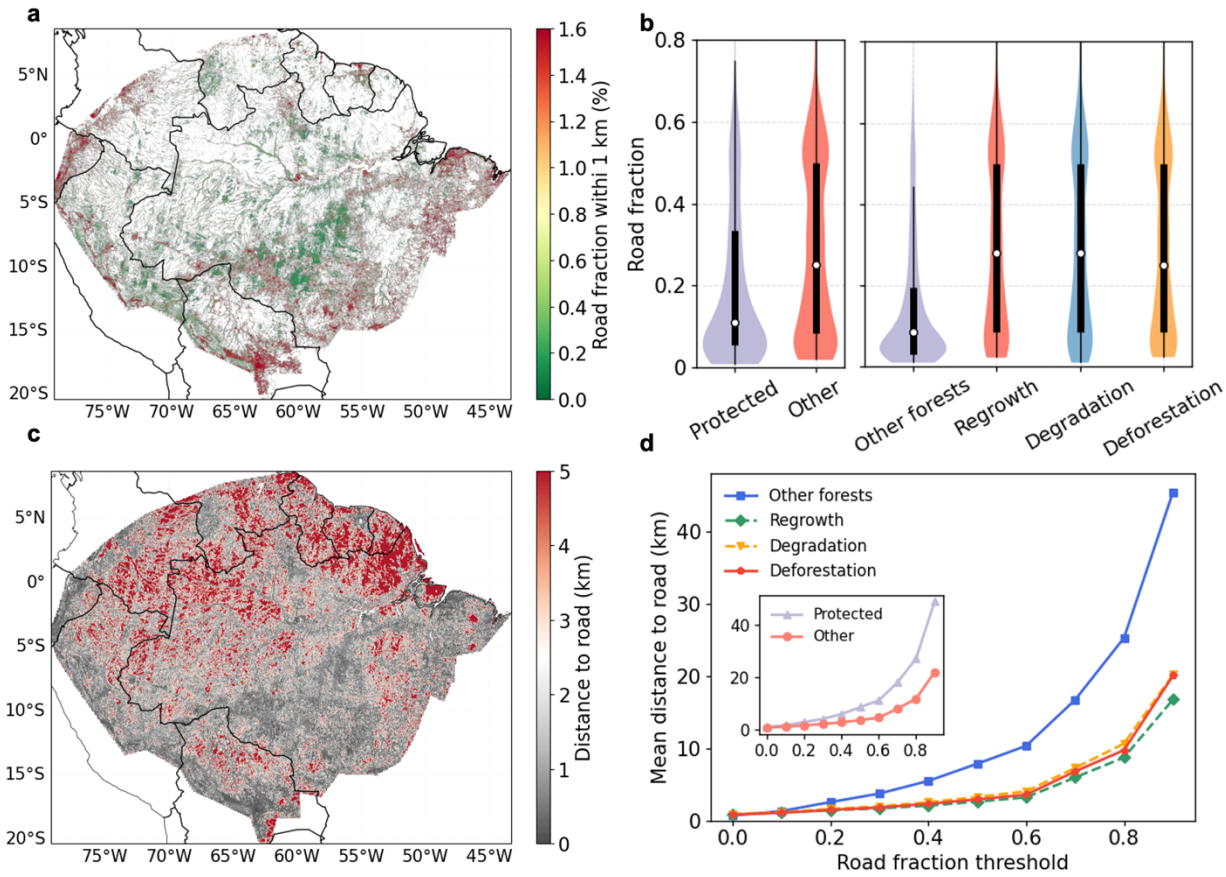



**Supplementary Fig. 38: Comparison of mean net aboveground carbon change (AGC) in undisturbed forests.** The left panel shows the modelled net AGC change across the Amazon derived from field inventory data[55], while the right panel shows the mean AGC change estimated from all undisturbed forest pixels as well as from those with AGC ≥ 0. The extent of undisturbed (old-growth) forests was delineated from the Tropical Moist Forests (TMF) dataset [25].

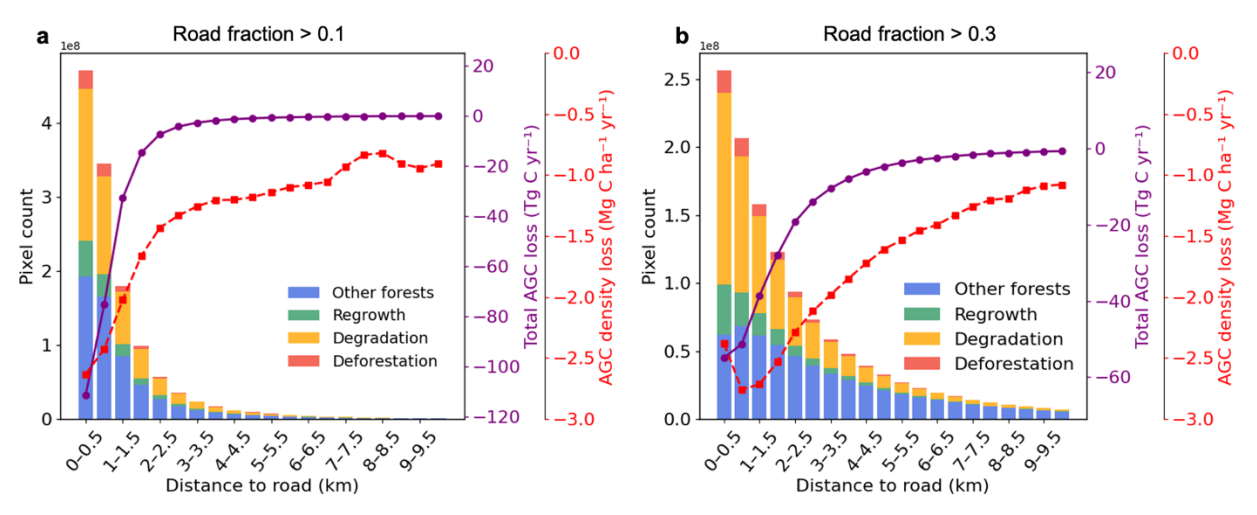



**Supplementary Fig. 39: Relationships between forest disturbance density and aboveground carbon change across 5-km grid cells in the Amazon.** Hexagonal binning plots showing the relationships between degradation density (**a, b**), deforestation density (**c, d**), and total disturbance density (**e, f**) with total aboveground carbon (AGC) change (**a, c, e**) and mean AGC change (**b, d, f**) across 5-km grid cells. Disturbance density was defined as the proportion of 30-m pixels

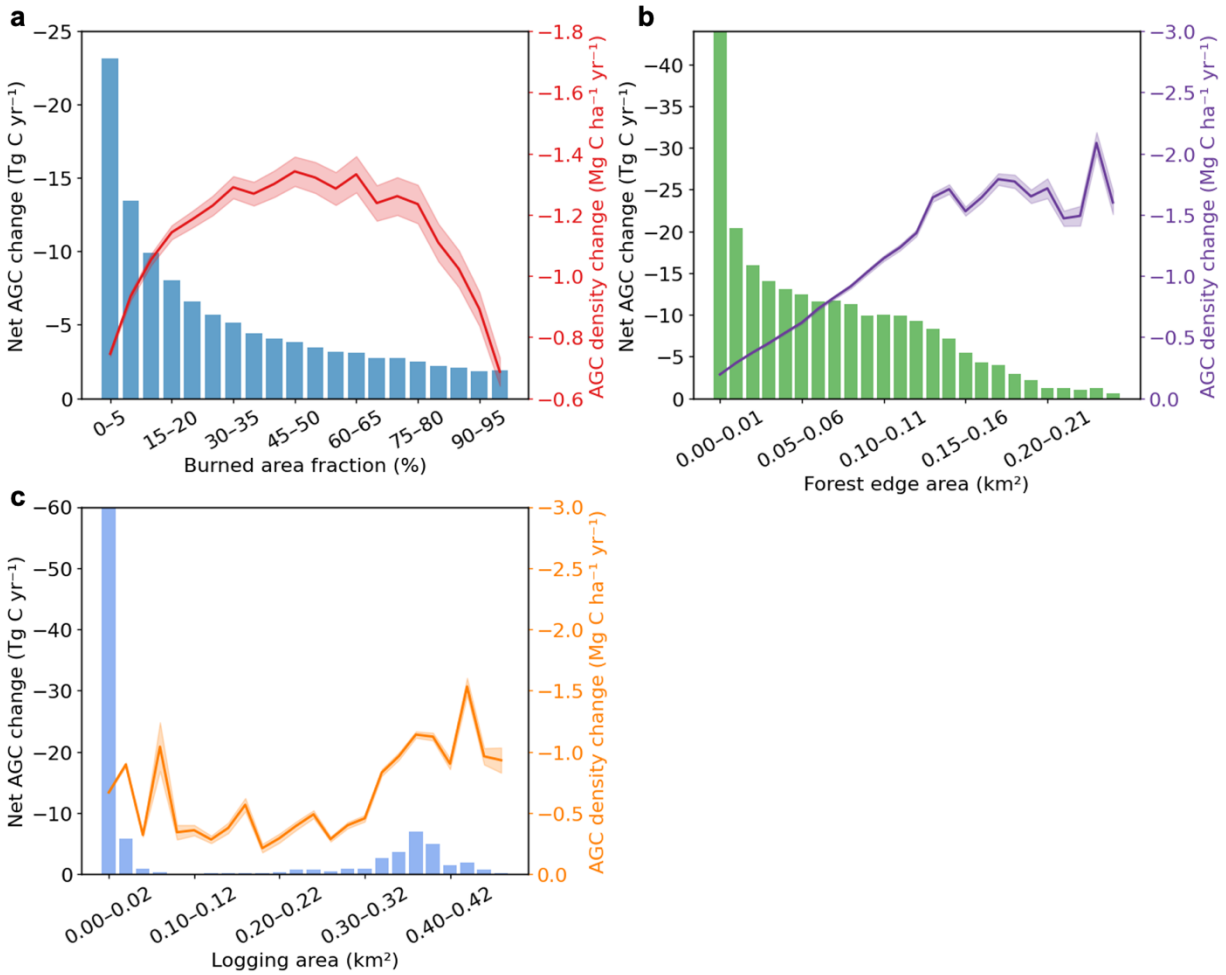
classified as the corresponding disturbance type within each 5-km grid cell. Colors indicate the logarithm of the number of observations within each hexagonal bin. Red dashed lines represent median AGC responses calculated from quantile-based disturbance density bins. Reported slopes and *P* values were derived from linear regression of the binned median responses.



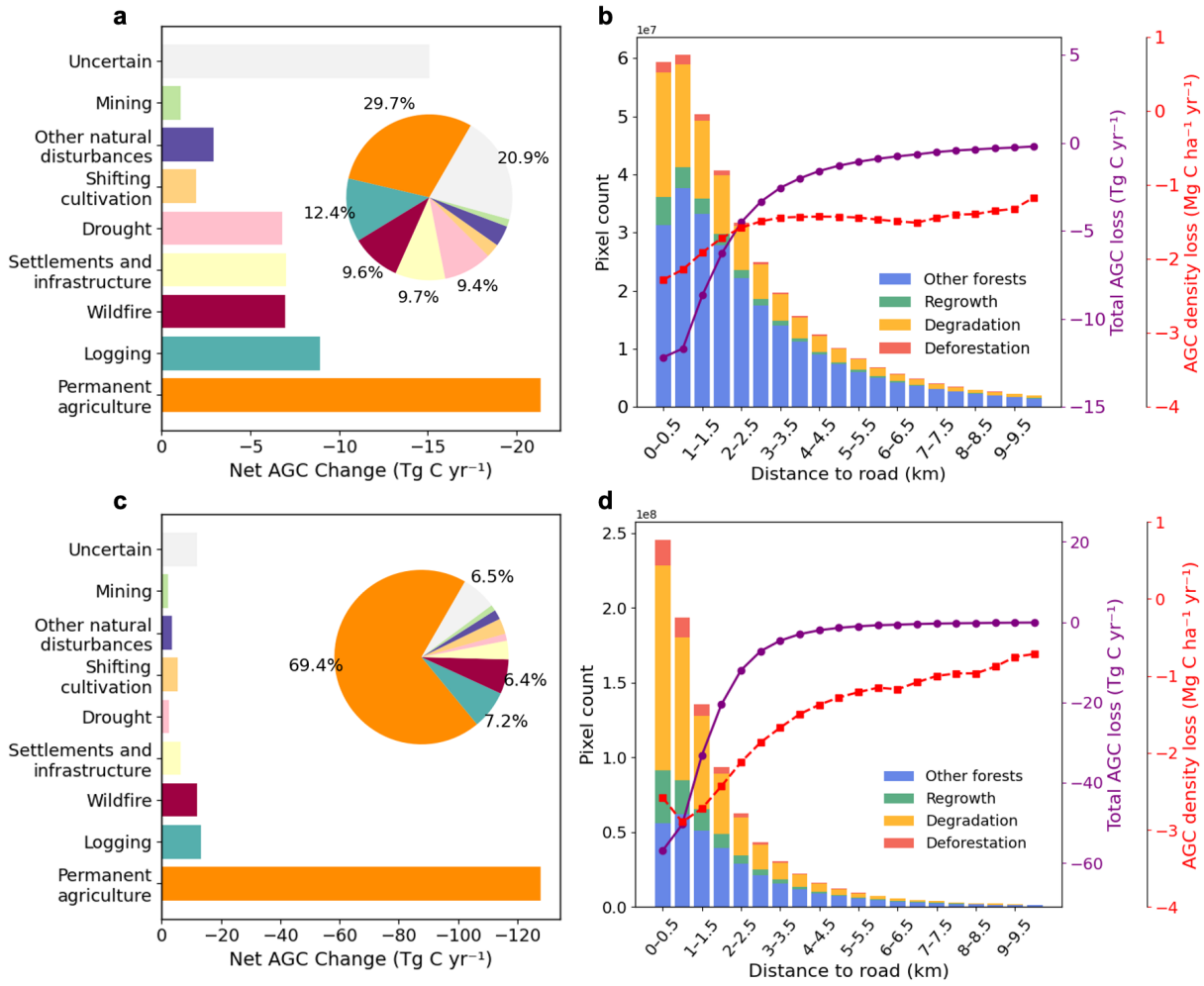

**Supplementary Fig. 40: Distribution of road fraction and distance to roads in the Amazon. a,** Road fraction within 1-km grid cells, averaged from 30-m resolution data. **b,** Comparisons of road fraction across protection status and disturbance types. 'other' indicates the non-protected region. "Other forests" indicate forest areas with small canopy height (CH) changes (≤ 5 m) and no associated TMF disturbances, representing forest dynamics that are not captured by existing disturbance datasets. **c,** Distance to roads, averaged within 5-km grid cells. **d,** Comparisons of mean distance to roads across protection status and disturbance types. The distance to roads was calculated based on the distance from non-road pixels to different thresholds of road fraction.



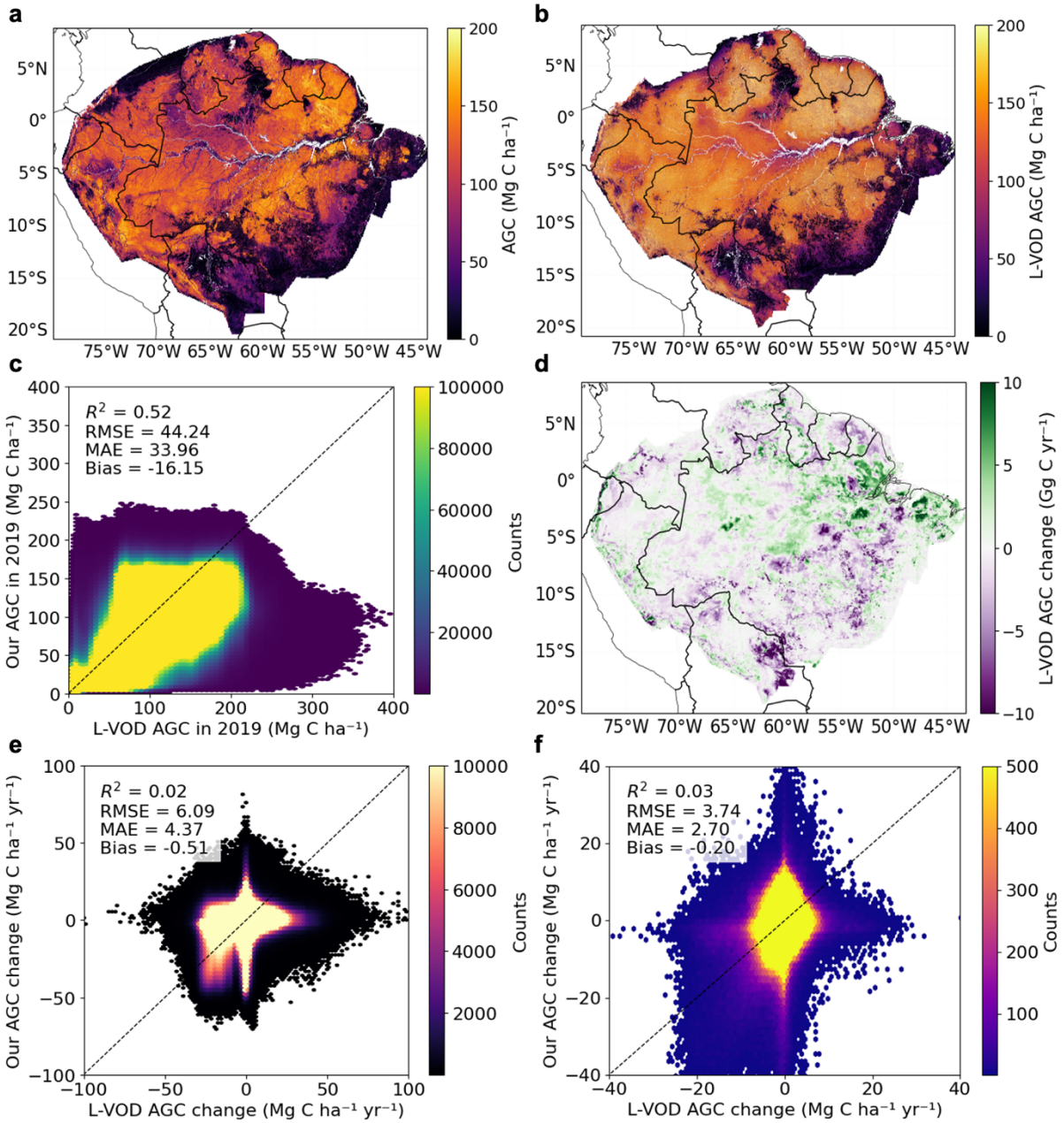

**Supplementary Fig. 41: Relationship between distance to roads and aboveground carbon change in Amazonian forests.** Distances were calculated from all pixels with valid AGC change to the nearest road pixel (road fraction >0.1 in **a**; >0.3 in **b**) at 30-m resolution, for other forests, regrowth, degraded, and deforested areas.



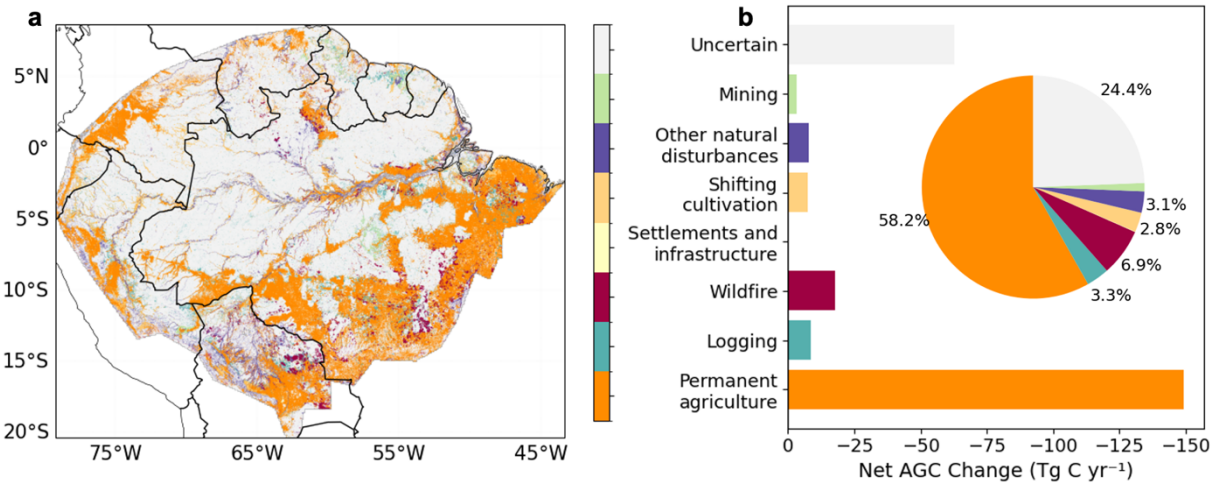

**Supplementary Fig. 42: Aboveground carbon (AGC) loss increases with fire intensity, logging area, and forest edge area. a**, Net AGC change (bars, Tg C $yr^{-1}$) and mean AGC density change (line, Mg C $ha^{-1}$ $yr^{-1}$) across burned area fractions. The burned area map (2014–2018) is derived from the 30 m Global Annual Burned Area Maps (GABAM) [69]. **b, c,** Net AGC change and mean AGC density change across forest edge (**b**) and logging (**c**) areas. Shaded bands represent 95% confidence intervals. Forest edge and logging are the primary drivers of forest degradation in the Amazon[71]. All analyses were conducted at a 1-km grid resolution.




**Supplementary Fig. 43: Contributions of loss drivers and road impacts on aboveground carbon change (AGC) within protected and non-protected areas in the Amazon. a, c,** Contributions of different disturbance drivers to net AGC change during 2019–2022 within protected **(a)** and non-protected (**c**) areas. The loss driver was derived from an updated dataset integrating 1-km forest loss drivers, 30-m Landsat-based burned area data, 5-m road data, and an Amazon forest degradation driver map. Only contributions above 5% are shown. **b, d,** Relationships between distance to roads and AGC change for other forests, regrowth, degraded, and deforested areas within protected **(c)** and non-protected (**d**) areas. Distances were calculated from each pixel with valid AGC change values to the nearest road pixel with a road fraction above 0.2 at 30-m resolution.




**Supplementary Fig. 44: Comparison of estimated aboveground carbon (AGC) with L-band Vegetation Optical Depth (L-VOD) AGC and their changes in the Amazon. a, b,** Maps of our estimated AGC (**a**) and L-VOD-derived AGC (**b**) in 2019 at 100-m resolution. Our AGC was aggregated from 30-m to 100-m resolution. **c,** Relationship between our AGC and L-VOD AGC in 2019. **d,** Map of L-VOD AGC change from 2017 to 2020, averaged at 5-km resolution. **e, f,** Comparisons of AGC changes from our estimates (2019–2022) and L-VOD AGC (2017–2020) at 100-m (**e**) and 1-km (**f**) scales. Note that L-VOD AGC change is not available for the 2019–2022 period.




**Supplementary Fig. 45: Contributions of loss drivers on aboveground carbon change (AGC) across the Amazon forests. a,** Spatial distribution of forest loss drivers at 1-km resolution across the Amazon forests. The loss driver was derived from the original WRI 1-km forest loss driver data [56]. **b,** Contributions of different disturbance drivers to net AGC change during 2019–2022. Only contributions above 2% are shown.

968 **Supplementary Table 1– Table 14**

969

970 **Supplementary Table 1**: **Summary of canopy height (CH) and aboveground biomass (AGB)**
971 **datasets across the Amazon.** S1/S2: Sentinel-1/-2; WD: wood density; SRTM: Shuttle Radar
972 Topography Mission; TRMM: Tropical Rainfall Measuring Mission; QSCAT: global quick
973 scatterometer; ALS: airborne laser scanning; BRT: bagged regression tree; GHM: Generalized
974 hierarchical model; CNN: convolutional neural network; RF: random forest; OLS: ordinary least
975 squares; SWR: stepwise regression. Note that only our study and ESA CCI include the annual data
976 in different years. The original L-VOD data only provides the aboveground carbon map, which is
977 converted to the AGB map by dividing by a factor of 0.5[74].

| Name (Reference) | Data | Resolution | Mapping year | Model | Input data |
|---|---|---|---|---|---|
| This study | CH, AGB | 10 m, 30 m | 2019–2022 (annual) | U-Net; Allometric | S1, S2, GEDI; WD |
| GLAD [75] | CH | 30 m | 2019 | BRT | Landsat, GEDI |
| GTDX [62,76] | CH, AGB | 25 m | 2011–2021 | GHM | TanDEM-XInSAR, GEDI |
| ETH [77] | CH | 10 m | 2020 | CNN | S2, GEDI |
| Pauls, et al. [9] | CH | 10 m | 2020 | U-Net | S1, S2, GEDI |
| CTrees [16] | CH | ~4.78 m | 2020–2024 | U-Net | Planet NICFI, ALS |
| Meta [17] | CH | 1 m | 2009–2020 | DINOv2 | WorldView, Quickbird II, ALS |
| EBA [11] | AGB | 250 m | 2016 | Allometric, RF | ALS, PALSAR, MODIS, SRTM, TRMM |
| ESACCI AGB [60] | AGB | 100 m | 2007,2010, 2015–2022 | Allometric | SAR C-band, L-band |
| GEDI L4B [61] | AGB | 1 km | 2019–2023 | OLS | GEDI |

| | | | | | |
|---|---|---|---|---|---|
| Saatchi [27] | AGB | 100 m | 2020 | MaxEnt model, machine learning | ICESat-1, Landsat8, PALSAR, ALS, Land cover, SRTM, MODIS, |
| L-VOD [74] | AGB | 100 m | 2010–2020 | Constrained statistical disaggregation | L-band passive microwave data of (SMOS) satellite |
| GlobBiomass [63] | AGB | 100 m, 25 m | 2007–2008 | Allometric | SAR, auxiliary data ICESat, Landsat, |
| Baccini AGB [64] | AGB | 500 m | 2000s | Allometric, SWR, RF | ICESat, MODIS |
| Saatchi, et al. [26] | AGB | 1 km | 2000s | MaxEnt model | ICESat, MODIS, QSCAT, SRTM |
| Avitabile, et al. [65] | AGB | 1 km | 2000s | Data fusion | Baccini and Saatchi AGB |

978

**Supplementary Table 2**: **Summary of reference datasets used to evaluate and interpret canopy height (CH) changes from 2019 to 2022 in the Amazon.** GEDI RH100 was directly used to assess CH changes in the same region and period, while the other three disturbance datasets were used to filter unlikely CH changes and validate CH loss events.

| Dataset | Time | Band (mask condition) | GEE source |
|---|---|---|---|
| GEDI L2A RH100 | 2019, 2022 | 'rh100': (1) degrade_flag = 0, quality_flag = 1; (2) sensitivity (0.98–1); (3) rh100 > 0; (4) leaf_off_flag = 0; (5) landsat_water_persistence < 10; (6) urban_proportion ≤ 50; (7) pft_mask equal to 1–6 or 11 | 'LARSE/GEDI/GEDI02_A_002_MONTHLY' |
| Tropical Moist Forest (TMF) [25] | 2019–2022 | 'Undisturbed', 'regrowth', 'degradation', 'deforestation', 'other land cover' | 'projects/JRC/TMF/v1_2024/AnnualChanges' |
| Global Forest Change (GFC) [34] | 2019–2022 | 'lossyear' | 'UMD/hansen/global_forest_change_2023_v1_11' |
| radar-based RAdar for Detecting Deforestation (RADD) [5] | 2020–2022 | 'Alert', 'Date' (high confidence: pixel value = 3) | projects/radar-wur/raddalert/v1 |

**Supplementary Table 3: Visual validation of canopy height (CH) loss and gain detections, and estimation of false detection rates using visually confirmed stable forest areas from 5-m PlanetScope imagery.** Area (%) represents the proportion of each patch size class relative to the total mapped area of 0–100 ha patches. Visual interpretation of very small **CH** changes remains challenging, and subtle gain or loss signals may be visually indistinguishable from stable forest conditions, potentially leading to underestimated accuracies for small patches.

| Patch size | Type | Area (%) | Sample size | Mean CH change (m) | TP | FP | UA |
|---|---|---|---|---|---|---|---|
| 0–2 ha | Loss | 28.8% | 200 | –1.5 | 133 | 67 | 66.5% |
| 2–10 ha | Loss | 37.2% | 191 | –1.5 | 143 | 48 | 74.9% |
| 10–100 ha | Loss | 34.0% | 190 | –1.9 | 159 | 31 | 83.7% |
| | Area-weighted user's accuracy (UA) for loss (0–100 ha) | | | | | | 75.5% |
| 0–2 ha | Gain | 47.4% | 200 | 2.1 | 131 | 69 | 65.5% |
| 2–10 ha | Gain | 33.2% | 180 | 2.1 | 136 | 44 | 75.6% |
| 10–100 ha | Gain | 19.4% | 142 | 2.0 | 120 | 22 | 84.5% |
| | Area-weighted user's accuracy (UA) for gain (0–100 ha) | | | | | | 72.5% |

**Supplementary Table 4: Visual validation of canopy-height (CH) loss detections stratified by mean CH-loss magnitude using randomly sampled 2-ha and 5-ha image chips interpreted from 5-m PlanetScope imagery.** The 2-ha and 5-ha categories refer to the size of randomly sampled image chips extracted from the CH-change map rather than the size of individual CH-loss patches. Image chips were stratified according to the mean estimated canopy-height loss within each chip. Visual interpretation using 5-m Planet imagery was used only to determine whether canopy loss was present (true positive) or absent (false positive); it does not provide an independent assessment of the quantitative accuracy of canopy-height loss magnitude estimates.

| Random image-chip size | CH loss magnitude (m) | Sample number | TP | FP | UA |
|---|---|---|---|---|---|
| 2 ha | $-2 \leq \Delta CH < 0$ | 100 | 62 | 38 | 62.00% |
| | $-5 \leq \Delta CH < -2$ | 106 | 72 | 34 | 67.92% |
| | $-10 \leq \Delta CH < -5$ | 127 | 98 | 29 | 77.17% |
| | $-15 \leq \Delta CH < -10$ | 128 | 111 | 17 | 86.72% |
| 5 ha | $-2 \leq \Delta CH < 0$ | 102 | 65 | 37 | 63.73% |
| | $-5 \leq \Delta CH < -2$ | 109 | 72 | 37 | 66.06% |
| | $-10 \leq \Delta CH < -5$ | 149 | 120 | 29 | 80.54% |
| | $-15 \leq \Delta CH < -10$ | 146 | 129 | 17 | 88.36% |

**Supplementary Table 5: Proportion of validated canopy height losses and their detection by conventional forest disturbance products.** PlanetScope-confirmed canopy height (CH) loss patches and magnitude indicate disturbances visually identified from PlanetScope imagery across different patch-size and loss magnitude classes. Across different CH loss classes, detection rates were calculated considering only TMF, GFC and RADD disturbance patches containing at least three disturbed pixels. ALS-confirmed CH loss pixels indicate locations where both satellite-derived CH changes and repeat airborne laser scanning (ALS) measurements showed CH loss in the Caxiuanã[78,79] (CAX) and Jamari[80,81] National Forest (JAM) sites. Values represent the proportion of confirmed canopy height losses that were additionally detected by the TMF, GFC and RADD disturbance products across different canopy height loss magnitude classes.

| Data | Size class | Sample size | TMF | GFC | RADD |
|---|---|---|---|---|---|
| Confirmed CH loss patches from PlanetScope images | 0–2 ha | 133 | 28.6% | 11.3% | 6.0% |
| | 2–10 ha | 143 | 52.5% | 31.2% | 9.9% |
| | 10–100 ha | 159 | 88.0% | 70.4% | 52.2% |
| Confirmed CH loss magnitude from PlanetScope images (**2-ha image chips**) | $-2 \leq \Delta CH < 0$ | 62 | 21.0% | 3.2% | 0.0% |
| | $-5 \leq \Delta CH < -2$ | 72 | 23.6% | 15.3% | 6.9% |
| | $-10 \leq \Delta CH < -5$ | 98 | 64.3% | 56.1% | 35.7% |
| | $-15 \leq \Delta CH < -10$ | 111 | 84.7% | 87.4% | 64.0% |
| Confirmed CH loss magnitude from PlanetScope images (**5-ha image chips**) | $-2 \leq \Delta CH < 0$ | 65 | 18.5% | 3.1% | 1.5% |
| | $-5 \leq \Delta CH < -2$ | 72 | 44.4% | 30.6% | 9.7% |
| | $-10 \leq \Delta CH < -5$ | 120 | 68.3% | 66.2% | 44.2% |
| | $-15 \leq \Delta CH < -10$ | 129 | 87.6% | 86.8% | 75.2% |
| Confirmed CH loss pixels by ALS data (JAM, CAX) | $\Delta CH < 0$ | 620 | 2.6% | 1.1% | 0% |
| | $-5 \leq \Delta CH < 0$ | 605 | 1.7% | 0.3% | 0% |
| | $\Delta CH < -5$ | 15 | 40.0% | 33.3% | 0% |

**Supplementary Table 6: Summary of above-ground carbon changes across the Amazon and its protected area.** Disturbance types were identified from canopy height change data, multiple reference datasets and a machine-learning classification of canopy height change, which differs from the Tropical Moist Forest classification map. Units of above-ground carbon (AGC) and area change areTg C $yr^{-1}$ and Mha, respectively.

| | | All | | Protected area | |
|---|---|---|---|---|---|
| | | AGC | Area | AGC | Area |
| Loss | Other | −153.9 ± 25.4 | −38.6 ± 6.0 | −77.3 ± 12.8 | −19.3 ± 3.0 |
| | Deforestation | −92.9 ± 14.9 | −5.4 ± 0.9 | −15.6 ± 2.5 | −1.0 ± 0.2 |
| | Degradation | −189.8 ± 30.6 | −38.6 ± 6.1 | −47.6 ± 7.7 | −9.0 ± 1.4 |
| | Total | −436.6 ± 42.4 | −82.5 ± 8.6 | −140.5 ± 15.1 | −29.2 ± 3.3 |
| Gain | Other | 83.7 ± 14.7 | 14.6 ± 2.4 | 46.1 ± 8.1 | 7.9 ± 1.3 |
| | Degradation | 58.5 ± 12.1 | 8.5 ± 1.7 | 15.8 ± 3.3 | 1.8 ± 0.4 |
| | Secondary | 37.7 ± 6.7 | 10.7 ± 1.9 | 6.6 ± 1.2 | 2.1 ± 0.4 |
| | Total | 179.8 ± 20.1 | 33.8 ± 3.5 | 68.4 ± 8.8 | 11.8 ± 1.4 |
| Net (total area) | | −256.7 ± 47.0 | 116.3 ± 9.3 | −72.0 ± 17.5 | 41.0 ± 3.6 |

**Supplementary Table 7**: Summary of aboveground carbon (AGC) change across primary protected types. The table presents the total AGC change, AGC density change, and the corresponding area for each category.

| Protected type | Total AGC change (Tg C $yr^{-1}$) | AGC density change (only changed pixels) (Mg C $ha^{-1}$ $yr^{-1}$) | Area (only changed pixels) (Mha) | AGC density change (all pixels) (Mg C $ha^{-1}$ $yr^{-1}$) | Area (all pixels) (Mha) |
|---|---|---|---|---|---|
| Indigenous land | −15.6 | −1.12 | 13.8 | −0.15 | 101.5 |
| Environmental Protection | −8.7 | −2.94 | 3.0 | −0.62 | 14.1 |
| National Park | −7.1 | −2.07 | 3.4 | −0.25 | 27.8 |
| Extractive Reserve | −6.5 | −3.27 | 2.0 | −0.52 | 12.3 |
| Forest | −5.5 | −1.64 | 3.3 | −0.19 | 28.3 |
| Ramsar Site | −4.5 | −1.49 | 3.0 | −0.24 | 18.8 |
| Park | −3.6 | −1.42 | 2.5 | −0.18 | 20.0 |
| Ecological Station | −3.1 | −2.15 | 1.4 | −0.28 | 10.8 |
| Biosphere Reserve | −2.6 | −2.32 | 1.1 | −0.34 | 7.6 |
| Sustainable Development Reserve | −2.5 | −1.92 | 1.3 | −0.27 | 9.5 |

**Supplementary Table 8**: Summary of aboveground carbon (AGC) change across different IUCN protected area categories. The table presents the total AGC change, AGC density change, and the corresponding area for each category.

| IUCN | Total AGC change (Tg C $yr^{-1}$) | AGC density change (only changed pixels) (Mg C $ha^{-1}$ $yr^{-1}$) | Area (only changed pixels) (Mha) | AGC density change (all pixels) (Mg C $ha^{-1}$ $yr^{-1}$) | Area (all pixels) (Mha) |
|---|---|---|---|---|---|
| Ia | −4.6 | −2.18 | 2.1 | −0.27 | 16.9 |
| Ib | −0.01 | −0.28 | 0.02 | −0.03 | 0.2 |
| II | −9.6 | −1.65 | 5.8 | −0.18 | 52.8 |
| III | −0.1 | −0.43 | 0.2 | −0.01 | 6.7 |
| IV | −0.2 | −0.89 | 0.2 | −0.17 | 1.0 |
| V | −8.6 | −3.25 | 3.3 | −0.51 | 16.8 |
| VI | −20.5 | −1.91 | 10.7 | −0.25 | 82.8 |
| Not Reported | −26 | −1.48 | 17.5 | −0.22 | 118.6 |
| Not Assigned | −0.1 | −1.26 | 0.1 | −0.17 | 0.5 |
| Not Applicable | −2.6 | −2.33 | 1.1 | −0.34 | 7.6 |
| **All region** | | | | | |
| All non-protected areas | −184.6 | −2.45 | 75.3 | −0.43 | 430.8 |
| All areas | −256.7 | −2.21 | 116.3 | −0.35 | 734.8 |

**Supplementary Table 9: Summary of above-ground carbon changes across different forest types in the Amazon.** Forest types are derived from the MapBiomas land cover and land-use data[68]. Disturbance types were identified from canopy height change data, multiple reference datasets and a machine-learning classification of canopy height change, which differs from the Tropical Moist Forest classification map.

| | | AGC change (Tg C $yr^{-1}$) | | | |
|---|---|---|---|---|---|
| | | Forest formation | Flooded forest | Mangrove | Savanna formation |
| Loss | Other | −271.4 | −60.6 | −1.0 | 0.0 |
| | Deforestation | −15.7 | −7.1 | −0.1 | −0.5 |
| | Degradation | −177.7 | −46.0 | −0.4 | −3.1 |
| | Total | −464.8 | −113.7 | −1.6 | −3.6 |
| Gain | Other | 163.8 | 18.2 | 0.2 | 0.0 |
| | Degradation | 70.6 | 13.5 | 0.2 | 2.4 |
| | Secondary | 43.1 | 11.0 | 0.1 | 1.6 |
| | Total | 277.5 | 42.6 | 0.6 | 4.1 |
| Net | | −187.4 | −71.1 | -1.0 | 0.5 |

**Supplementary Table 10: Comparisons of our estimated aboveground carbon (AGC) change with estimates derived from remote sensing observations, process-based models, bottom-up flux estimates, and hybrid approaches.** Negative values indicate forest biomass loss and associated carbon emissions to the atmosphere. Estimates presented here are not directly comparable due to methodological differences. Our estimate reflects changes in aboveground biomass carbon (AGC, Tg C $yr^{-1}$) only, including the results from Fawcett, et al. [82] and Fendrich, et al. [42]. While Inversion-based estimates represent net ecosystem carbon exchange and integrate multiple flux pathways not captured by structural biomass observations, including additional fluxes such as belowground biomass, soil carbon, fire emissions, and legacy fluxes. Therefore, this table provides a reference comparison, but the values should not be interpreted as fully equivalent across approaches.

| Data variable | Net carbon change | Time | Reference |
|---|---|---|---|
| Our AGC | −256.7 ± 47.0 | 2019–2022 | |
| L-VOD AGC (25 km) | −188.9 ± 58.6 | 2012–2019 | Fawcett, et al. [82] |
| Downscaled L-VOD AGC (100 m) | −166 | 2012–2019 | Fendrich, et al. [42] |
| Old-growth forest sink (TRENDY-v11) | 333 (± 195) | 2010–2020 | Rosan, et al. [40] |
| Net land carbon fluxes (Bottom-up) | 141 (± 195) | 2010–2020 | |
| Net land carbon fluxes (Hybrid) | 243 (± 195) | 2010–2020 | |
| Disturbances bottom-up (BLUE ELUC + FATE degradation fires) | −192 | 2010–2020 | |
| Disturbances hybrid (GFED deforestation and degradation fires) | −89 | 2010–2020 | |
| Posterior total flux (with Amazon observations) | −130 (± 170) | 2010–2018 | Basso, et al. [37] |
| Posterior total flux (without Amazon observations) | −480 (± 170) | 2010–2018 | |
| Total carbon balance | −290 (± 400) | 2010–2018 | Gatti, et al. [38] |
| Amazonia carbon emissions | −240 (± 80) | 2010–2018 | Gatti, et al. [39] |
| | −440 (± 100) | 2019 | |
| | −520 (± 100) | 2020 | |

**Supplementary Table 11. Contributions of disturbance patch-size classes and canopy-height (CH) change classes to affected area and aboveground carbon (AGC) change associated with mapped forest loss and gain.** Area is expressed in Mha and AGC change in Tg C $yr^{-1}$. Percentages for forest loss and forest gain were calculated separately relative to the total affected area and total AGC change within the corresponding loss or gain category. Values are rounded to one decimal place

| Type | Patch size (ha) | Area (Mha) | Area (%) | AGC change (Tg C $yr^{-1}$) | AGC change (%) |
|---|---|---|---|---|---|
| **Loss** | 0–2 ha | 17.4 | 21.1 | −52.5 | 12.0 |
| | 2–10 ha | 22.5 | 27.2 | −83.2 | 19.1 |
| | 10–100 ha | 20.5 | 24.9 | −109.0 | 25.0 |
| | >100 ha | 22.1 | 26.8 | −191.8 | 43.9 |
| **Gain** | 0–2 ha | 14.8 | 43.9 | 76.7 | 42.7 |
| | 2–10 ha | 10.4 | 30.8 | 53.4 | 29.7 |
| | 10–100 ha | 6.1 | 18.0 | 32.6 | 18.2 |
| | >100 ha | 2.5 | 7.4 | 17.0 | 9.5 |
| | CH change ($\Delta CH$, m) | Area (Mha) | Area (%) | AGC change (Tg C $yr^{-1}$) | AGC change (%) |
| **Loss** | $-2 \leq \Delta CH < 0$ | 43.7 | 52.9 | −84.2 | 19.3 |
| | $-5 \leq \Delta CH < -2$ | 26.7 | 32.3 | −151.0 | 34.6 |
| | $-10 \leq \Delta CH < -5$ | 7.5 | 9.1 | −80.0 | 18.3 |
| | $-15 \leq \Delta CH < -10$ | 2.2 | 2.7 | −41.3 | 9.5 |
| | $\Delta CH < -15$ | 2.5 | 3.0 | −80.1 | 18.4 |
| **Gain** | $0 < \Delta CH \leq 2$ | 12.4 | 36.7 | 28.1 | 15.6 |
| | $2 < \Delta CH \leq 5$ | 17.0 | 50.4 | 101.3 | 56.3 |
| | $5 < \Delta CH \leq 10$ | 3.9 | 11.6 | 41.6 | 23.1 |
| | $\Delta CH > 10$ | 0.4 | 1.3 | 8.8 | 4.9 |

**Supplementary Table 12**: **Comparisons of our estimated aboveground carbon change with prior work.** Primary forests indicate old growth forests or undisturbed forests. The undisturbed forests for our AGC change were defined using the Tropical Moist Forests (TMF) data.

| Our map (2019–2022, Amazon forests) | Reference |
|---|---|
| AGC density loss rate: degraded and deforested forests (−19.3 Mg C $ha^{-1}$); only defrosted forests (−51.5 Mg C $ha^{-1}$); only degraded forests (−14.8 Mg C $ha^{-1}$) | GEDI-derived results for degraded forests (−23.1 Mg C $ha^{-1}$; Amazon) [46]; Average deficit of degraded forests (−21.8 Mg C $ha^{-1}$; TMF) compared to nearby interior forest[83] |
| AGC density gain rate for regrowth forests (3.5 Mg C $ha^{-1}$ $yr^{-1}$) | LiDAR-derived growth (3.8 Mg C $ha^{-1}$ $yr^{-1}$) reported in Amazon forests[47]; ESA-CCI derived secondary forest regrowth (1.3–3.2 Mg C $ha^{-1}$ $yr^{-1}$) in the Brazilian Amazon[50]; Field inventory ranges in Amazon tropical rainforests (4.64 Mg C $ha^{-1}$ $yr^{-1}$) and moist forest (3.37 Mg C $ha^{-1}$ $yr^{-1}$)[48], and exceed IPCC defaults for tropical rainforests (2.8 Mg C $ha^{-1}$ $yr^{-1}$) and moist forests (2.4 Mg C $ha^{-1}$ $yr^{-1}$) [48,49]; |
| AGC density change rate for undisturbed forests: all pixels (−0.17 Mg C $ha^{-1}$ $yr^{-1}$); AGC≥ 0 (0.22 Mg C $ha^{-1}$ $yr^{-1}$) | Refined IPCC default AGC change rate for primary forests: tropical moist forests (0.47 Mg C $ha^{-1}$ $yr^{-1}$), tropical rainforests (0.18 Mg C $ha^{-1}$ $yr^{-1}$)[49]; Modelled AGC change rate using field inventory data (0.16 Mg C $ha^{-1}$ $yr^{-1}$ in 2022) [55] |

**Supplementary Table 13: Summary of changes in the number of original and processed CH-loss pixels.** We applied a three-step procedure to filter out noisy CH-loss pixels: (1) the first step excluded isolated pixels; (2) the second step removed loss-related noise; and (3) the final correction, based on canopy cover change, identified pixels with consistent trends. Detailed descriptions are provided in **Methods**, and the corresponding results are shown in **Supplementary Fig. 19**.

| CH loss range | Original CH loss pixels | CH loss pixels after the first step (reduced pixel ratio relative to original) | CH loss pixels after the second step (reduced pixel ratio relative to original) | CH loss pixels after final processing (reduced pixel ratio relative to original) |
|---|---|---|---|---|
| (−2, 0] | 2143491680 | 1773255390 (17.3%) | 849476741 (60.4%) | 485314137 (77.3%) |
| (−4, −2] | 516914693 | 489058002 (5.4%) | 376929140 (27.1%) | 245869998 (52.4%) |
| (−6, −4] | 122396906 | 119412758 (2.4%) | 101485333 (17.1%) | 81382352 (33.7%) |
| (−8, −6] | 43085134 | 42537019 (1.3%) | 37377694 (13.2%) | 33974101 (21.2%) |
| (−10, −8] | 21758320 | 21596730 (0.8%) | 19529087 (10.3%) | 18674752 (14.1%) |
| (−12, 10] | 13337694 | 13268483 (0.5%) | 12423093 (6.9%) | 12140875 (9.0%) |
| (−14, −12] | 9234357 | 9197538 (0.2%) | 8818943 (4.5%) | 8732970 (5.4%) |
| (−16, −14] | 7424958 | 7404319 (0.2%) | 7195935 (3.1%) | 7166046 (3.5%) |
| (−18, −16] | 6390944 | 6378185 (0.2%) | 6258160 (2.1%) | 6245892 (2.3%) |
| (−20, −18] | 5675978 | 5667335 (0.2%) | 5595066 (1.4%) | 5589477 (1.5%) |
| (−22, 20] | 4940730 | 4935176 (0.1%) | 4889810 (1.1%) | 4886914 (1.1%) |
| (−24, −22] | 3782991 | 3780158 (0.1%) | 3755045 (0.7%) | 3753585 (0.7%) |
| (−26, −24] | 2263708 | 2263044 (0.0%) | 2250376 (0.6%) | 2249872 (0.8%) |
| (−28, −26] | 935435 | 935256 (0.0%) | 929447 (0.6%) | 929339 (0.6%) |
| (−30, −28] | 236314 | 236263 (0.0%) | 235894 (0.2%) | 235882 (0.2%) |
| (−32, 30] | 39100 | 39070 (0.1%) | 39010 (0.2%) | 39007 (0.2%) |
| (−34, −32] | 4297 | 4252 (1.0%) | 4234 (1.5%) | 4234 (1.5%) |
| (−36, −34] | 337 | 329 (2.4%) | 323 (4.2%) | 323 (4.2%) |
| (−38, −36] | 12 | 12 (0.0%) | 12 (0.0%) | 12 (0.0%) |
| (−40, −38] | 0 | 0 (—) | 0 (—) | 0 (—) |

**Supplementary Table 14: Summary of classification uncertainty in canopy height loss and gain.** The XGBoost model was trained to classify six different classes based on the previously defined class labels. The weight-average precision and recall was used as the mean accuracy for determining the uncertainty. Input features included CH from 2019 to 2023, ΔCH (2023–2019), ΔCH (2023–2022), ΔCH (2022–2019), and canopy cover change between 2019 and 2022.

| Class | Uncertainty | Precision | Recall | F1-score | Support |
|---|---|---|---|---|---|
| Other (loss) | 11.5% | 0.87 | 0.90 | 0.88 | 80224354 |
| Deforestation | 12.5% | 1.00 | 0.99 | 1.00 | 11579502 |
| Degradation (loss) | 12.5% | 0.90 | 0.86 | 0.88 | 79630076 |
| Secondary (regrowth) | 13.5% | 0.92 | 0.81 | 0.86 | 22814419 |
| Degradation (gain) | 22.5% | 0.75 | 0.80 | 0.77 | 18000770 |
| Other (gain) | 8.0% | 0.90 | 0.94 | 0.92 | 31719992 |

## References


1 Eva, H. D. *et al.* A proposal for defining the geographical boundaries of Amazonia. (2005).

2 Wan, L. *et al.* Satellite-based mapping of annual canopy height and aboveground biomass in African dense forests. *Frontiers in Remote Sensing* **6**, 1724950 (2025).

3 Wan, L. *et al.* Correcting confounding canopy structure, biochemistry and soil background effects improves leaf area index estimates across diverse ecosystems from Sentinel-2 imagery. *Remote Sensing of Environment* **309**, 114224 (2024).

4 Bossy, T. *et al.* State of the art and for remote sensing monitoring of carbon dynamics in African tropical forests. *Frontiers in Remote Sensing* **6**, 1532280 (2025).

5 Reiche, J. *et al.* Forest disturbance alerts for the Congo Basin using Sentinel-1. *Environmental Research Letters* **16**, 024005 (2021).

6 Nandy, S., Srinet, R. & Padalia, H. Mapping forest height and aboveground biomass by integrating ICESat-2, Sentinel-1 and Sentinel-2 data using Random Forest algorithm in

northwest Himalayan foothills of India. *Geophysical Research Letters* **48**, e2021GL093799 (2021).

7 Silveira, E. M. *et al.* Nationwide native forest structure maps for Argentina based on forest inventory data, SAR Sentinel-1 and vegetation metrics from Sentinel-2 imagery. *Remote Sensing of Environment* **285**, 113391 (2023).

8 Qi, W. & Dubayah, R. O. Combining Tandem-X InSAR and simulated GEDI lidar observations for forest structure mapping. *Remote sensing of Environment* **187**, 253-266 (2016).

9 Pauls, J. *et al.* Estimating canopy height at scale. *arXiv preprint arXiv:2406.01076* (2024).

10 Schwartz, M. *et al.* High-resolution canopy height map in the Landes forest (France) based on GEDI, Sentinel-1, and Sentinel-2 data with a deep learning approach. *International Journal of Applied Earth Observation and Geoinformation* **128**, 103711 (2024). https://doi.org:https://doi.org/10.1016/j.jag.2024.103711

11 Ometto, J. P. *et al.* A biomass map of the Brazilian Amazon from multisource remote sensing. *Scientific Data* **10**, 668 (2023).

12 Ometto, J. L3A-Summary of Airborne LiDAR transects collected by EBA in the Brazilian Amazon. *Zenodo https://doi. org/10.5281/zenodo* **4968706** (2021).

13 Reis, C. R. *et al.* Forest disturbance and growth processes are reflected in the geographical distribution of large canopy gaps across the Brazilian Amazon. *Journal of Ecology* **110**, 2971-2983 (2022).

14 Khosravipour, A., Skidmore, A. K., Isenburg, M., Wang, T. & Hussin, Y. A. Generating pit-free canopy height models from airborne lidar. *Photogrammetric Engineering & Remote Sensing* **80**, 863-872 (2014).

15 Dos-Santos, M., Keller, M. & Morton, D. LiDAR surveys over selected forest research sites, Brazilian Amazon, 2008-2018. *ORNL DAAC, Oak RIdge, Tennessee, USA* (2019).

16 Wagner, F. H. *et al.* High Resolution Tree Height Mapping of the Amazon Forest using Planet NICFI Images and LiDAR-Informed U-Net Model. *arXiv preprint arXiv:2501.10600* (2025).

17 Tolan, J. *et al.* Very high resolution canopy height maps from RGB imagery using self-supervised vision transformer and convolutional decoder trained on aerial lidar. *Remote Sensing of Environment* **300**, 113888 (2024).

18 Fischer, F. J. *et al.* A global map of wood density. *bioRxiv*, 2025.2008.2025.671920 (2025). https://doi.org:10.1101/2025.08.25.671920

19 Fischer, F. J. *et al.* Beyond species means – the intraspecific contribution to global wood density variation. *bioRxiv*, 2025.2008.2025.671896 (2025). https://doi.org:10.1101/2025.08.25.671896

20 Longo, M. *et al.* Aboveground biomass variability across intact and degraded forests in the Brazilian Amazon. *Global Biogeochemical Cycles* **30**, 1639-1660 (2016).

21 Dionizio, E. A. *et al.* Aboveground carbon stocks for different forest types in eastern Amazonia. *Environmental Research Communications* **7**, 045006 (2025).

22 Mitchard, E. T. *et al.* Markedly divergent estimates of A mazon forest carbon density from ground plots and satellites. *Global ecology and biogeography* **23**, 935-946 (2014).

23 Lopez-Gonzalez, G. *et al.* Amazon forest biomass measured in inventory plots. Plot Data from 'Markedly divergent estimates of Amazon forest carbon density from ground plots and satellites'. (2014).

24 Chave, J. *et al.* Tree allometry and improved estimation of carbon stocks and balance in tropical forests. *Oecologia* **145**, 87-99 (2005).

25 Vancutsem, C. *et al.* Long-term (1990–2019) monitoring of forest cover changes in the humid tropics. *Science advances* **7**, eabe1603 (2021).

26 Saatchi, S. S. *et al.* Benchmark map of forest carbon stocks in tropical regions across three continents. *Proceedings of the national academy of sciences* **108**, 9899-9904 (2011).

27 Saatchi, S. Mapping global live woody vegetation biomass at optimum spatial resolutions. *Zenodo. doi:10.5281/zenodo.15858551.* **7583611** (2025).

28 Mann, H. B. Nonparametric tests against trend. *Econometrica: Journal of the econometric society*, 245-259 (1945).

29 Kendall, M. G. Rank correlation methods. (1948).

30 Gilbert, R. O. *Statistical methods for environmental pollution monitoring*. (John Wiley & Sons, 1987).

31 Dubayah, R. *et al.* GEDI L2B Canopy Cover and Vertical Profile Metrics Data Global Footprint Level V002. *NASA EOSDIS Land Processes Distributed Active Archive Center (DAAC) data set* (2021).

32 Dalagnol, R. *et al.* Mapping tropical forest degradation with deep learning and Planet NICFI data. *Remote Sensing of Environment* **298**, 113798 (2023). https://doi.org:https://doi.org/10.1016/j.rse.2023.113798

33 Wagner, F. H. *et al.* Mapping tropical forest cover and deforestation with planet NICFI satellite images and deep learning in Mato Grosso State (Brazil) from 2015 to 2021. *Remote Sensing* **15**, 521 (2023).

34 Hansen, M. C. *et al.* High-resolution global maps of 21st-century forest cover change. *science* **342**, 850-853 (2013).

35 Jackson, T. D. *et al.* Tall Bornean forests experience higher canopy disturbance rates than those in the eastern Amazon or Guiana shield. *Global Change Biology* **30**, e17493 (2024).

36 Chen, T. & Guestrin, C. in *Proceedings of the 22nd acm sigkdd international conference on knowledge discovery and data mining.* 785-794.

37 Basso, L. S. *et al.* Atmospheric CO 2 inversion reveals the Amazon as a minor carbon source caused by fire emissions, with forest uptake offsetting about half of these emissions. *Atmospheric Chemistry and Physics* **23**, 9685-9723 (2023).

38 Gatti, L. V. *et al.* Amazonia as a carbon source linked to deforestation and climate change. *Nature* **595**, 388-393 (2021). https://doi.org:10.1038/s41586-021-03629-6

39 Gatti, L. V. *et al.* Increased Amazon carbon emissions mainly from decline in law enforcement. *Nature* **621**, 318-323 (2023). https://doi.org:10.1038/s41586-023-06390-0

40 Rosan, T. M. *et al.* Synthesis of the land carbon fluxes of the Amazon region between 2010 and 2020. *Communications Earth & Environment* **5**, 46 (2024). https://doi.org:10.1038/s43247-024-01205-0

41 Spawn, S. A., Sullivan, C. C., Lark, T. J. & Gibbs, H. K. Harmonized global maps of above and belowground biomass carbon density in the year 2010. *Scientific data* **7**, 112 (2020).

42 Fendrich, A. *et al.* Human influence on Amazon's aboveground carbon dynamics intensified over the last decade. *Nature Communications* **16**, 6681 (2025). https://doi.org:10.1038/s41467-025-61856-1

43 Silva, C. V. *et al.* Estimating the multi-decadal carbon deficit of burned Amazonian forests. *Environmental Research Letters* **15**, 114023 (2020).

44 Walker, W. S. *et al.* The role of forest conversion, degradation, and disturbance in the carbon dynamics of Amazon indigenous territories and protected areas. *Proceedings of the National Academy of Sciences* **117**, 3015-3025 (2020).

45 Godar, J., Gardner, T. A., Tizado, E. J. & Pacheco, P. Actor-specific contributions to the deforestation slowdown in the Brazilian Amazon. *Proceedings of the National Academy of Sciences* **111**, 15591-15596 (2014).

46 Holcomb, A., Burns, P., Keshav, S. & Coomes, D. A. Repeat GEDI footprints measure the effects of tropical forest disturbances. *Remote Sensing of Environment* **308**, 114174 (2024). https://doi.org:https://doi.org/10.1016/j.rse.2024.114174

47 Csillik, O. *et al.* A large net carbon loss attributed to anthropogenic and natural disturbances in the Amazon Arc of Deforestation. *Proceedings of the National Academy of Sciences* **121**, e2310157121 (2024). https://doi.org:doi:10.1073/pnas.2310157121

48 Cook-Patton, S. C. *et al.* Mapping carbon accumulation potential from global natural forest regrowth. *Nature* **585**, 545-550 (2020).

49 Requena Suarez, D. *et al.* Estimating aboveground net biomass change for tropical and subtropical forests: Refinement of IPCC default rates using forest plot data. *Global Change Biology* **25**, 3609-3624 (2019).

50 Heinrich, V. H. A. *et al.* Large carbon sink potential of secondary forests in the Brazilian Amazon to mitigate climate change. *Nature Communications* **12**, 1785 (2021). https://doi.org:10.1038/s41467-021-22050-1

51 Heinrich, V. H. A. *et al.* The carbon sink of secondary and degraded humid tropical forests. *Nature* **615**, 436-442 (2023). https://doi.org:10.1038/s41586-022-05679-w

52 Bourgoin, C. *et al.* Human degradation of tropical moist forests is greater than previously estimated. *Nature* **631**, 570-576 (2024).

53 Duncanson, L. *et al.* Aboveground biomass density models for NASA's Global Ecosystem Dynamics Investigation (GEDI) lidar mission. *Remote Sensing of Environment* **270**, 112845 (2022).

54 Esquivel-Muelbert, A. *et al.* Increasing tree size across Amazonia. *Nature Plants* (2025). https://doi.org:10.1038/s41477-025-02097-4

55 Hubau, W. *et al.* Asynchronous carbon sink saturation in African and Amazonian tropical forests. *Nature* **579**, 80-87 (2020). https://doi.org:10.1038/s41586-020-2035-0

56 Sims, M. J. *et al.* Global drivers of forest loss at 1 km resolution. *Environmental Research Letters* **20**, 074027 (2025).

57 Fayad, I. *et al.* DUNIA: Pixel-Sized Embeddings via Cross-Modal Alignment for Earth Observation Applications. *arXiv preprint arXiv:2502.17066* (2025).

58 Quegan, S. *et al.* The European Space Agency BIOMASS mission: Measuring forest above-ground biomass from space. *Remote Sensing of Environment* **227**, 44-60 (2019).

59 Dubayah, R. *et al.* GEDI L2A elevation and height metrics data global footprint level V002. *NASA EOSDIS Land Processes Distributed Active Archive Center (DAAC) data set*, GEDI02_A. 002 (2021).

60 Santoro, M. & Cartus, O. ESA Biomass Climate Change Initiative (Biomass_cci): Global datasets of forest above-ground biomass for the years 2007, 2010, 2015, 2016, 2017, 2018, 2019, 2020, 2021 and 2022, v6.0. *NERC EDS Centre for Environmental Data Analysis* (2025). https://doi.org:https://dx.doi.org/10.5285/95913ffb6467447ca72c4e9d8cf30501

61 Dubayah, R. *et al.* GEDI L4B gridded aboveground biomass density, version 2.1. *ORNL DAAC* (2023).

62 Dubayah, R. *et al.* Pantropical Forest Height and Biomass from GEDI and TanDEM-X Data Fusion. *ORNL DAAC, Oak Ridge, Tennessee, USA* (2023).

63 Santoro, M. *et al.* The global forest above-ground biomass pool for 2010 estimated from high-resolution satellite observations. *Earth System Science Data* **13**, 3927-3950 (2021).

64 Baccini, A. *et al.* Estimated carbon dioxide emissions from tropical deforestation improved by carbon-density maps. *Nature Climate Change* **2**, 182-185 (2012). https://doi.org:10.1038/nclimate1354

65 Avitabile, V. *et al.* An integrated pan-tropical biomass map using multiple reference datasets. *Global change biology* **22**, 1406-1420 (2016).

66 Martin, A. R., Doraisami, M. & Thomas, S. C. Global patterns in wood carbon concentration across the world's trees and forests. *Nature Geoscience* **11**, 915-920 (2018).

67 Cuni-Sanchez, A. *et al.* High aboveground carbon stock of African tropical montane forests. *Nature* **596**, 536-542 (2021).

68 Souza Jr, C. M. *et al.* Reconstructing three decades of land use and land cover changes in brazilian biomes with landsat archive and earth engine. *Remote Sensing* **12**, 2735 (2020).

69 Long, T. *et al.* 30 m resolution global annual burned area mapping based on Landsat Images and Google Earth Engine. *Remote Sensing* **11**, 489 (2019).

70 Liu Shidong, C. P., Zhang Jie, Penuelas Josep, Ding Shengping, Nath Biswajit, Song Wanjuan, Wu Xia, Zhang Yaping, Jacquet Iskid, Li Wang, Huang Ni, Niu Zheng, Wang Li. Road-induced fragmentation endangers half of the global tropical tree cover. *In preparation* (2025).

71 Lapola, D. M. *et al.* The drivers and impacts of Amazon forest degradation. *Science* **379**, eabp8622 (2023).

72 Vancutsem, C. *et al.* Long-term (1990–2019) monitoring of forest cover changes in the humid tropics. *Science Advances* **7**, eabe1603 (2021). https://doi.org:doi:10.1126/sciadv.abe1603

73 Unep-Wcmc, I. Protected Planet: The World Database on Protected Areas (WDPA) and World Database on Other Effective Area-based Conservation Measures (WD-OECM). *Cambridge, UK: UNEP-WCMC and IUCN* (2025).

74 Fendrich, A. *et al.* Human influence on Amazon's aboveground carbon dynamics intensified over the last decade. *Nature Communications* **16**, 6681 (2025).

75 Potapov, P. *et al.* Mapping global forest canopy height through integration of GEDI and Landsat data. *Remote Sensing of Environment* **253**, 112165 (2021).

76 Qi, W. *et al.* Mapping large-scale pantropical forest canopy height by integrating GEDI lidar and TanDEM-X InSAR data. *Remote Sensing of Environment* **318**, 114534 (2025).

77 Lang, N., Jetz, W., Schindler, K. & Wegner, J. D. A high-resolution canopy height model of the Earth. *Nature Ecology & Evolution* **7**, 1778-1789 (2023).

78 Brasileiro, S. F. & José Humberto, C. LiDAR data collected in the Caxiuanã National Forest, State of Pará, Brazil, in the year 2022. (2025).

79 Brasileiro, S. F. & José Humberto, C. LiDAR data collected in the Caxiuanã National Forest, State of Pará, Brazil, in the years 2018, 2019, 2020 and 2021. (2025).

80 Brasileiro, S. F. & Chaves, J. H. LiDAR data collected in the Jamari National Forest, State of Rondônia, Brazil, in the years 2018, and 2019. (2025).

81 Brasileiro, S. F. & Chaves, J. H. LiDAR data collected in the Jamari National Forest, State of Rondônia, Brazil, in the year 2022. (2025).

82 Fawcett, D. *et al.* Declining Amazon biomass due to deforestation and subsequent degradation losses exceeding gains. *Global Change Biology* **29**, 1106-1118 (2023).

83 Zhu, L. *et al.* Comparable biophysical and biogeochemical feedbacks on warming from tropical moist forest degradation. *Nature Geoscience* **16**, 244-249 (2023). https://doi.org:10.1038/s41561-023-01137-y